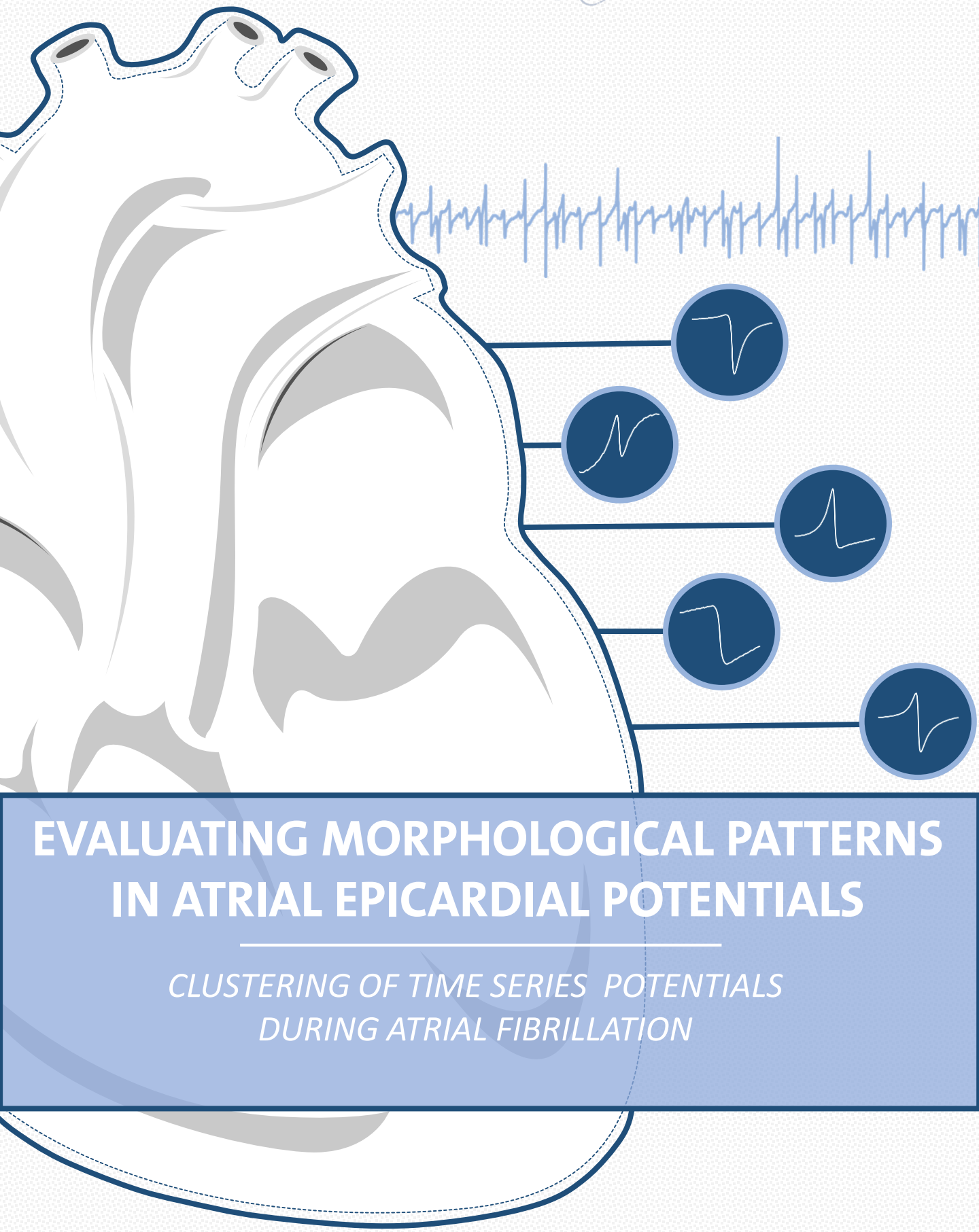

EVALUATING MORPHOLOGICAL PATTERNS IN ATRIAL EPICARDIAL POTENTIALS

CLUSTERING OF TIME SERIES POTENTIALS DURING ATRIAL FIBRILLATION

MSc Thesis Technical Medicine
Sensing and Stimulation
J.A. Roest

EVALUATING MORPHOLOGICAL PATTERNS IN ATRIAL EPICARDIAL POTENTIALS

CLUSTERING OF TIME SERIES POTENTIALS DURING ATRIAL FIBRILLATION

J.A. (Jeroen Alfred) Roest

Student number : 4498615

October 15, 2021

Thesis in partial fulfilment of the requirements for the joint degree of Master of Science in

Technical Medicine

Leiden University ; Delft University of Technology ; Erasmus University Rotterdam

Master thesis project (TM30004 - 35 ECTS)

Department of Translational Electrophysiology, Erasmus Medical Center

January 2021 – October 2021

Supervisors:

Prof. Dr. N.M.S. De Groot	Erasmus MC	Medical supervisor
Dr. Ir. R.C. Hendriks	TU Delft	Technical supervisor
Drs. M.S. Van Schie	Erasmus MC	Daily supervisor

Thesis committee members:

Prof. dr. N.M.S. De Groot (chair)	Erasmus MC	Department of Translational Electrophysiology
Dr. Ir. R.C. Hendriks	TU Delft	Circuits and Systems, Microelectronics
Dr. Y.J.H.J. Taverne	Erasmus MC	Department of Thoracic Surgery
Drs. M.S. Van Schie	Erasmus MC	Department of Translational Electrophysiology

TU Delft Erasmus MC

Preface

Just over six years ago, I entered the bachelor's program Clinical Technology. Not unlike me, I recall being fairly doubtful in my decision regarding what program to choose in the summer prior to the start. I turned 18 on the day prior to the day I started my first lecture from the program. From the starting years, I noticed developing an increased interest in the field of cardiology and neurology. The interest regarding cardiology exceeded over the neurologic field during my internships, partly due to the internship availability at that time. Hence, I decided to perform my graduation internships in the (sub)field of my greatest interest. I returned to one of the departments from my previous internships: translational electrophysiology. The complexity of activation patterns required for coordinated activation and large volume of data makes the department of translational electrophysiology highly suitable for a technical physician.

Firstly, I would like to thank all supervisors for the possibility to shape an assignment suited to my specific wishes. Natasja, thank you for giving me the opportunity to return to the department as a graduate student. Thank you for taking your time in your busy agenda to discuss and help me overcome the encountered problems during this internship. Above all, thank you for keeping me on the right track and preserving perspective at moments where I tended to wander from the path to the eventual goal. Richard, thank you for your continuous positivity and triggering me to look at the problem from other point of view. Your attitude invites me to put problems in broader perspectives. Besides, you always came up with suggestions and opportunities to overcome the problems I encountered. Mathijs, thank you for being my primary point of contact. Thank you for your help in interpretation of the results and, likewise Natasja, keep my focus on the end goal. Besides your help regarding this thesis, I would like to thank you for our talks about the perspectives and opportunities for technical physicians in a general sense. Yannick, thank you for contributing in my defence committee. To the colleagues at the department, thank you for always make room for discussion and providing feedback on possible different approaches and overlooked topics. More importantly, thank you for creating a comfortable and sociable environment with common coffee talks and Friday drinks. Lastly, I would like to thank my friends and family for consistently being my exhaust valve. Thank you for the continuous support, appreciation and the ability to clear my mind around you.

This master's thesis is the result of the graduation internship and concludes my journey as a student. Over the course of six years, I can say that I am very satisfied with the decision I have made in the summer six years ago. I am yet to find out what the future path for me will be, but I am highly excited to find out.

Jeroen Roest
Rotterdam, October 2021

Abstract

Introduction: Potentials measured at the epicardial surface contain information regarding the conductive properties of the atrial tissue. The current lack of morphological categorization during atrial fibrillation (AF) provokes the usage of unsupervised learning methods to evaluate time series electrograms across the atrial surface. Analysis of regional potential morphology increases insight in individual tissue characteristics, possibly aiding in future selection of patients with AF benefitting from additional treatment with.

Methods: single potentials (SP) are extracted from four defined regions: right atrium (RA), left atrium (LA), pulmonary veins (PV) and Bachmann's bundle (BB). The methods are divided in two parts. In part one, the clusters are determined. Choice of algorithm, evaluation of distance metrics and evaluation in reduced dimensionality are performed sequentially to determine the eventual clustering setup. The clustering setup is repeated for different types of input data, originating from different regional structures (all four regions, solely LA and solely the RA) to avoid deterioration of cluster formation from single region(s). In the second part, the clusters are adapted to evaluate morphological characteristics in the included regions.

Results: Data from a total of 23 patients was used, containing 128 files and 468588 SPs. K-means using the first 8 principal components was deemed the most suitable clustering method with the current data, identifying a total of five clusters. The clusters showed evident different morphology, mostly distinguishable by RS-ratio and potential duration. RA showed a predominant S to an RS-wave pattern, comparable to PV. Both showed similar contribution of fast and slow S-wave morphology. LA showed a RS to R-wave morphology. The cluster showing a slow S-wave morphology was substantially increased across BB compared to other regions but also when compared to other clusters in BB.

Conclusion: Looking at spatial cluster occurrence through an RS-ratio perspective, the beforehand expected deviation from AF compared to sinus rhythm (SR) was not observed. The observed pattern during AF suggests more elaborate contribution of atrial tissue than often targeted in current daily practice. The methodology and defined groups of potentials facilitate evaluation of potential morphology at an individual level. Translation to an endocardial perspective could assist in selecting patients eligible for additional treatment when technologically feasible. Future research should be focused on including potentials containing multiple deflections and estimation of progression state of the atrial tissue.

Table of contents

List of abbreviations

AF	Atrial fibrillation
SR	Sinus rhythm
ML	Machine learning
AI	Artificial intelligence
SP	Single potential
SDP	Short double potential
LDP	Long double potential
FP	Fractionated potential
SAN	Sinoatrial node
AVN	Atrioventricular node
RA	Right atrium
LA	Left atrium
BB	Bachmann's bundle
PV	Pulmonary vein region
ECG	Electrocardiogram
AAF	Acute atrial fibrillation
PAF	Paroxysmal atrial fibrillation
PeAF	Persistent atrial fibrillation
LSPAF	Long-standing persistent atrial fibrillation
PerAF	Permanent atrial fibrillation
LAT	Local activation time
MVD	Mitral valve disease
AVD	Aortic valve disease
CABG	Coronary artery bypass grafting
BPM	Beats per minute
WCSS	Within-cluster sum of squares
GMM	Gaussian mixture models
DBSCAN	Density-based spectral clustering of applications with noise
BIC	Bayesian information criterion
AIC	Akaike information criterion
IQR	Interquartile range
PCA	Principal component analysis

Abbreviations follows by 's' refer to the pleural form of the abbreviation.

INTRODUCTION & BACKGROUND

1

Introduction

Atrial fibrillation (AF) is the most common cardiac arrhythmia. Lots of provoking factors for the development of AF have been identified. Examples are hypertension, diabetes and smoking (1, 2). The most important contributor to the development of AF is age. Especially ages above 65 show increased susceptibility to develop AF (3). Although not a directly fatal arrhythmia, its presence is associated with increased risk of stroke (1, 4), myocardial infarction (5, 6) , heart failure (7) and mortality (8). Current prevalence of AF is estimated around 9 million in Europe. However it is expected that the prevalence will be more than doubled by 2060 (9). The increased risk at morbidity and mortality combined with the expected increasing prevalence underlines the need for adequate management of AF. The ability to adequately treat patients with AF greatly relies on understanding the underlying electrophysiological mechanism of the arrhythmia.

I. Atrial fibrillation mechanisms

Multiple theories regarding the mechanisms for the perpetuation of AF have been proposed. Three major hypotheses are linked to the perpetuation in AF: rotors or ectopic foci, the presence of multiple simultaneously present wavelets across the atrial surface and asynchrony of the endocardium and epicardium facilitating possibility for reentrant circuits (10-13).

Ablation strategies attempt to eliminate AF by targeting the arrhythmic substrate. However, no consensus regarding a ground truth of characteristics of arrhythmic substrate is defined. Hence, results of different ablation therapies are currently unsatisfactory (14, 15). A possible explanation to the disappointing success rates of ablation procedures might be the co-existence of multiple mechanisms. Besides, AF has a progressive nature due to remodeling of atrial tissue during the arrhythmia (16). The longer AF is present, the more the conductive properties of the cardiac tissue will deteriorate and the more resistant the arrhythmia becomes to therapy.

II. Potential morphology characterization

The co-existence of multiple mechanisms causes variability in potentials between different patients. The observed potential at the surface can be regarded as the sum of all activity of the underlying cardiac cells. Therefore, potential morphology might yield information regarding the state of the underlying pathophysiological mechanisms. During ablation procedures, inspection of the atrial tissue characteristics is performed by an endocardial approach. These electrophysiological procedures are limited by atrial luminal size (17). Performing thoracic surgery provides the opportunity for detailed investigation of the atrial surface (18).

Konings et al. divided potentials according to the number of deflections and their respective intervals (19). However, other contributing factors can be used to further characterize potentials like slope, amplitude and RS-ratio (20, 21). Besides, characteristics cannot be regarded independently. For instance, a higher grade of fractionation directly resulted in reduced amplitude during sinus rhythm (SR) (22).

III. Regional analysis

Potential characteristics can differ between patients, but significant changes in morphology can be observed across different areas of the atrial tissue as well. During SR, significant differences in RS-ratios are observed when analysing single potentials (SP) (20, 21). However, distinct descriptions of (localized) morphologies of the atrial complexes are lacking during AF. Studies have shown an increased number of simultaneous waves innervating the tissue, an increased number of fractionated potentials, more conduction block and a slower conduction velocity with longer sustained AF (23, 24). During AF, the activation pattern of the myocardium is therefore expected to be more complex, with

more diverting potential morphology compared to SR. Analysis of SP morphology might therefore enhance understanding of tissue characteristics.

IV. Clustering analysis

Categorization regarding epicardial potential morphology during AF is yet to be been established in literature. The lack of consensus sparks the opportunity of adapting a unsupervised learning methodology to investigate the morphological structures present in electrograms observed at the atrial surface. Attempts have been performed using bipolar electrograms (25-27). Besides the bipolar nature of the electrograms, these methods are targeted towards finding the atrial substrate rather than describing electrogram morphology. Furthermore, current publications often use parameterization of the signal. Even more information might be retained in the raw signal. Hence, clustering of time series potentials might be of added value for describing the morphology of potentials occurring at the atrial surface during AF.

V. Goal

The goal of this thesis is to analyze the morphologies of (single) potentials occurring at the atrial epicardial surface during AF. The first objective is determining the observed clusters from the electrograms. Subsequently, the observed clusters can be utilized to evaluate patterns across the atrial surface. Gaining insight into individual tissue characteristic across the atrial surface might aid in selecting patients eligible for treatment and patients which are not. In this sense, classification of atrial epicardial potentials can aid as a diagnostic tool. Translation to endocardial unipolar high-resolution mapping in the future could reduce the threshold for diagnostic opportunities in patients.

Thesis outline

Chapter 1 covers the introduction to the project with the according goal to reach. Chapter 1 also describes the relevant background regarding the clinical and technical concepts which are passed in the thesis. Chapter 2 covers the methodology of the performed research. Chapter 3 covers the results of the thesis. Both chapter 2 and 3 are split in two parts along the way for the sake of clarity. The first part covers the method and results of the cluster determination. The second part of both chapters covers the method and results of the spatial cluster occurrence. In chapter 4, both objectives are merged into the discussion section and the thesis is concluded. An additional chapter (chapter 5) covers the appendices of the thesis.

Background

I. Cardiac anatomy

The heart serves as the pump for the supply of blood through the body. The heart contains four chambers. The chambers are divided by its position on the left or right site of the heart. The upper chambers are referred to as the atria, whilst the bottom chambers are referred to as the ventricles. The left and right side of the heart are separated by a septum. Remaining closure of the chambers is achieved through four valves. The valves between the atria and the ventricles are specified as the atrioventricular valves: the mitral and the tricuspid valve. The valves between the ventricles and their corresponding arteries are called the semilunar valves: the aortic and the pulmonary valve. An overview of the valves is shown on the left side of the Figure 1. The tricuspid valve separates the right atrium from the right ventricle. From the right ventricle, the blood is pumped through the pulmonary valve into the pulmonary artery. The left atrium is separated from the left ventricle by the mitral valve. The left ventricle pumps the blood towards the rest of the body through the aorta, passing the aortic valve.

Cardiac tissue contracts in a coordinated way to permit movement of the blood through the heart chambers. Movement into the right direction is facilitated by the cardiac valves, which all function as unidirectional valves. This is shown at the right site of the Figure 1. In the phase 1, the left and right atrium are filled with blood originating from the lungs and the rest of the body, respectively. After filling of the atria, cardiac tissue contracts. The contractile function of the cardiac tissue increases the pressure in the atria. Once the pressure in the atria surpasses the pressure in the ventricles, the atrioventricular valves open to allow flow of blood through the ventricles (shown in phase 2 and 3). Once the ventricles are filled, contraction of ventricular tissue is initiated. The atrioventricular valves close and semilunar valves open, forcing the blood to flow through either the pulmonary artery or the aorta (as shown in phase 4). This is also referred to as systolic phase of the cardiac cycle. Phase 1 to 3 represent the diastolic phase.

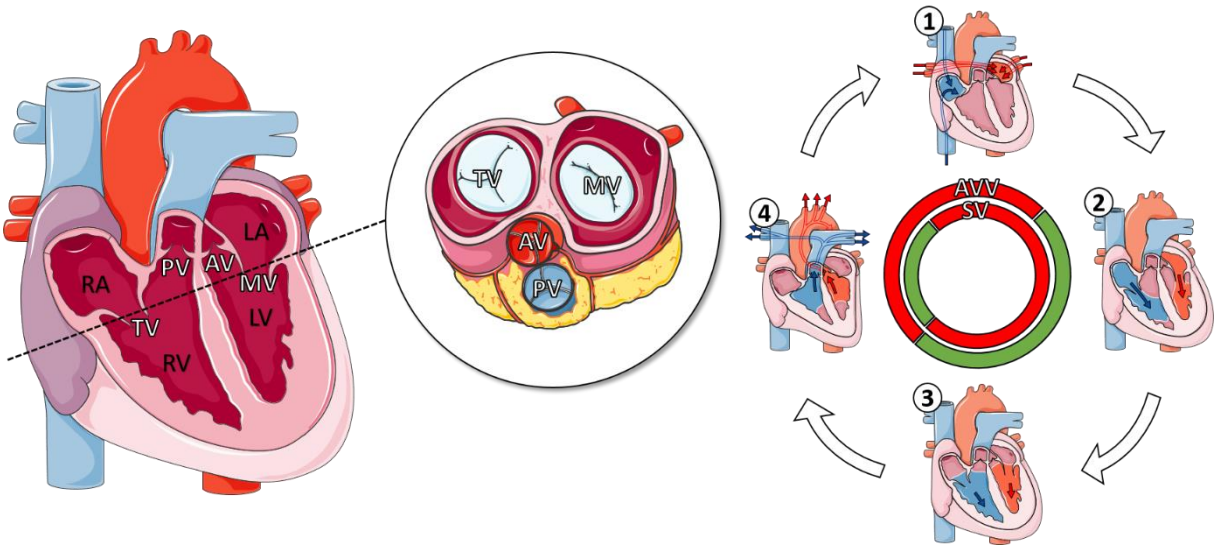

Figure 1: Valvular anatomy in the heart. The figure on the left the valvular positions from a frontal view. The encircled component shows a transversal view of valvular positions. The ventral site of the patient is at the bottom of the figure. The figure on the right shows opening of the semilunar valves and atrioventricular valves during the different components of the heart cycle. The green area represents opening of the respective valves, whilst the red area represents closure of the respective valves. RA represents the right atrium, RV represents the right ventricle, LA represents the left atrium, LV represents the left ventricle, TV represents the tricuspid valve, MV represents the mitral valve, PV represents the pulmonary valve, AV represents the aortic valve, AVV represents the atrioventricular valves, SV represents the semilunar valves.*

Contractile dysfunction or valvular dysfunction can both cause inadequate movement of blood, restricting the supply of nutrients to other parts of the body. Furthermore, both factors have substantial interplay. Valvular dysfunction can cause eventual contractile dysfunction. For example, valvular dysfunction has been associated with increased risk of AF (28, 29). Vice versa, contractile dysfunction can cause eventual valvular dysfunction. The reduced (ventricular) contractile dysfunction can cause ineffective closure of the valve. Mitral valve regurgitation is a common complication following reduced contractile dysfunction due to myocardial infarction. Hence, both components are vital for adequate delivery of oxygen and nutrients.

II. Electrophysiology

A. Conduction system

Valvular function is a mostly passive mechanism, its opening and closure is coordinated by respective pressure differences between the spaces it is separating. However, the contractile (orpump) function of the heart is a highly controlled mechanism consisting of a segment generating pulses which are transported through conductive paths across the cardiac tissue. Regular conduction starts in the sinoatrial node (SAN), located superiorly in the right atrium (RA). The pulses travel across the atrial tissue towards the atrioventricular node (AVN). The left atrium (LA) is connected to the RA through a specialized cardiac structure called Bachmann's bundle (BB) (30). Cardiac cells are electrically coupled through gap junctions. Innervation of a single cell of the heart will therefore result in innervation of all tissue. Hence cardiac tissue behaves as a functional syncytium. Atrioventricular valves are anchored using a fibrotic skeleton. Besides the help in permitting flow of blood in the preferred direction, the fibrotic skeleton also provides electric isolation between the atria and the ventricles of the cardiac system (31). The sole passage between the two structures is the AVN. Upon arrival at the AVN from the atria, the propagation is delayed, allowing the ventricles to be filled during atrial contraction without counteraction from ventricular contractile activity. The ventricular conduction system ensures high-speed conduction to allow simultaneous contraction of all ventricular tissue. The systems consists of the His bundle after which the impulses are separated into a left and a right ventricular bundle. Both bundles debouch in Purkinje fibers, innervating surrounding (ventricular) myocardial tissue, the conductive pathways across the heart are displayed in Figure 2.

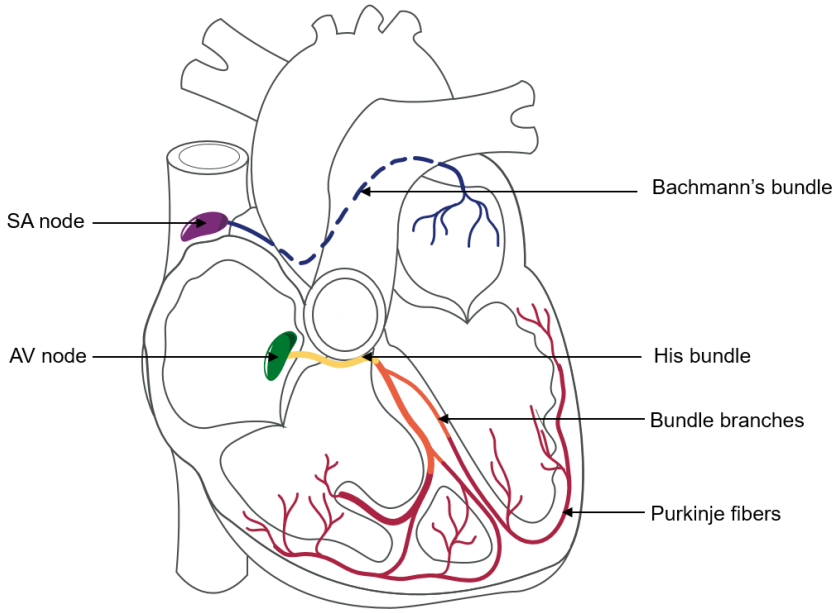

Figure 2: Cardiac conduction system, the different structures are color-coded.*

B. The action potential

Inactivated cardiac cells contain a negative transmembrane potential. Activation of a cardiac cell is achieved when the increase of intracellular electric charge causes the transmembrane potential to surpass a certain threshold. Increase of intracellular electric charge can be achieved by influx of ions through a neighboring cardiac cell. Activation of a cardiomyocyte, resulting in a temporary change of transmembrane potential, is called the action potential. The action potential is generated by timed opening and closing of ion channels (Na^+ , Ca^{2+} and K^+) across the membrane, divided into five phases. Phase 4, also called the resting state, represents the inactivated cell. Once activated, rapid opening of Na^+ channels results in steep increase of the transmembrane potential (phase 0). In phase 1, K^+ channels open causing outflow of potassium. This is shown by a reduction of the transmembrane potential. Once the Ca^{2+} channels open, the transmembrane potential is stabilized. This is referred to as phase 2 (or the plateau phase). In the last phase of the action potential, the flow of potassium out of the cell causes the transmembrane potential to returns to its original value. Once a cardiac cell is activated, additional activations are ineffective in producing a new action potential (phase 0 to 2). This period is declared as the effective refractory period. At the end of the plateau phase, it is possible for a new stimulus to initiate a new action potential. However, if a new action potential is initialized before reaching the resting potential, the new action potential will be smaller in amplitude. This period is also called the relative refractory period. An overview is provided in Figure 3.

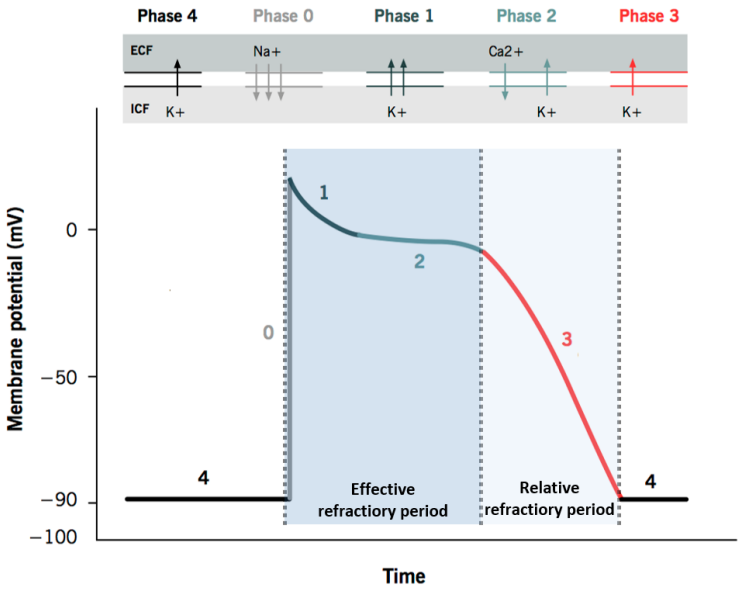

Figure 3: Action potential, divided into the predefined phases. Figure adapted from (32).

C. Atrial fibrillation

The automaticity of the SAN generates action potentials which are transported through the cardiac tissue as specified earlier. Heart rhythm originating from the SAN has the appurtenant name: SR. AF is characterized by chaotic activity of the atria of the heart. Pulses are no longer originating from the SAN. Another focus or multiple foci can cause the innervation across the atria, characterized by beat-to-beat changes. Different timing of waves arriving at the AVN causes variability in intervals between ventricular beats. The chaotic atrial activity causes disappearance of the p-wave on the electrocardiogram (ECG). The ECG is further characterized by variation in ventricular beat intervals, as shown in Figure 4.

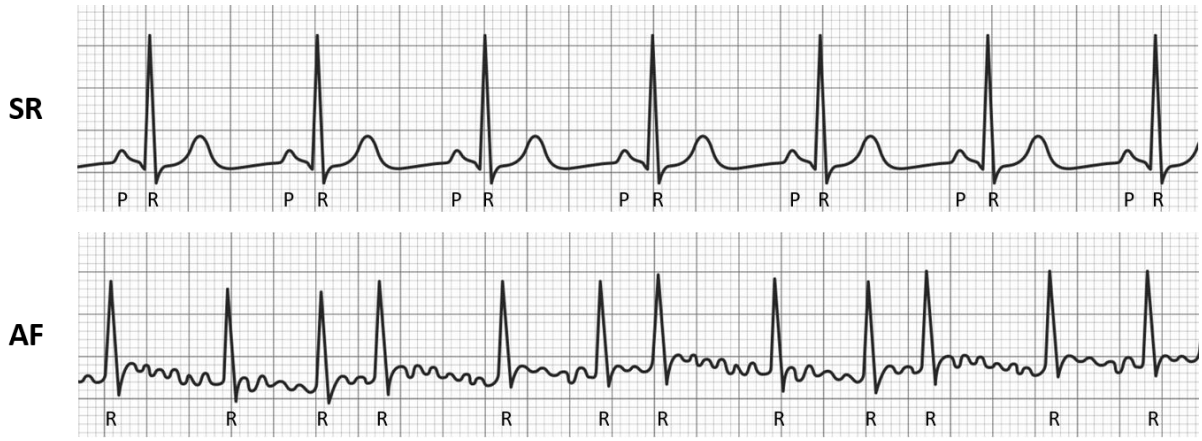

Figure 4: ECG recordings of SR (upper panel) and AF (lower panel).

AF is thought to be an extensive interplay between a trigger and a substrate necessary to perpetuate the arrhythmia. First episodes of AF are thought to be results from atrial extrasystolic beats. However, AF has a progressive nature due to contractile, electrical and structural remodeling of the atrial tissue arises during AF (16). Altered cellular Ca^{2+} handling can be thought to play a major role in remodeling of the atrial tissue. The altered Ca^{2+} concentrations shortens the effective refractory period, eventually leading to shorter cycle lengths and increased susceptibility to reentrant circuits (33). Furthermore, decreased Ca^{2+} concentrations cause decrease of contractile function of the atrial tissue. This is accompanied by degeneration of the contractile elements (sarcomeres), eventually leading to atrial tissue stretch Ca^{2+} (34). Atrial stretch creates space for structural remodeling with loss of cellular coupling (connexin proteins) and fibrosis (35, 36). Although electrical remodeling is shown to be recovering after up to years of sustained arrhythmic episodes, structural remodeling does not appear to share these recovering properties (37). Therefore, with sustained AF, the arrhythmia transforms from trigger induced to substrate mediated overtime. The longer AF is sustained, the more resistant it becomes to therapy (38). To differentiate between patients with different stages of remodeled tissue, AF is currently categorized based on time from the first recorded episode (39). Paroxysmal AF (PAF) is described as AF terminating within 7 days, spontaneously or by intervention. Persistent AF (PeAF) is described as continuous AF, sustained for more than 7 days. PAF becomes long-standing persistent AF (LSPAF) when AF is sustained for longer than 12 months. When the goal of restoring to SR is no longer pursued, AF is referred to as permanent AF (PerAF).

Recent reports regarding AF epidemiology report a 31% higher incidence compared to a decade ago, accompanied by a 33% increase in prevalence over the past 20 years (40). The observed increase in suffering from AF is expected to increase in the upcoming decades as well (9, 40). Age is one of the most prominent risk factor for the development of AF. Furthermore, prevalence of longer sustained AF is higher at increased age (41-43). Coherent with increasing lifetime expectancy, it is expected that AF will contribute to become an even greater healthcare burden in the future.

III. Cardiac tissue mapping

A. Bipolar and unipolar mapping

Electrodes are capable of measuring the extracellular current when placed on the cardiac surface. A configuration of multiple electrodes simultaneously capturing activity along the surface of the cardiac tissue to allow identification of spatio-temporal characteristics, is referred to as cardiac mapping. Cardiac mapping is usually performed in a unipolar or bipolar fashion. To derive a potential over time, two measurement points are always required. In bipolar measurements, the potential is derived between two closely spaced electrodes. In unipolar measurements, one electrode captures activity at

the site of interest, while the other electrode is positioned remotely. The remote electrode functions as an indifferent electrode.

Both methods have their respective advantages and disadvantages. In unipolar electrograms, the global activation of the underlying cardiac tissue is recorded. The gained advantages are direction-independent electrograms and reduced requirement for intimate contact to record the electrograms. However, unipolar electrograms are sensitive to remote activation. Ventricular activity interferes the electrograms recorded from local atrial tissue activity (known as far-field activity). In bipolar electrograms, the close proximity of the electrodes causes far-field activity to be simultaneously present on both of the recording electrodes. The subtraction causes effective cancellation of far field interference. Furthermore, other sources of noise causes further contamination of unipolar electrograms (44), which can be effectively reduced using bipolar recordings. Usage of bipolar electrograms does introduce direction dependency and the increased requirement for substantial contact. The potential determination and direction dependency are visualized in Figure 5.

Both methods show their own assets in cardiac tissue mapping and provide complementary information. However, the effective cancellation of noise causes endocardial electrophysiological procedures to be performed mainly using bipolar electrograms (45).

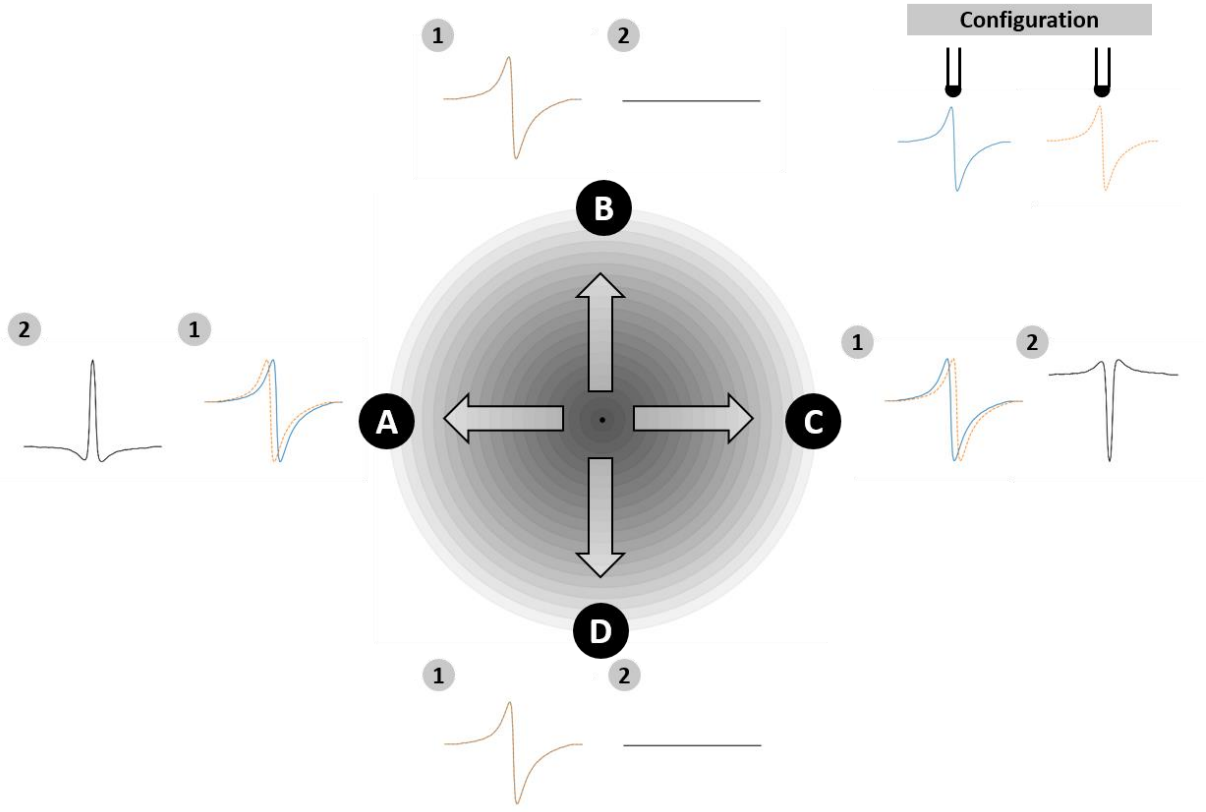

Figure 5: Direction dependency when using bipolar potentials. The electrode configuration is shown in the top right. The solid line represents the left electrode, the dotted line represents the right electrode. The bipolar electrodes are calculated by subtracting the right from the left electrode. The labelled black dots indicate measurement sites. Number 1 shows the temporal alignment of the two unipolar electrodes. Number 2 shows the resulting bipolar electrogram. When the wave enters from a transversal plane to the electrode configuration, the deflection will not be registered using bipolar measurement (measurement B and D). When the wave enters from a plane parallel to the electrode configuration, the bipolar electrogram polarity depends on the origination site of the wave (see measurement A and B). Using unipolar electrograms, measurement on any of the indicated locations will result in the same recorded electrogram.

B. Potential morphology

A propagating action potential causes changes in the charge of the extracellular space. In front of the propagating wave, the intracellular potential is more negative with respect to the extracellular potential, leading to a negative transmembrane potential. This is followed by influx of current through the intracellular gap junctions. The resulting increase in transmembrane potential causes influx of current from the extracellular space. In this way, a propagating wave can be regarded as a propagating bipole (45, 46). The potential in the extracellular space is positive in front and negative behind the propagating action bipole. Hence, an increase in the recorded potential voltage will appear when the wavefront is approaching the electrode (R-wave) and a decrease in potential voltage will be produced when the wavefront is leaving the electrode (S-wave). The activation of the tissue underneath the electrode is clearly visible by a steep deflection from the R-wave to the S-wave, refered to as the local activation time (LAT). Summation of all activity from the cardiomyocytes (all bipoles) generates the observed potential (21). An example is displayed in the left panel of Figure 6.

In accordance with the theory of the generation of the deflection, different R-wave and S-wave can be observed based on site where the wavefront is initialized. During SR, origination will be from the SAN. Hence, a S-wave pattern is to be expected in potentials recorded near the SAN. At sites where the wavefront terminates, a R-wave pattern can be expected (21). However, the potential can be further described by the amplitude and the slope (47). As mentioned, the potential is generated by the sum of all underlying bipoles. The amplitude is dependent on the volume of activated tissue. Low voltage amplitude regions are regions showing little electrical activity. These sites are regarded as potential arrhythmogenic substrate and therefore these regions are often targeted in ablation strategies, especially in PAF (48). Furthermore, areas of slow conduction show lower slopes and amplitudes (49). The delayed slope is the result of a slower propagation wave. The reduced amplitude results from the lowered amount of tissue activated synchronously.

Previously described potentials are applicable if all cardiac tissue is innervated in a synchronous matter. Remodeling of atrial tissue decreases the conductive abilities, causing asynchronous activation of different groups of myocardial tissue underneath the electrode. The asynchronous activation is represented in the electrogram by a potential showing multiple deflections. The deflections have been categorized by Konings et al. (19) based on the number of deflections and their respective intervals: SP, short double potentials (SDP, two deflections, interval < 15 ms), long double potentials (LDP, two deflections, interval ≥ 15 ms) and fractionated potentials (FP, more than two defection). Examples of the different types of potentials is displayed in Figure 6.

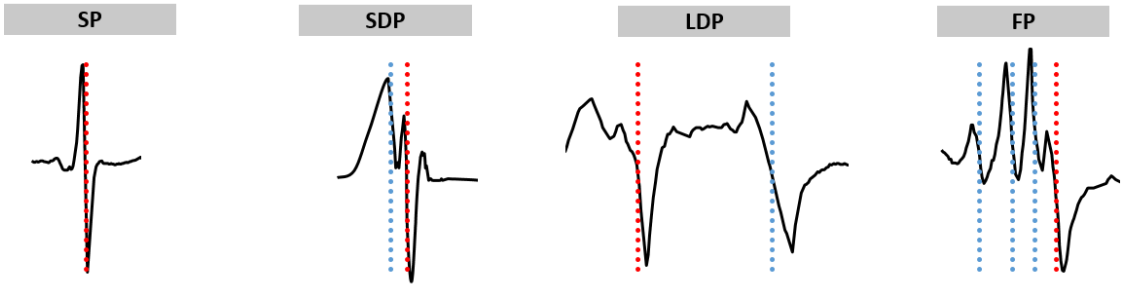

Figure 6: Types of unipolar potentials. The vertical dotted lines represent the LATs. The potential with the steepest deflection is refered to as the primary deflection (red dotted lines). The other deflections are refered to as the secondary deflections (blue dotted lines).

IV. Unsupervised learning

Machine learning (ML) falls under the elaborate field of artificial intelligence (AI). AI refers to systems mimicking problem-solving and autonomous decision making analogous to the human mind. ML attempts to learn models by learning from a set of input data, without the need of explicit programming of the model. Two major branches of ML are supervised and unsupervised ML.

In supervised learning, a set of decision rules is constructed based on a set of training data, supplied with labels. The performance of the eventual decision rules can be evaluated through a set of test data. The newly formed decision rules are applied to predict new labels of the test data. Comparison of the predicted labels to the true labels results in an estimation of the error. The model can be improved iteratively to minimize the error of the created model. Supervised ML algorithms can be of added value in medicine for increasing diagnostic and prognostic abilities. Examples from multiple fields have shown promising results from the usage of supervised ML methods, aiding in early or improved diagnosis (50, 51). Furthermore, the growing computational capabilities give rise to the necessity of (partly) automatic interpretation of data. Applicable fields of interest could be automatic sleep staging using polysomnographic measurements and automatic arrhythmia detection from the ECG (52, 53).

In unsupervised learning, the data is not accompanied by predefined labels. Hence, the model cannot be evaluated through comparison of the predicted labels with the true labels. Similarity between samples in the datasets are explored to find patterns in the given input data. Unsupervised learning is mostly fitted for clustering analysis or detection of anomalies. Although fields of applications are less obvious than supervised ML, unsupervised ML methods can be adopted to evaluate patterns in yet to be defined subgroups. A highly suitable topic is genetics (54).

METHODS 2

Methods

I. Study population

Data of epicardial mapping procedures during open heart surgery are collected. Motives for open heart surgery amongst included data were: coronary artery disease (resulting in coronary artery bypass grafting, or CABG, surgery), mitral valve disease (MVD) and aortic valve disease (AVD). Data is originates from the Halt & Reverse study and the QUASAR study (55, 56). Approval for the studies has been granted by the local medical ethical committee of Rotterdam : METC: 2014-393 and 2010-054, respectively. Written informed consent was collected for all participants.

Patient characteristics were retrieved through medical records. Patient characteristics were: age, BMI, hypertension, diabetes mellitus, dyslipidemia, AF subtype, type of surgery and usage of anti-arrhythmic drugs. One additional type of AF is not described in the clinically handled categorization. For patients in SR without contradictory indications, an attempt to induce AF was performed trough bipolar epicardial pacing. Contradictory indications for the induction of AF were: Wolff-Parkinson-White syndrome, decreased left ventricular function (ejection fraction <40%), presence of cardiac assist devices, usage of inotropic agents and either kidney or liver failure. In case of successful induction within a patient without prior history of AF, it was indicated as acute atrial fibrillation (AAF).

II. Mapping procedure

Mapping was performed in the perioperative setting. Surface ECG lead I was extracted by placing electrodes on both shoulders. Mapping was performed before the patient was connected to extracorporeal circulation, patients were under general anesthesia. Atrial potentials are recorded using a 24 by 8 array (192 electrodes) or 16 by 8 array (128 electrodes) of unipolar electrodes, both with an inter-electrode distance of 2 mm. To perform unipolar measurements, a steel wire was connected to the subcutaneous tissue of the thoracic cavity. The reference electrode consisted of a temporal bipolar electrode connected to the RA free wall (18, 57). Multiple regions were recorded, as shown in the Figure 7. The number of measurements varies depending on atrial size. A description of anatomical landmarks serving as reference for mapping positions is described by Kik et al. (57). All positions were recorded for 5 seconds during SR and for 10 seconds during AF. Mapping the entire surface was deemed preferential to omission of areas. Hence, possible small overlap between adjacent recordings was accepted. If applicable, an attempt to induce AF was performed. Epicardial pacing from the RA appendage was performed starting with 2 ms pulses at 250 beats per minute (BPM). BPM was increased with 50 when induction failed. In case of failed attempt at 400 BPM or loss of capture appears, induction of AF will be terminated (55, 56). Cardioversion will be performed in case of sustained AF after induction.

Recordings were amplified using a gain of 1000, filtered with a bandpass filter (0.5-400 Hz), sampled with a sample rate of 1 kHz and were converted to digital signals using a 16 bit analog-to-digital converter.

III. Data retrieval

Data was analyzed using semi-automatic software in Python 3. Ventricular activity was assesed based on the surface ECG. An atrial deflection was set automatically when the negative slope was at least 10% of the steepest slope in the electrogram and had an amplitude of at least two times the signal-to-noise ratio of the signal. The minimal time between two deflections was set to 2 ms. Deflections were inspected visually for verification. The set refractory period to distinguish between different primary atrial deflections differed between 40 ms and 50 ms. Deflections were therefore addressed to a potential if falling within the refractory period of another deflection. In potentials with multiple

deflections, the deflection with the steepest slope was addressed as the primary deflection. The other potentials were regarded as secondary deflections.

Data created by Rasmus was retracted using Python 3. Subsequent analysis and visualization of data was performed in the same environment.

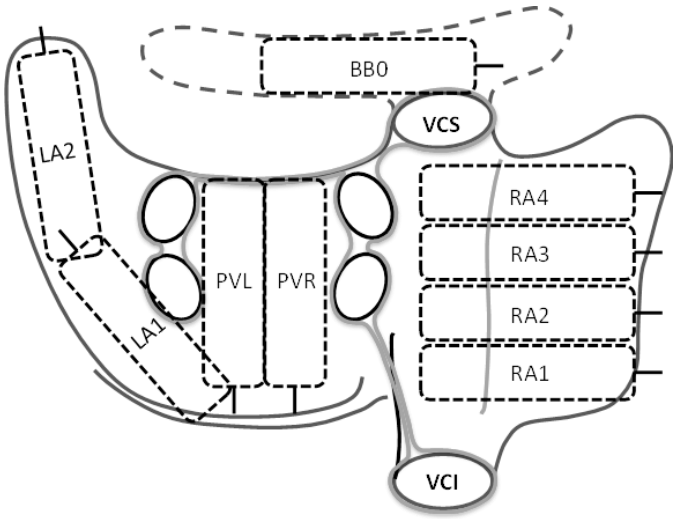

Figure 7: Atrial surface and mapped regions. Number of recordings on the atrial surface is depends on the atrial surface size. LA: left atrium, RA: right atrium, BB: Bachman's bundle, PV: pulmonary veins, VCS: superior caval vein, ICV: inferior caval vein.

IV. Single potentials – cluster determination (I)

SPs are potentials containing a single deflection. To capture the raw signal containing the deflection, windows are created in which de deflection is centered. Given the used settings for refractory periods (40 ms to 50 ms), windows of 100 ms are created around the deflection of the SP. These 100 ms segments are the input for cluster formation. Clustering using time series data uses the different time stamps as features for clustering. Therefore, the length of the input signals will determine the dimensionality of the feature space. In this case, the feature space will contain 100 dimensions.

Deflections occurring close to the start or the end of a recording can result in the inability to create 100 ms windows. The reduced window size possibly contains less information regarding the course of the potential compared to other potentials in the dataset. Besides, electrograms of unequal length will limit the comparative possibilities regarding clustering. Therefore, deflections from which 100 ms windows cannot be established, were excluded.

Usage of unipolar measurements introduces far field activity in the measurements. Attempts have been made to eliminate the contribution of the ventricular activity to the electrogram using template matching and subtraction (58), adaptive filtering (59) and independent component analysis (60). However, no adequate method for effective cancelation of ventricular activity is currently available. To maintain reliability in extracted electrograms, solely electrograms containing no contamination from ventricular activity were used. Created windows around the identified deflections overlapping with ventricular windows were excluded. An example is shown in the Figure 8. The overlap with ventricular activity caused exclusion of 17 atrial windows in this example. The surface ECG is used to identify ventricular complexes. The ventricular windows are retrieved from Rasmus, using the Pan-Tompkins algorithm (61).

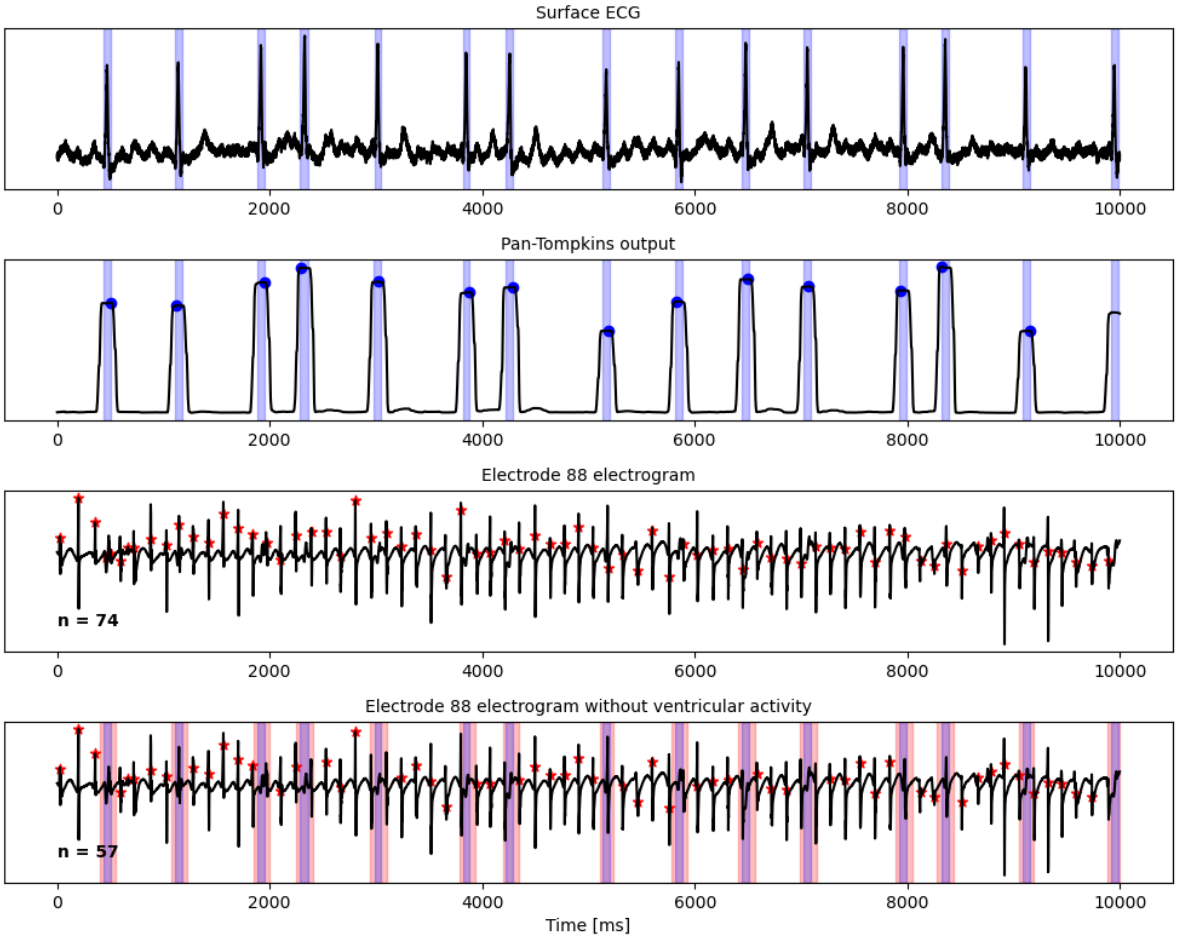

Figure 8: Exclusion of atrial complexes contaminated with ventricular activity. The blue areas show the ventricular activity as determined by the Rasmus software. The top panel shows the surface ECG. The panel below shows the output of the Pan-Tompkins algorithm. The blue dots represent found peaks of ventricular activity. The bottom two panels show the electrogram from a specific electrode of the array. The red asterisk indicate the detected deflections. In the bottom panel, it can be observed that a total of 17 found complexes were excluded based on contamination with ventricular activity (the excluded windows are displayed as the red windows in the bottom panel).

Given the aim is to evaluate morphological structures, only relative differences in the electrogram voltages are informative to perform clustering upon. Besides, different measurements can be scaled to different extents. Normalizing the values in the electrogram eliminates the possible presence of scaling bias.

To perform clustering, several choices for the creation of clusters can be considered: different algorithms, different distance measures and different ways to reduce feature space or parameterize data, see Figure 9. The different steps are discussed in the next section(s). The steps are performed in a sequential manner. First, the algorithm for clustering will be chosen. Subsequently, evaluation of different distance measures is performed. Lastly, differences of reduction of dimensionality will be evaluated to validate consistency. By performing the sequential steps, the most suitable clustering method for the current application will be determined.

Clustering outcome depends on the input data provided to the algorithm. All regions share the same characteristics with respect to the generation of potentials. Nevertheless, anatomical variations in different atrial tissues might alter the observed potentials at the surface of different areas. Hence, the clustering results are evaluated for different structures to ensure consensus of the eventual chosen clusters. The following different input possibilities are explored: all atrial regions with equal

distribution over the four regions, all single potentials observed at the RA, all single potentials observed at the LA.

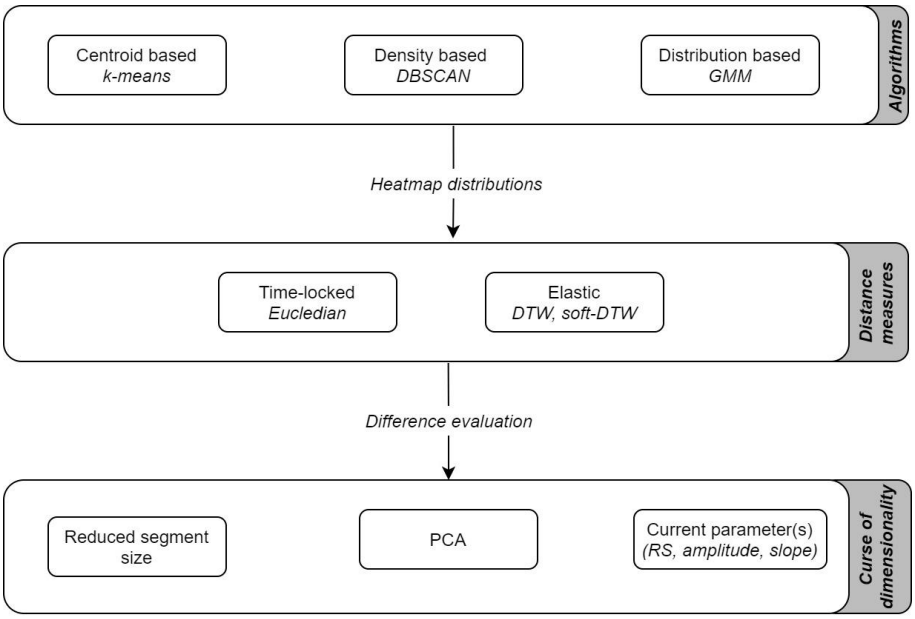

Figure 9: Sequential setup for creation of clusters.

A. Clustering algorithms

Centroid based (k-means)

In centroid based clustering algorithms, the center of the data points within a cluster is also regarded as the center of that cluster. The most commonly used centroid-based clustering algorithm is the k-means algorithm (62). In k-means, the samples are divided into N clusters. The mean of that cluster (for every dimension) is denoted by μ, also referred to as the centroid. Initial means can be randomly generated in the feature space (although more sophisticated initialization methods are currently available as well). The following steps are then repeatedly performed until a stopping criterion is reached:

i. Assign every point in the feature space to the nearest centroid.
ii. Calculate the new centroids based on the new distribution of the data.

The rationale of k-means is to minimize the within-cluster sum-of-squares (WCSS), meaning that the distances to the centers of a cluster should be minimized (63), as shown in equation 1.

$$\min_{C} \sum_{n=1}^{N} \sum_{x_i \in C_n} \|x_i - \mu_n\|^2 \qquad \textit{Eq. 1}$$

In which C represent the clusters, N represents the number of clusters, x_i the samples and μ_n the mean of the corresponding cluster. To perform k-means, the number of clusters should be predefined. The number of clusters can be investigated by exploiting the performance of the algorithm for a different number of clusters. This method is described in 'Cluster evaluation'.

The algorithm to perform k-means clustering was available in the scikit-learn Toolbox in Python (64). The number of clusters varied between 2 and 10. Initialization was performed using kmeans++ (65). Initialization was repeated 10 times. The best iteration in terms of inertia values, is displayed in the graphs. The maximum number of iterations for a single (updating the centroids) was set at 300.

Distribution based (GMM)

In distribution based clustering, observations which are presumed to belong to the same distribution are clustered together. A commonly utilized clustering algorithm is Gaussian mixture models (GMM) (66). In GMM, the data is fitted into N Gaussian densities. In higher dimensional spaces, the Gaussian distributions are described by a collection of parameters, as shown in equation 2.

$$\lambda_i = \{a_i, \mu_i, \sum_i\} \qquad i = \{1,2,\dots,N\} \qquad \textit{Eq. 2}$$

Where a_i represents the weight of the distribution, μ_i the mean vector and $\sum_i$ represents the covariance matrix. The GMM model is described by the following equations:

$$p(x \mid \lambda) = \sum_{i=1}^{N} a_i \, f(x \mid \mu_i, \sum_i) \qquad \textit{Eq. 3}$$

$$f(x \mid \mu_i, \sum_i) = \frac{1}{(2\pi)^{K/2} |\sum_i|^{1/2}} \, e^{\left(-\frac{1}{2}(x-\mu_i)^T \sum_i^{-1} (x-\mu_i)\right)} \qquad \textit{Eq. 4}$$

In which x represents a K-dimensional data vector. The data is captured in N Gaussian distribution functions from which the parameters (λ_i) have to be estimated. To estimate the parameters for the Gaussian distributions, iterative usage of expectation-maximization is utilized (67). Subsequently, a weight is appointed to every estimated distribution. Contradictory to k-means clustering, which is a hard clustering algorithm, GMM produces soft clustering. In hard clustering algorithms, samples are completely assigned to a cluster. In soft clustering, a probability of a sample belonging to each of the defined clusters is considered. When al parameters are of the estimated probabilities are final, new data points can be assigned to one of the distributions (or clusters) using Bayes' theorem, as shown in equation 5.

$$p(C_i \mid x) = \frac{p(C_i) p(x \mid C_i)}{\sum_{j=1}^{N} p(C_j) \, p(x \mid C_j)} = \frac{a_i \, f(x \mid \mu_i, \sum_i)}{\sum_{j=1}^{N} a_j \, f(x \mid \mu_i \ \sum_i)} \qquad \textit{Eq. 5}$$

The new sample will be assigned to the cluster with the highest posterior probability. Likewise centroid based clustering, the number of clusters in the data should be predefined. Determination of the number of clusters can be investigated by varying the number of clusters.

The algorithm to perform GMM clustering was available in the scikit-learn Toolbox in Python (64). Variation in number of clusters is consistent with k-means. Initialization was performed using regular k-means and was performed once. Maximum number of iterations (using the expectation-maximization algorithm) is set at 100. The GMM algorithm covers four types of covariance possibilities, altering the possibilities of the formed cluster shapes. The four types in case of two-dimensional data are described below:

i. **Spherical:** Each distribution is only described by its variance, resulting in circular-shaped contours.
ii. **Diagonal:** Each distribution yields its own diagonal covariance matrix. The contours can vary, but are orientated along one of the coordinate axis.
iii. **Tied:** The same covariance matrix is shared. However, the position of the distribution can differ. The contours for the different distributions will be similar.
iv. **Full:** Each distribution yields its own covariance matrix. The contours of the different distributions will be varying.

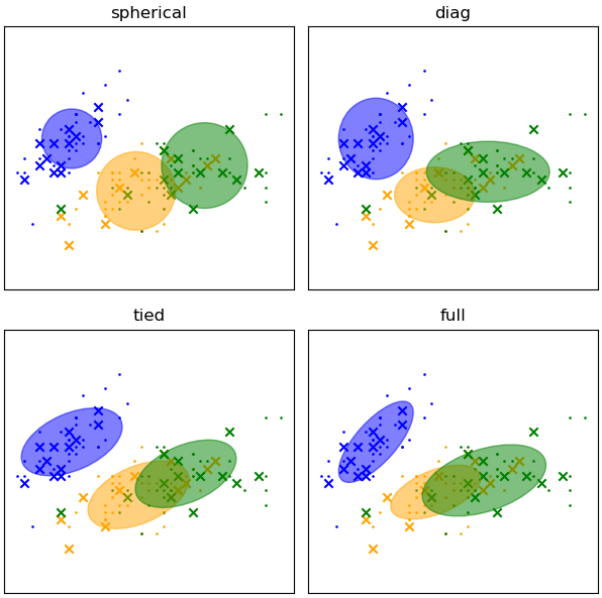

Figure 10: Different covariance options for the GMM algorithm.

The described settings for GMM clustering have been combined with all possible covariance options supplied by the algorithm.

Density based (DBSCAN)

In distribution based clustering, high density of samples in the feature space are regarded as belonging to the same cluster. One of the most commonly used density based algorithm is density-bases spatial clustering of applications with noise (DBSCAN) (68). The algorithm relies on two hyperparameters: epsilon and number of neighbors. Using the two hyperparameters, three type of points can be described:

i. **Core points**: A sample with more than the minimum number of neighbors within distance epsilon.
ii. **Border point**: A sample with less than the minimum number of neighbors within distance epsilon, but in within epsilon distance of a core point.
iii. **Noise point**: A sample with less than the minimum number of neighbors within distance epsilon and without a core point within epsilon distance.

From all samples, core points can be identified. Subsequently, all samples belonging to the same cluster can be identified. A remaining core point yet to be addressed to a cluster is then assigned to a new cluster. The process will be repeated until all samples in the dataset are visited. The number of clusters found will be a result of the chosen hyperparameters. Hence, the number of clusters is not predefined for this algorithm.

Likewise the other algorithms, the DBSCAN algorithm was available in the scikit-learn Toolbox in Python (64). The performance of the DBSCAN algorithm greatly relies on the chosen values for epsilon and minimum number of neighbors. An automated way to determine the value of these hyperparameters is lacking. In datasets of substantial size, Sander et al. (69) recommended using a value for the minimum number of neighbors of two times the dimensionality of the data. Bigger datasets are likely to contain more noise. Increasing the number of neighbors will make noise less likely to be appointed to one of the clusters. In case of the previously described windowing settings, the number of neighbors will be chosen at 200. Using the minimum number of neighbors, the average

distance to the k-nearest neighbors can be determined. This average can be graphically presented in ascending order. The optimal value for epsilon is then represented by the point of maximum (positive) curvature of the graph (70).

An example of the functioning of the three algorithms on 2D datasets is shown in Figure 11. K-means is the simplest, but an effective way to create clusters of the data. However, it can be sensitive to outliers and to its initialization. It can be observed that GMM will reach good performance in case of clusters with a specific (Gaussian) distribution. The varying covariance in all dimensions can be captured to a higher extent than when using k-means. DBSCAN can take complex shapes, but is dependent on the spatial densities in the entire feature space.

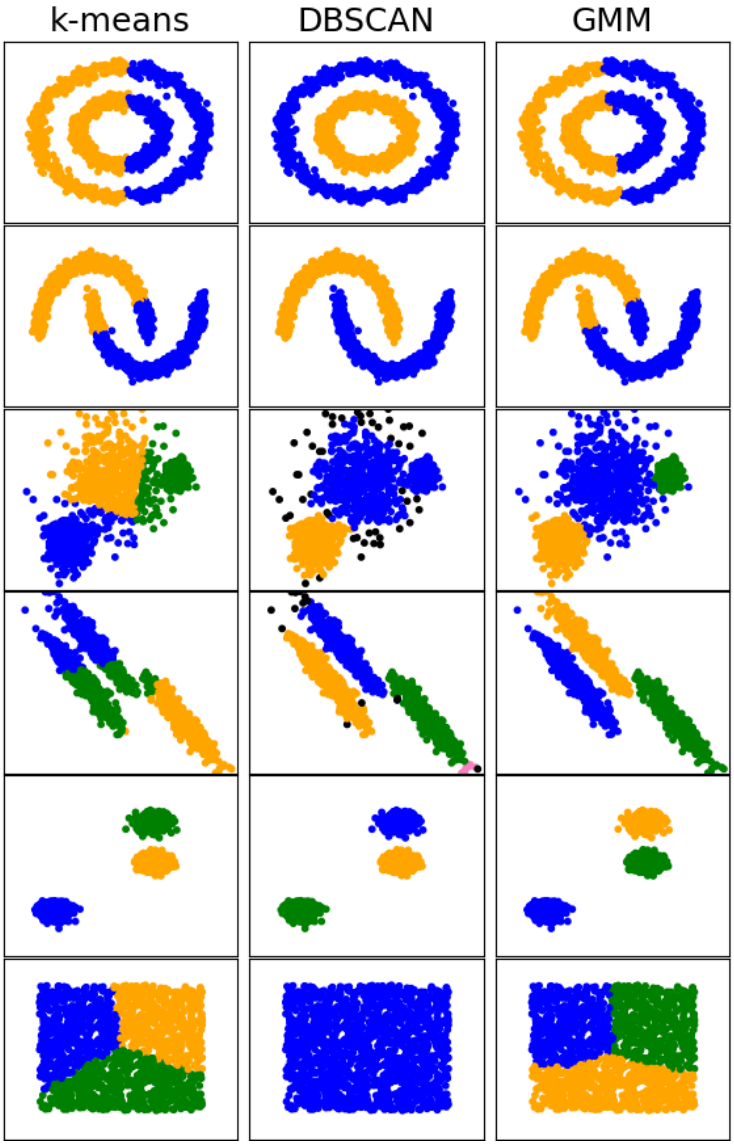

Figure 11: The performance of different with different types of 2D datasets. The colored dots represent different clusters. The black dots (solely present in DBSCAN algorithm) represent noise data points.

B. Distance measures

The similarity between samples is usually evaluated by distances. There are several ways to evaluate the distances between two samples in the feature space. In this case, the distances between values of two potentials. In case of time series data, the evaluation of the distance can be performed in a lock-step or elastic manner. In case of lock-step distances, a one-to-one comparison at the same time

instance is made between two samples. A constraint of this method is that both sequences have to be equally long. Using elastic measures, a one-to-one or one-to-many approach can be achieved. Usage of dynamic measures gives rise to possibility of comparing sequences of different lengths.

Lock-step measures can regard Euclidian and Manhattan distances. Given the absence of Manhattan distance as a metric in the scikit-toolbox, Euclidian distance is used as a distance metric in lock-step measures. Across many elastic distance measures, dynamic time warping (DTW) is one of the most commonly used time measures. It was originally used for the recognition of speech (71, 72). DTW attempts to find a path to optimally align two sequences, satisfying multiple conditions. If we consider two sequences x, with length n and sequence y, with length m. Path z with length N is described as the alignment path if satisfying the following conditions (71, 73):

i. **Boundary condition**: The start and end point of the chosen path must correspond with the first and last point of both sequences

$$z(1) = (1,1), \qquad z(N) = (n, m) \qquad \textit{Eq. 6}$$

ii. **Monotonicity condition:** Time ordering is preserved by constraining every new element in the appointed path to have a indices values equal or greater than the previous element for both sequences:

$$x_1 \leq x_2 \leq \cdots \leq x_n\,, \qquad y_1 \leq y_2 \leq \cdots \leq y_m \qquad \textit{Eq. 7}$$

iii. **Step size condition:** Long time shifts are prevented by restricting the jumps solely to the adjacent points. If we consider the starting point in the path:

$$z(1) = (1,1)\,, \qquad z(2) = \{(2,1), (2,2), (1,2)\} \qquad \textit{Eq. 8}$$

To find the optimal alignment path, a cost function is applied to the local cost matrix. The local cost matrix (M_{local}), contains distances between all combinations of the elements of both sequences, as displayed in equation 9. M_{local} will therefore have an n by m shape. The alignment path with the lowest cost is chosen as the optimal path.

$$M_{local}(i,j) = \left(\left|x_i - y_j\right|^p\right)^{\frac{1}{p}} \quad i = \{1,2,\dots,n\}, \quad j = \{1,2,\dots,m\} \qquad \textit{Eq. 9}$$

Where p represents the l_p norm. An l_p norm of 2 was used in the current setting (Euclidian distance). In reality, a substantial number of paths should be investigated to determine the optimal path. The resulting computational complexity is reduced by an algorithmic approach. This approach translates to several components. Firstly, the local cost matrix (M_{local}) is constructed as displayed in equation 9. Subsequently, M_{local} is used to initialize the first row and column of the accumulated cost matrix (M_{acc}) as displayed in equations 10-12:

$$M_{acc}(1,1) = 0 \qquad \textit{Eq. 10}$$

$$M_{acc}(i,1) = \sum_{k=2}^{i} M_{local}(x_i, y_1) \qquad i = \{1,2,\dots,n\} \qquad \textit{Eq. 11}$$

$$M_{acc}(1,j) = \sum_{k=2}^{j} M_{local}(x_1, y_j) \qquad j = \{1,2,\dots,m\} \qquad \textit{Eq. 12}$$

The remaining elements of M_{acc} are filled elementwise using the following rule:

$$M_{acc}(i,j) = M_{local}(i,j) + min\{M_{acc}(i-1,j-1), M_{acc}(i-1,j), M_{acc}(i,j-1)\} \qquad \textit{Eq. 13}$$

Lastly, the optimal path is determined by tracking back M_{acc}. Starting at $M_{acc}(n,m)$, the elements of the eventual alignment path z will follow the direction of the minimum values of the adjacent points (likewise the step size condition) whilst the boundary condition and the monotonicity condition are preserved. The process is repeated until reaching $M_{acc}(1,1)$. The eventual alignment path is used to calculate the distance between the sequences. An example is shown in Figure 12. It shows that the first sequence returns more quickly to its iso-electric baseline after the deflection compared to the second sequence. Hence, the last point of the second sequence will be closest to the iso-electric segment of that potential. Hence, this point will be used as comparison with many points of the first sequence.

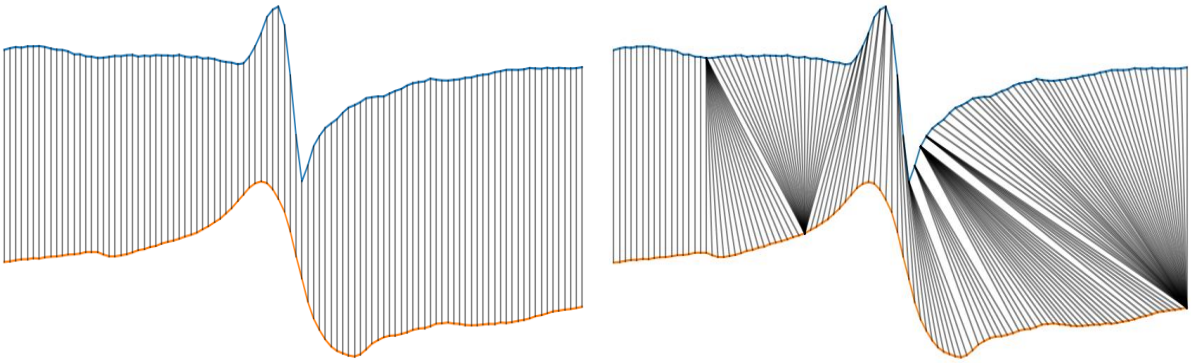

Figure 12: Illustration of DTW. Instead of having time locked comparisons, a single spot on the first electrogram will be compared to many points on the other electrogram. The most suitable point of comparison is then used for distance calculation. The figure on the left shows the time-lock comparison. The figure on the right shows the compared points using DTW.

An addition to original DTW is soft-DTW (74). Soft-DTW introduces regularization to the original DTW by introducing a soft-minimum function, parameterized by ɣ instead, instead of a regular minimum function. Increasing ɣ will result in increased smoothening of the signal. This will prevent the alignment of remote points in original sequences (horizontal or vertical lines in the alignment matrix). An example of usage of soft-DTW is shown in Figure 13 or the same potentials as shown in Figure 12. Increasing ɣ will result in increased smoothening of the eventual alignment path. Centering of the deflection causes the path to be aligned at that point, regardless of ɣ. However, the upslope before and after the deflection can differ between the potentials. The curvature in comparison is smoothened by the increase in ɣ.

To evaluate whether a different similarity measure influences the outcome of the clustering performance, lock-step measure is compared with elastic measures. The elastic measures will consist of DTW and soft-DTW (using ɣ = 0.5).

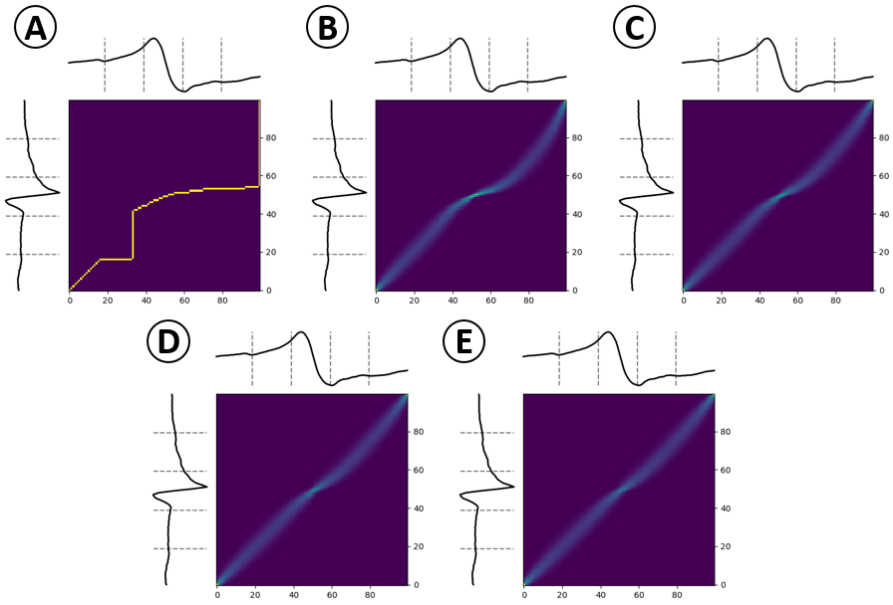

Figure 13 The usage of soft-DTW. The values for γ are increasing from left to right (A: 0, B: 0.25, C: 0.5, D: 0.75 and E: 1). A higher value of γ will restrict the possibility of comparing a point on the first electrogram with a more distant point on the other electrogram. Note that usage of lock-step distances would create a diagonal line in the shown figures.

C. Dimensionality reduction

Clustering time series data can, depending on the sample frequency and the recording time, result in high feature space dimensionality. Using the Euclidian distance, increasing the number of dimensions will result in convergence of the distances between points to a constant value (75-77). With this, the ability to form clusters diminishes. Therefore, it is important to show that the observed clusters from the 100 ms segments are consistently found in lower dimensional space. An example of how introduction of new dimensions can alter the found distances is descibed below:

Imagine time series data of length K. The length of the time series data determines the dimensionality of the feature space:

$$x = x_1, x_2 \dots x_K \qquad \textit{Eq. 14}$$

$$x \in \mathbb{R}^K \qquad \textit{Eq. 15}$$

Using the Euclidian distance, the distance between two points (v and u) is calculated by:

$$d(v,u) = \sqrt{(v_1 - u_1)^2 + (v_2 - u_2)^2 + \cdots + (v_K - u_K)^2} \qquad \textit{Eq. 16}$$

Where d represents the distance. The problem is as follows: two separate groups exist in the database, which are represented by the blue and the orange markers. When the feature space is one dimensional (or one parameter), the distance between the centers of the groups is relatively low (in this case, d = 2). When another parameter is addedto increase the feature space to two dimensions, the second parameter yields greater distances than the first parameter (d = 19). Using the Euclidian distance, it can be observed that the distance between the centroids will converge to the parameter with the largest distance.

$$v,u \in \mathbb{R}^1 \rightarrow d(v,u) = \sqrt{(v_x - u_x)^2} = \sqrt{(4 - 2)^2} = 2 \qquad \textit{Eq. 17}$$

$$v,u \in \mathbb{R}^2 \rightarrow d(v,u) = \sqrt{(v_x - u_x)^2 + (v_y - u_y)^2} = \sqrt{(4-2)^2 + (20-1)^2} = 19.1 \quad \textit{Eq. 18}$$

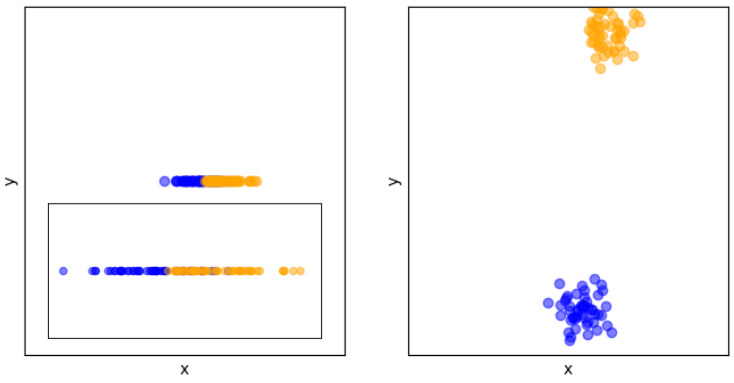

Figure 14: Distribution of samples from the two different groups in one-dimensional (left) and two-dimensional space (right) . The figure on the left shows an additional box, this is a zoomed in version of the data points that are observed in the rest of the plane.

It shows that addition of a dimension in this case (with a substantially higher difference) causes the differences to converge to the value of the dimension with the highest difference. Applying the same to three groups (addition of the green markers), but we make the distances in the third dimension greater than the other two dimensions (d = 99), the same pattern occurs. The distance from the blue cluster to the green cluster is increased for the first dimension or x-axis (d = 6) to give a clearer overview. Equation 19 and 20 show the result when two points, v from the blue cluster and w from the green cluster, are compared:

$$v,w \in \mathbb{R}^2 \rightarrow d(v,w) = \sqrt{(v_x - w_x)^2 + (v_y - w_y)^2} = \sqrt{(8-2)^2 + (20-1)^2} = 19.9 \quad \textit{Eq. 19}$$

$$v,w \in \mathbb{R}^3 \rightarrow d(v,w) = \sqrt{(v_x - w_x)^2 + (v_y - w_y)^2 + (v_z - w_z)^2} = \sqrt{(8-2)^2 + (20-1)^2 + (100-1)^2} = 100.1 \quad \textit{Eq. 20}$$

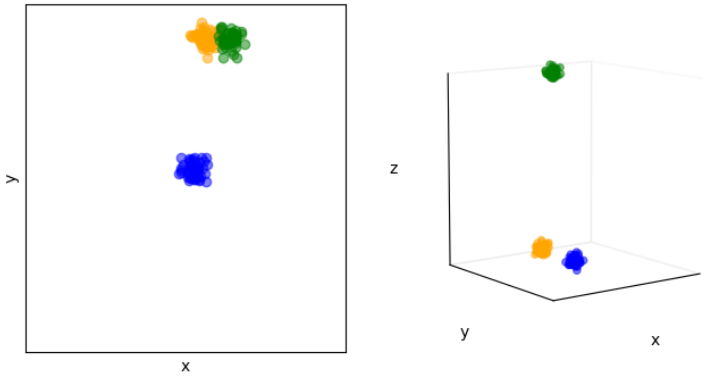

Figure 15: Distribution of samples from the two different groups in two-dimensional (left) and three-dimensional space (right).

The distance from the blue cluster to the orange cluster will be equal to the distance in the previous example. Comparing the addition of the third dimension repeatedly shows that the distances will converge to the dimension with the highest distance (in this case the third parameter or the z-dimension). It is not possible to visualize this pattern in higher dimensions. However, with the addition of dimensions, the chance of occurrence of the described phenomenon increases. Normalization of the parameters could help to reduce this phenomenon, but the distance will still converge to the dimension with the highest distance difference. Increasing dimensionality will therefore always increase the chance of encountering the curse of dimensionality.

Although the created clusters will be visualized for evaluation, it should be verified whether lowering the number of dimensions will not alter the resulting clusters.

Window size reduction

One way to show consistent results of clustering is to change the size of the window around the primary deflection. Firstly, this is done by taking 20 ms before and after the primary deflection. The dimensionality of the dataset will be reduced to 40 dimensions. If the clustering is consistent with the clustering from the longer time windows, it indicates absence of the curse of dimensionality in the long electrogram segment analysis.

Afterwards, the 50 ms before and 20 ms after the primary potential will be investigated. This contributes to the confirmation of absence of the curse of dimensionality. However, it might serve an additional purpose. Given that contraction of the atrial tissue is expected to follow the electrical activity (deflection), it can be expected that the course of the potential following the deflection is less reliable. Hence, analyzing a shorter segment of the end of the potential might yield different results. The different window sizes are visualized in the Figure 16.

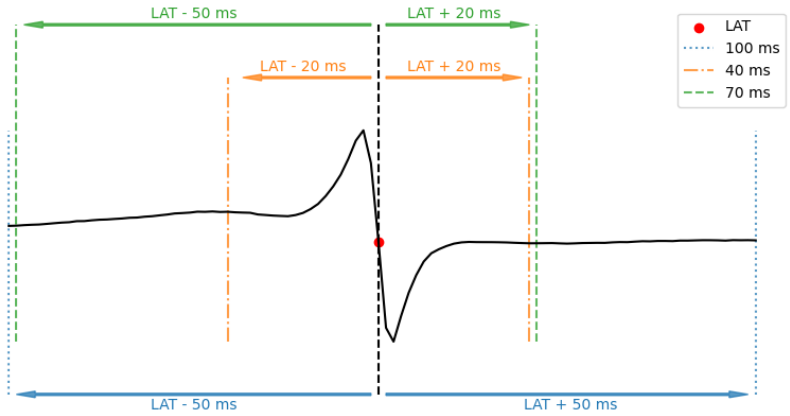

Figure 16: Different used window sizes for the evaluation of clusters. Shifting of individual lines (by 1 ms) is performed for sake of clarity.

PCA

Another way to reduce the dimensionality of the dataset is by performing principal component analysis (PCA). In the former two methods, sequential observations formed the features utilized to cluster the data. It can be argued that usage of sequential data point will contain a great amount of redundant information. In PCA, new axis (or variables) are defined which are uncorrelated, called the principal components. This maximizing the variance whilst the dimensionality of the dataset is reduced (78). For PCA, the data should be standardized for all features (all time points). Description of the extraction of principal components is discussed in this section.

Consider the data to have the following structure, described as matrix B:

$$B = \begin{bmatrix} x_{1,1} & \cdots & x_{1,n} \\ \vdots & \ddots & \vdots \\ x_{m,1} & \cdots & x_{m,n} \end{bmatrix} \quad \textit{Eq. 21}$$

Matrix B has an m by n shape, in which m represents the total number of potentials in the dataset and n represents the length of a single time series signal. The average $\bar{x}_i$ per column of matrix B is calculated, resulting in a row vector. By multiplying the row vector with a column vector filled with ones, matrix $\overline{B}$ is obtained. $\overline{B}$ will have the same shape as B, however, the columns of $\overline{B}$ are filled with the average of the corresponding columns in B. Subsequently, $\overline{B}$ is subtracted from B to form matrix C. Matrix C contains all values from matrix B in which the mean per time stamp is subtracted.

$$\bar{x}_i = \frac{1}{m} \sum_{j=1}^{m} x_{j,i} \; i = \{1,2 \dots, n\} \quad \textit{Eq. 22}$$

$$\bar{B} = \begin{bmatrix} 1 \\ \vdots \\ 1 \end{bmatrix} [\bar{x}_1 \quad \dots \quad \bar{x}_n] \quad \textit{Eq. 23}$$

$$C = B - \bar{B} \quad \textit{Eq. 24}$$

From matrix C, the covariance matrix D can be constructed. It can be calculated in a compactly using the matrix configuration, as shown in equation 25.

$$D = \frac{1}{n-1} C^T C \quad \textit{Eq. 25}$$

In which C^T represents the transposed matrix C. The eigenvectors and eigenvalues of covariance matrix D represent the directions of the new feature space and the magnitude of each direction, respectively. The eigenvectors can be calculated by equation 26 and 27.

$$D\vec{v} = \lambda\vec{v} \quad \textit{Eq. 26}$$

$$\det(D - \lambda I) = 0 \quad \textit{Eq. 27}$$

In which $\vec{v}$ represents the eigenvectors and λ represent the corresponding eigenvalues. The unit matrix is represented by I. Once the eigenvectors are retracted, the eigenvalues can be calculated using equation 28.

$$(D - \lambda_i)\vec{v}_i = 0 \quad i = \{1,2 \dots, N_{eig}\} \quad \textit{Eq. 28}$$

The total number of eigenvectors is represented by N_{eig}. The eigenvectors are sorted by decreasing eigenvalues. Eigenvectors with higher eigenvalues capture the most variance of the dataset. The usual cutoff value for demining the number of principal components is the number of components explaining 95% of the variance. The number of eigenvectors which contain 95% of the variance is calculated by:

$$R = \frac{\sum_{i=1}^{k} \lambda_i}{\sum_{i=1}^{N_{eig}} \lambda_i} \; k = \{1,2, \dots, N_{eig}\} \quad \textit{Eq. 29}$$

In which R represents the explained variance ratio. Lastly, the original data is transformed to the new feature space, using matrix E. Matrix E contains the eigenvectors (or principal components) of the k highest eigenvalues as columns (therefore having an n by k shape). When performing PCA on a collection of different univariate time series, the resulting eigenvectors can be regarded as temporal fundamental functions. The original potentials are projected onto the new axis and represent a linear

combination of the retracted principal components. Transformation to the new feature space using the k determined principal components is displayed in equation 31.

$$E = \begin{bmatrix} \vec{v}_{1,1} & \cdots & \vec{v}_{k,1} \\ \vdots & \ddots & \vdots \\ \vec{v}_{1,n} & \cdots & \vec{v}_{k,n} \end{bmatrix} \quad \textit{Eq. 30}$$

$$F = E^T C^T \quad \textit{Eq. 31}$$

The new feature space is defined by performing PCA on the dataset with equal distribution across all regions. New groups of data have to be transformed to the feature space in the same manner. In this case, this will contain scaling based on the standardization using the previously determined standardization components. Subsequently, the data is projected onto the new feature space and dedicated to a cluster.

Currently used parameters

Deflections can also be parameterized instead of using the entire time series sequence. By parameterizing the data, dimensionality is reduced. Parameters describing the potential morphology can be explained by how the potential is generated on a cellular level, as discussed in the 'Background' section. Amplitude, slope and RS-ratio are the parameters used to describe SPs, as displayed in Figure 17. They are calculated using equation 32 to 34 and can be retracted using the Rasmus software. *A* represents the amplitude, *S* represents the slope and *RS* represents the RS-ratio. In order to calculate the RS-ratio, the baseline voltage should be calculated. The baseline voltage is defined as the median value between 70 ms (70 samles) and 30 ms (30 samples) after the LAT by the Rasmus software. LAT is defined as the point of steepest slope in the deflection.

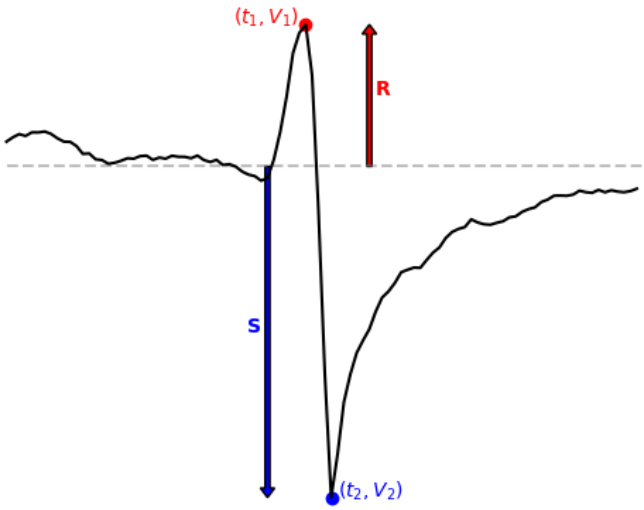

Figure 17: Recorded single potential. The R and S-peaks are visualized. The grey dashed lined represents a hypothetical baseline value.

$$A = V_1 - V_2 \quad \textit{Eq. 32}$$

$$S = \frac{V_1 - V_2}{t_1 - t_2} \quad \textit{Eq. 33}$$

$$RS = \begin{cases} 1 - RS(n) & for\ RS(n) \leq 1 \\ \dfrac{1}{RS(n)} - 1 & for\ RS(n) > 1 \end{cases} \quad \textit{Eq. 34}$$

Likewise clustering the time series data, distances between points in the dataset will converge to the dimension with the highest values. For example, the RS-ratio is already restricted to a range of [-1,1], whilst the amplitudes and slopes can take much higher values. Without additional rescaling of data, the amplitude parameter will dominate the distances in the feature space. Hence, the data should be rescaled to be able to cluster based on the three proposed variables. To evaluate the clustering results, three setups are regarded:

i. Clustering based using unscaled features.
ii. Clustering based on robust range scaling.
iii. Clustering based on MaxMin scaling.

MaxMin scaling rescales the data to have a range of [0-1]. Robust range scaling removes the median from the data and ranges the data between the first and third quartile range. Therefore, this method is more robust against outliers compared to using unscaled features. However, major difference in distances between parameters can still be present. If a potential lacked one of the three parameters, the potential was not included in the clustering method based on the described parameters.

D. Cluster evaluation

To select an appropriate setting for the included algorithms, the clusters are evaluated by different scores for different a range of clusters. Number of clusters ranging from 2 to 10 were evaluated. For k-means, the silhouette score and the elbow method are adopted. For GMM, the silhouette score was evaluated, accompanied by the Bayesian information criterion (BIC) and the Akaike information criterion (AIC). Not only the number of clusters, but also the type of covariance will be evaluated. No additional cluster evaluations were performed for DBSCAN, given the outcome is a direct result of the value for the chosen hyperparameters.

Silhouette

The silhouette is a way to compare the distances within a cluster to the distances to another cluster (79). The metric can be calculated using equation 35.

$$s(x_i) = \frac{b(x_i) - a(x_i)}{max\ \{a(x_i), b(x_i)\}} \qquad \textit{Eq. 35}$$

Where $s(x_i)$ represents the silhouette score of the sample, $a(x_i)$ represents the average distance of sample x_i to other samples in the same cluster, $b(x_i)$ is the average distance to the samples in the nearest neighboring cluster. The silhouette score is calculated for every sample in the dataset. The average silhouette score for all samples represents the total silhouette score. The silhouette score can vary between [-1,1]. A higher score represents a better separation of clusters. With the silhouette score, a local maximum or plateau in the evaluated number of clusters is searched for.

Elbow method

The elbow methods uses the WCSS as a metric (see equation 1) (80). This value is minimalized during creation of clusters with k-means. Addition of clusters will result in reduction of the WCSS. However, addition of excessive clusters will not significantly reduce WCSS. This 'bend' can be regarded as an indicator for selection of the most appropriate number of clusters.

BIC/AIC

Either BIC and AIC are methods of model selection methods under maximum likelihood estimations (81, 82). They can be used in supervised learning to motivate a model choice without specific need for a separate test set. However, they can also be applied to unsupervised learning problems to find the most suitable model amongst a selection of models. In this case, choosing the optimal number of

clusters. Both evaluation metrics compensate for the complexity of the model by penalizing models containing a high number of estimated parameters. More estimated parameters will result in a higher scores for both evaluation metrics score, effectively preventing overfitting of the model on the acquired data. Both are commonly adopted in analyzing the number of clusters in with a GMM model. The metrics are calculated using the equations 36 to 38:

$$AIC = 2k - 2\ln(\hat{L}) \quad \textit{Eq. 36}$$

$$BIC = k\ln(n) - 2\ln(\hat{L}) \quad \textit{Eq. 37}$$

$$\hat{L} = p(x \mid \hat{\theta}, M) \quad \textit{Eq. 38}$$

In which k represents the number of parameters estimated by the model. The sample size of the data is represented by n, x represents the observed data, $\hat{\theta}$ represents the total set of estimated parameters, which depends on the number of distributions fitted by the model. Not solely the number of clusters can be evaluated through this metric, also the different settings for covariance types can be assessed in order to find the most suitable model. Both evaluation metrics represent the ability of the model to predict the observed data. Another way of understanding $\hat{L}$ is that it is the probability of obtaining the data which you have, supposing the model being tested was a given. Intuitively, a lower value for either AIC or BIC represents a better model. Hence, AIC and BIC values are attempted to be minimized.

E. Cluster visualization

The formed clusters should be analyzed to validate adequate cluster formation. This is performed by creating heatmaps of all potentials falling into that cluster. The advantage when using SPs is the possibility of aligning the potentials around the deflection. Therefore, the main structure of the potentials in a cluster can be extracted. For every time step, a histogram containing 100 bins is created. Subsequently, the histogram is normalized to create a heatmap with consistent characteristics. The global structure of the potential in a cluster is shown by the dotted white line. This line is constructed by plotting the mean of all potentials per time step. Figure 18 shows an example of a heatmap which is created. The potentials are originating from all four included regions. Two characteristics are desirable when clusters are evaluated by the heatmaps. First, the (mean) morphological structures of all clusters should be varying. Secondly, the distribution (red in the heatmap) should be focused around the mean morphological structures as much as possible. The low dispersion would indicate high similarity between the potentials falling in the same cluster.

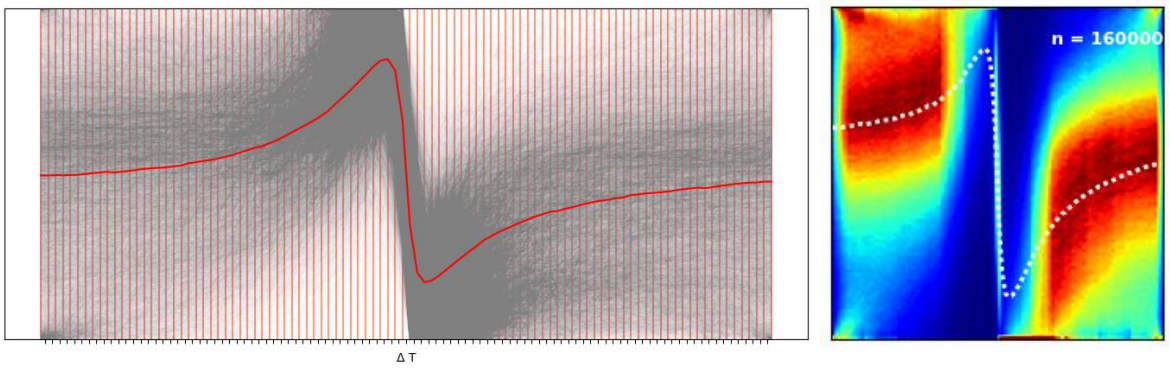

Figure 18: A representation of the creation of the heatmaps. A normalized histogram is made for each time step. The figure on the right is the heatmap result of the figure on the left. The figure on the left is enlarged in the time axis for clarity. The vertical pink stripes indicate the time steps. A histogram is produced for every time step.

F. Cluster covariance

When looking at SPs, the covariance between different potentials can be utilized to evaluate similarity between time series data. The covariance ranges between -1 and 1. In the current circumstances, a higher value of the covariance represents higher similarity of the electrograms. It could be expected that the values for the covariance are higher within the clusters compared to the coefficients between clusters. This can be visualized by creating color-coded recurrence matrices, as performed in bipolar measurements by Ng et al. (83). Ng et al. performed this on bipolar endocardial measurements. Furthermore, they adapted the maximum cross-correlation rather than the covariance. Given all potentials are aligned at the deflection, it is expected that the cross-correlation is maximal when there is no time shift between the potentials. Hence, instead of the cross-correlation, the covariance is adapted. Given the exponentially growing number of calculations is necessary to create the recurrence plots, random samples of 2000 potentials across all clusters have been evaluated. The possible range of covariance values displayed in the recurrence matrix is 0 to 1. To evaluate patterns in the observed clusters, ratio of the within cluster and the between cluster covariances are determined.

V. Single potentials – spatial cluster occurrence (II)

A. Cluster occurrence

Retrieved mapping data is divided into four regions, as previously described: RA, LA, pulmonary veins (PV) and BB. Morphology of SPs are categorized into one of the clusters according to the outcome of the cluster determination methodology. Occurring morphologies are expressed as a percentage of the total number of SPs present to maintain a general outcome measure over all ranges of identified SPs. Distribution of clusters is analyzed per file. The data is visualized using scatterplots. Furthermore, currently used parameters for description of SPs (amplitude, RS-ratio and duration) are supplied of the respective potentials. Since the number of samples is far higher compared to the usage of percentages, violin are utilized to visualize the distributions of the currently used parameters instead of scatterplots.

B. Statistical analysis

Data is checked for normality using Lilliefors test. In case of normally distributed data, mean and 95% confidence interval will be provided. In case of skewed data, medians with interquartile range (IQR) will be presented. Given data might differ between patients and also within patient regions, data files are considered independent. The regional comparison will be performed by one-way ANOVA parameteric test if distributed normally. Appropriate post-hoc analysis will be performed based on Levene's statistic. In case of skewed distribution, nonparametric Kruskall-Wallis test will be applied. In case of significant differences, post-hoc analysis using Dunn's test will be performed. Significance level will be adjusted to the number of included regions (n = 4) or the number of clusters to be compared (n = 5).

RESULTS 3

Results

A total number of 128 files was used, originating from 23 patients. Patient characteristics retrieved through medical records are displayed in Table 1.

Table 1: Baseline characteristics of included data (n = 23). Values are presented as median [IQR] or absolute value (percentage).

Demographic characteristics	
• Age	71.0 [65.5|70.1]
• Male sex	21 (91.30)
AF subtype	
• No history (AAF)	13 (56.52)
• AF history	10 (43.48)
○ PAF	4 (17.39)
○ PeAF	2 (8.70)
○ LSPAF	4 (17.39)
○ PerAF	0 (0.00)
Cardiovascular risk factors	
• BMI	28.1 [25.35|31.20]
• Hypertension	15 (65.21)
• Dyslipidemia	12 (52.17)
• Diabetes Mellitus	6 (23.09)
Underlying disease	
• CABG	19 (82.61)
• AVD	1 (4.35)
• MVD	1 (4.35)
• CABG + MVD	1 (4.35)
• CABG + AVD	1 (4.35)
Anti-arrhythmic drugs	
• Class I	0 (0.00)
• Class II	17 (73.91)
• Class III	2 (8.70)
• Class IV	0 (0.00)
• Digoxin	3 (13.04)

I. Single potentials – cluster determination (I)

A. Clustering algorithms

Centroid based (k-means)

Adapting k-means to the data, a local maximum in the silhouette score is observed at a number of four clusters. Similarly, a total of four clusters appears to be the point of maximum using the elbow method. The graph scores and corresponding outcome clusters are shown in Figure 19. Usage of four clusters shows four distinct different morphologies when looking at the main structures across the heatmaps. Besides, distribution of potentials within the cluster appears to be narrow. Densities appear to be consolidated across the main structure of the cluster. The first cluster is represented to a lesser extent compared to the other three clusters (9.6%, 27.6%, 25.6% and 37.1%, following Figure 19 from top to bottom). Although the potentials are different in morphology, the first cluster shows a morphology

not meeting the prior expectation of single potentials. The cluster lacks iso-electric segments before and after the deflection.

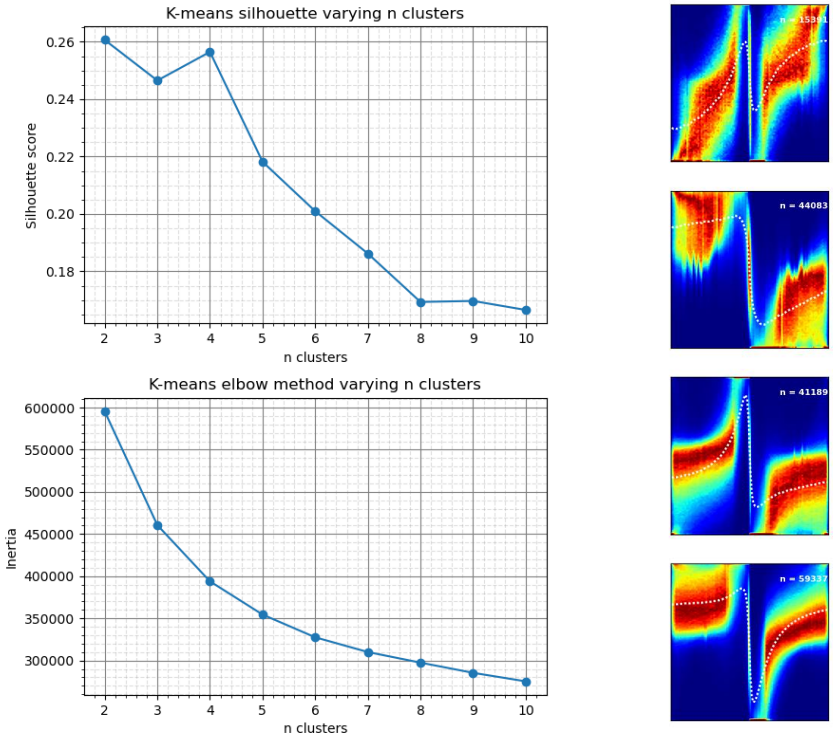

Figure 19: Results using k-means clustering for a varying number of clusters. Usage of four clusters appears to be most suitable number of clusters using this method. The left side of the figure shows the silhouette score in the upper panel and the inertia (elbow method) in the lower panel. The right site of the figure shows the formed clusters.

Distribution based (GMM)

When adapting GMM to the potentials, the different possible constrictions for covariance type are evaluated. An overview is given in Figure 20. For all covariance types, the BIC and AIC do not show a preferential number of clusters for the given range. Similarly, the silhouette scores show no distinct preference in the number of clusters to choose with the full, tied and diagonal covariance options. When using spherical covariance type of the Gaussian distributions, a preferential number of four clusters appears from the silhouette scores. Although no local optimum is observed when advancing from full covariance type to diagonal covariance type, silhouette scores across all number of clusters increases. An increase in silhouette score using identical input data indicates better separation of the potentials into different groups. Since either no desired number of clusters or four clusters is recommended using the scores, four clusters are taken to create the heatmap representation for comparison. Description of this heatmaps is divided in different components.

Full covariance

Using full covariance, the mean morphological structures across different clusters are similar. Furthermore, densities in clusters are highly scattered over the entire possible range of potentials. Potentials falling under the same group therefore appear to have high variance in morphologies. The heatmaps of the clusters are explanatory to the observed low silhouette scores (blue graph in Figure 20).

Tied covariance

Compared to usage of full covariance, silhouette scores show a minor increase (orange graph in Figure 20), indicating better cluster separation of the different clusters. The morphological structures of the

first and second cluster are similar. The second cluster contains a relatively low number of potentials compared to the first cluster (66.2% and 5.7% of all potentials). It would be expected that the two formed clusters would have formed a single clusters. Furthermore, the third and fourth cluster show a distorted pattern with lacking relevant general structure from a electrophysiological perspective.

Diagonal covariance

Constraining to diagonal covariance starts showing a different morphology in all separate clusters. Consolidation around the mean structures of the clusters increases as well. Both beneficial characteristics are observed as a substantial increase in silhouette scores across all possible number of clusters (green graph in Figure 20). Some clusters appear to have mixing of components. The third cluster shows mixing of components around a single potential with a RS-ratio of 0, combined with consolidation of potentials starting at the left bottom and right top corner. The morphology of these potentials resembles the potentials observed in the cluster without iso-electric segment prior and following the deflection when adapting k-means.

Spherical covariance

Spherical covariance is the only type showing preferential number of clusters using silhouette scores, which is four. The silhouette score at four clusters is especially higher compared to using diagonal covariance type (red graph in Figure 20). Analyzing the heatmaps using spherical covariance type, different morphological structures can be recognized. The morphological structures resemble the clusters formed by k-means. K-means assigns labels according to its closest centroid. All points with the same distance to a point forms a circular structure. Hence, it is expected that adaption of spherical covariance will be most similar to usage of k-means. The scattering of potentials clustered together decreases. However, inspecting the density borders, a relatively high proportion of discontinuities is observed.

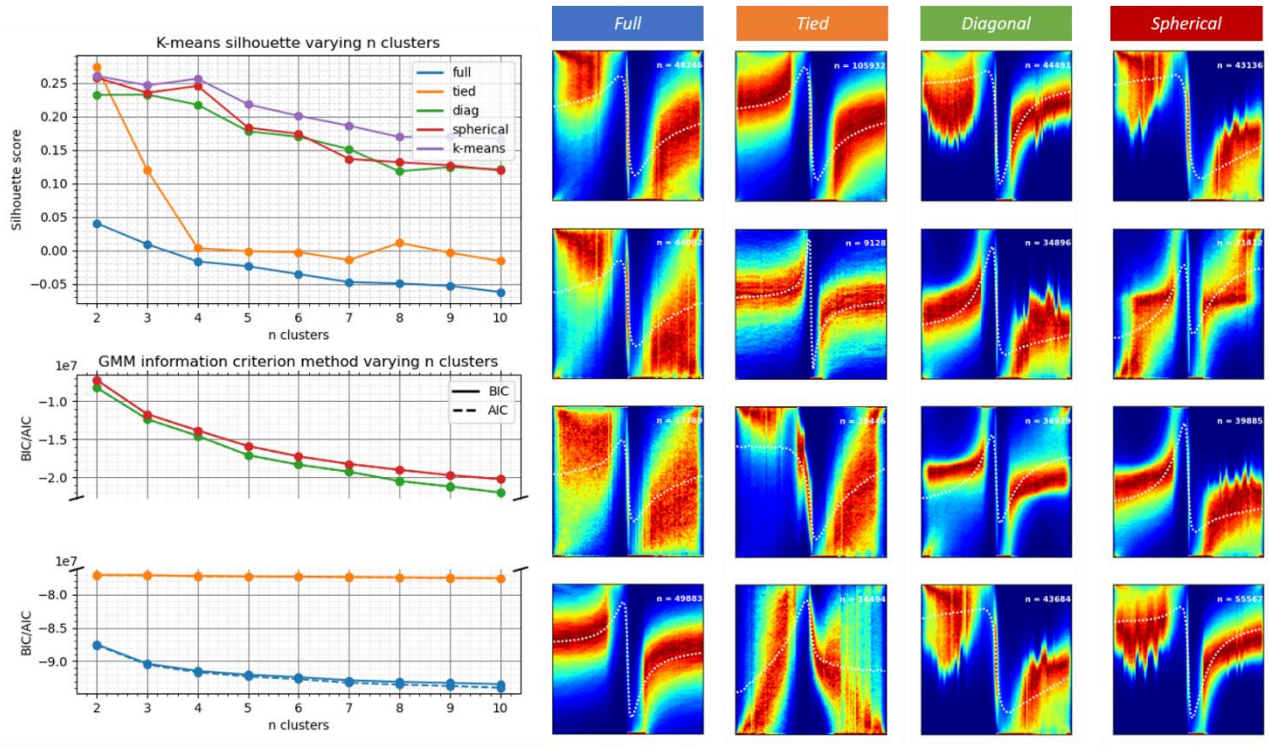

Figure 20: Overview of the clusters formed by means of the GMM algorithm. The left side of the figure shows the silhouette score in the top panel. The lower panel shows the BIC and AIC score, the y-axis is split in two parts. The graphs are color-coded by the type of covariance used. The right side of the figure shows the heatmaps using the different covariance types.

Density based (DBSCAN)

Evaluating the distance to the 200 closest neighbors shows the point of maximum curvature at distance of 0.75, see Figure 21. DBSCAN was therefore adapted using 200 as the number of neighbors and an epsilon of 0.75. Using DBSCAN, all the potentials forming the noise are grouped together. The identified noise is shown in the heatmap at the top of a column. No morphologically different clusters could be identified using the initial settings. Lowering the number of neighbors or increasing epsilon eases creation of different clusters. In both cases, a noise cluster and a cluster containing the far majority of all potentials are created with the same general structure. Increasing clustering ease did not improve clustering ability. Furthermore, potentials grouped in the same cluster are highly scattered.

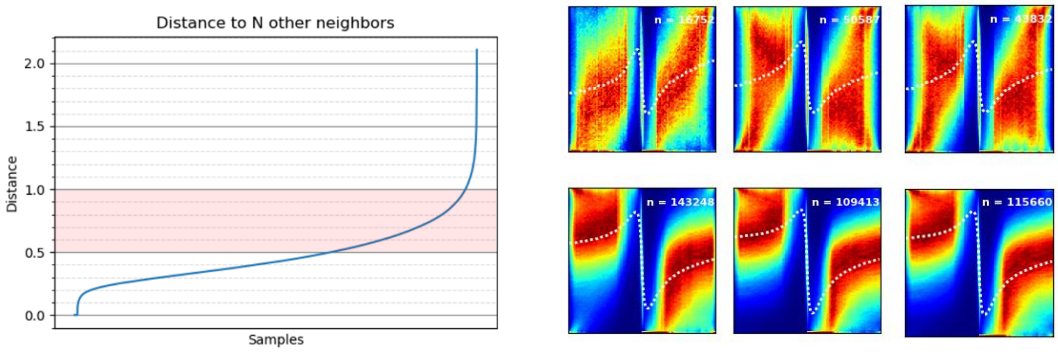

Figure 21: The panel on the left shows the average distance to the 200 closest neighbours ranked for all samples. The panel on the right shows the DBSCAN results using a various values for epsilon and number of neighbours. From left to right: ε = 0.75 with neighbours = 200, ε = 1 with neighbours = 200 and ε = 1 with neighbours = 100 (four clusters with each approximately 100 potentials are not shown in the figure, the low number of potentials causes a lack a generally recognizable structure).

Choice of algorithm

Using DBSCAN under different circumstances, no adequate clustering of potentials was achieved. K-means showed a preferential cluster number of four. The resulting clusters showed different morphological structures combined with consolidation of all potentials around the mean structure the assigned group. Usage of GMM reaches a similar result compared to k-means once the covariance types are further restricted to spherical distribution shapes. However, k-means showed a slightly higher silhouette score, more continuity along the density borders of the heatmaps and is computationally less intensive compared to GMM using spherical covariance. Hence, k-means is adapted as the algorithm for clustering task.

B. Distance measures

Figure 22 shows the results of using different distance measures. Using DTW, morphological structures do not coincide with the clusters resulting from a lock-step measure. General structures are possibly altered due to increased scattering prior (indicated with the red circles at the right bottom of the heatmap) or after (indicated with yellow circle at the right bottom of the heatmap) the deflection. The deflection is centered in all potentials. It is therefore expected that these time points will be compared to the same time points of another deflection. However, the upslopes (R-waves) will all be compared between potentials since these are the most similar structures in potentials. An example is shown Figure 12 in the corresponding 'Methods' section. The same goes when returning to the iso-electric segment after the S-wave in the third cluster. This behavior provokes scattering of the distribution in the heatmap.

Using soft-DTW, the regularization of the DTW method causes the return of different morphological structures as observed with the lock-step measure. The second cluster shows a mixing phenomenon of two types of potentials (as earlier described in the algorithm choice).

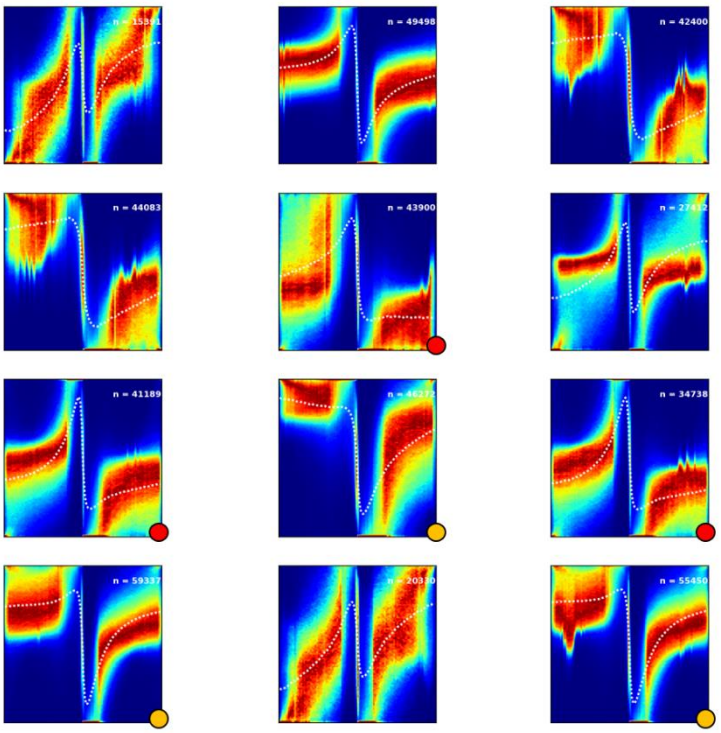

Figure 22: Results from clustering using lock-step and elastic distance measures. From left to right, the columns represent the results of clustering with locks-step measures, DTW (γ = 0.0) and soft-DTW (γ = 0.5).

Choice of distance measure

Usage of an elastic distance measure does not increase clustering capability and possibly even hampers adequate clustering ability. Furthermore, elastic distance measures are far more computationally intensive compared to the usage of lock-step measures. Hence, the lock-step measure is chosen as distance measure for further clustering purposes.

C. Dimensionality reduction

Segment size reduction

40 ms

Using a window size of 40 ms, usage of three clusters appears to be most suitable. Usage of four clusters could be considered as well, since this is shown to be preferential when analyzing longer segments. The values appear consistent with the curvature of the graph using the elbow method. The heatmaps using a three cluster-approach shows three morphological structures also present when analyzing 100 ms segments. Using a four-cluster approach, clusters have the same morphological structures as observed using the 100 ms analysis. Hence, clustering is deemed consistent when lowering the segments to a window size of 40 ms.

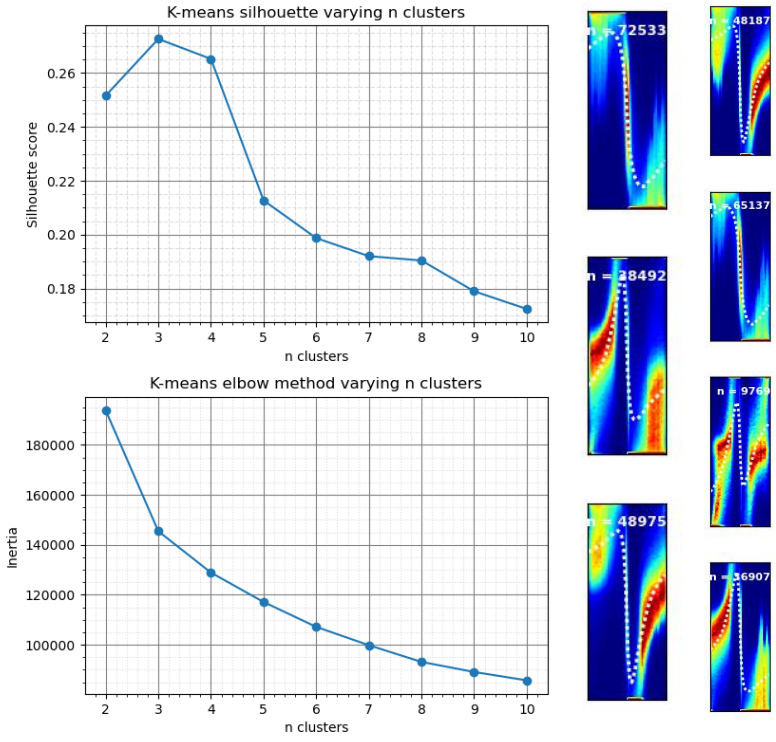

Figure 23: Overview of results with reduced segment size as input (40 ms). The left panel shows the evaluation scores (silhouette score and elbow method). The right panel shows the results of clustering using a three and a four-cluster approach.

70 ms

Using a window size of 70 ms, no preferential number of clusters could be identified using the evaluation scores. The elbow method does not give an indication of a possible suitable number of clusters as well. The heatmaps using a four-cluster approach shows clusters with varying morphology. The formed clusters appear comparable to the clusters formed using 100 ms segments. Although the same number of clusters is not observed as preferential in this shorter segment size, the results when adapting the same number of clusters is the same. Hence, altering the window size around the deflection, either reducing the duration after the potential or prior and after the potential results in consistent clustering results.

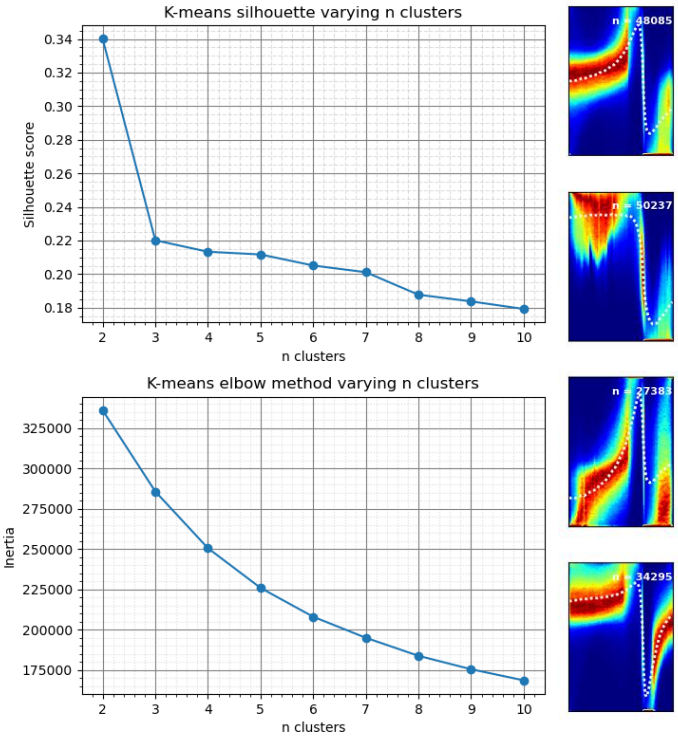

Figure 24: Overview of results with reduced segment size as input (70 ms). The left panel shows the evaluation scores (silhouette score and elbow method). The right panel shows the results using a four-cluster approach.

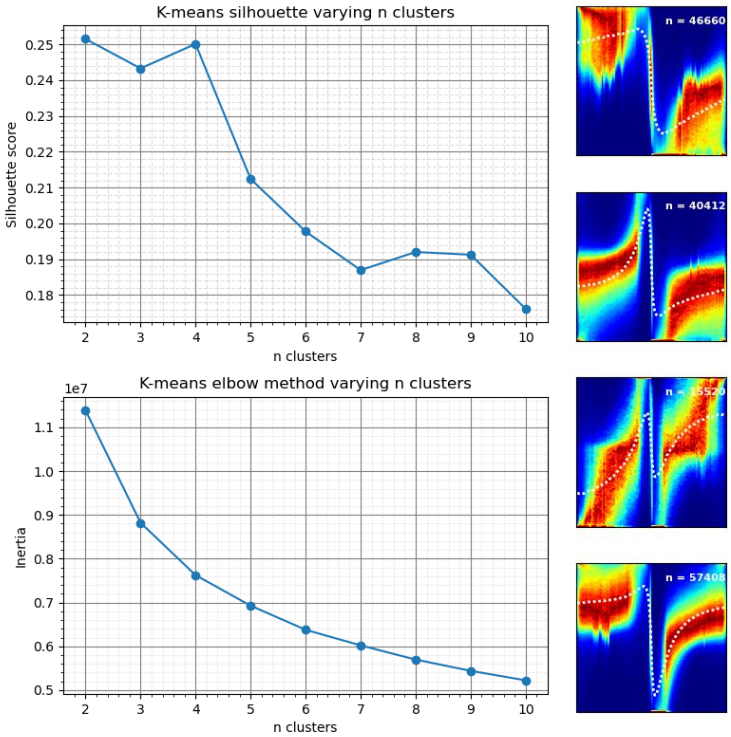

Figure 25: Overview of results with reduced dimensionality by PCA (using the first 8 principal components). The left panel shows the evaluation scores (silhouette score and elbow method). The right panel shows the results of clustering using a four-cluster approach.

PCA

A number of 8 principal components was consistently required to capture over 95% of the variance in the data. The principal components and their respective contribution to the explained variance are displayed in Figure 26, the principal components are not displayed on the same scale to enhance the morphology. The principal components do not show a potential morphology which can be explained by the current principles of electrophysiology, which was not also expected beforehand. The linear combination of principle components creates potentials with interpretable information. However, the newly defined axes can be used for clustering. When using the first 8 principal components for clustering of potentials, a number of four clusters is identified as the preferential number of clusters. The clustering results are shown in Figure 25. The created clusters are almost identical to the ones resulting from the using 100 ms time series data.

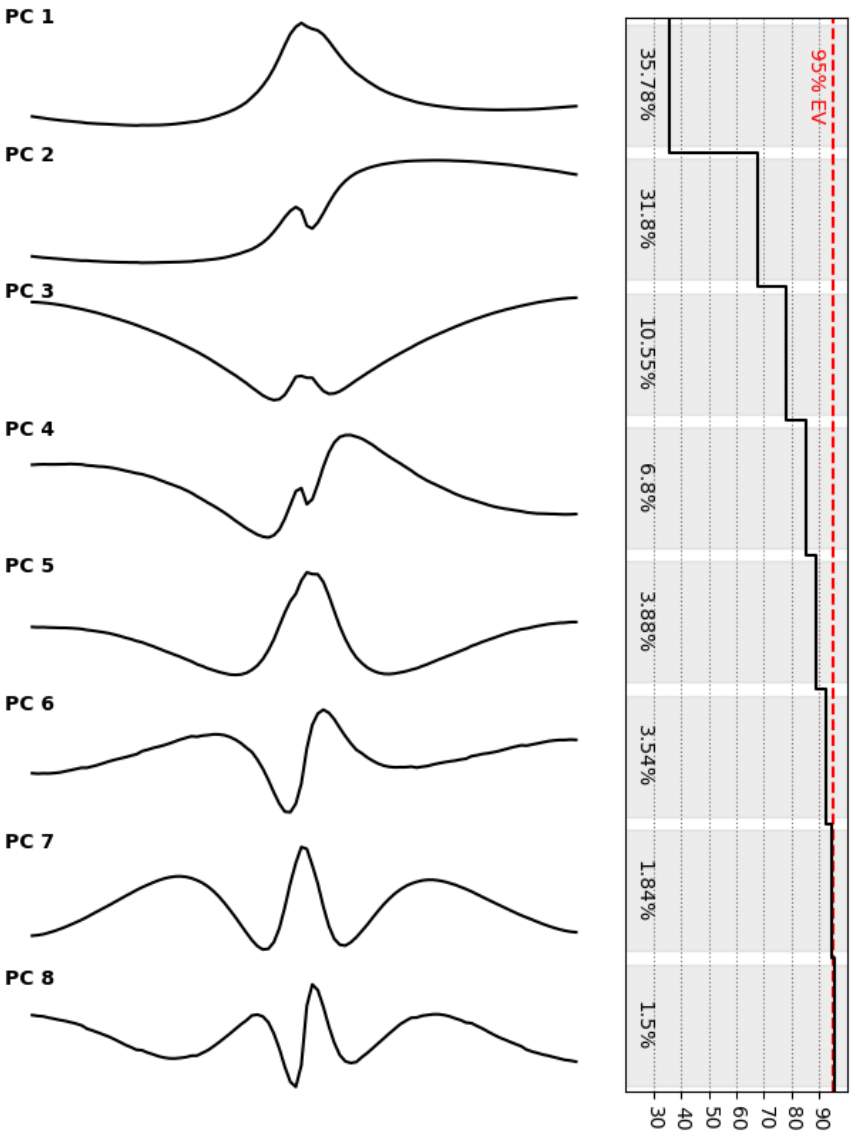

Figure 26: Principal components (eigenvectors of covariance matrix D in the 'Methods' section) with the respective explained variance (or eigenvalue of covariance matrix D in the 'Methods' section). The right panel shows the cumulative explained variance by the principal components. EV represents explained variance, PC represents principal component.

Currently used parameters

One of the files in the dataset had a value for the RS-ratio of 0 for all potentials. The data from this specific file was not included in clustering based on currently used parameters. The distributions of the clusters are displayed in Figure 27. In the unscaled data, the range of values was not equal across the different parameters. Robust range scaling reduced the range of parameter options. Finally, MinMax scaling ranged the values from equalized the possible ranges of all parameters (between 0 and 1). The amplitudes show a skewed pattern with decreasing frequency at higher values of the amplitude. Slopes display a shape similar to the amplitude spectrum, but with decreasing frequency at lower values of the slope. The RS-ratio shows a bimodal distribution. An increase in frequency of potentials showing an R-wave pattern is observed. S-wave patterns are even higher represented in the included data. A relatively low proportion of potentials showing a RS-pattern.

Using the unscaled data and data scaled using robust range scaling, no obvious preferential number of clusters can be identified from consensus between the silhouette score and the elbow method (see Figure 28). The only preferential number of clusters that might be considered, is 7. Using MinMax scaling, either a total of four or a total of six clusters can be considered based on the provided scores. The results are shown in the heatmaps of Figure 29. For comparison with k-means, heatmaps using four clusters are created with every scaling.

All methods adopting a number of clusters above four, irrespective of the performed scaling, resulted in similarity of potentials grouped in the same cluster. When a four-cluster approach is adopted, usage of unscaled data and usage of robust range matching resulted in no distinction in mean morphology across clusters. Discrepancy in ranges of possible values of different input parameters possibly results in domination of a single parameter. Usage of MinMax scaling resulted in more diversity in morphology across different clusters. However, overlapping morphology is still present. The diversity amongst clusters remains less satisfactory compared to the results of time series data clustering.

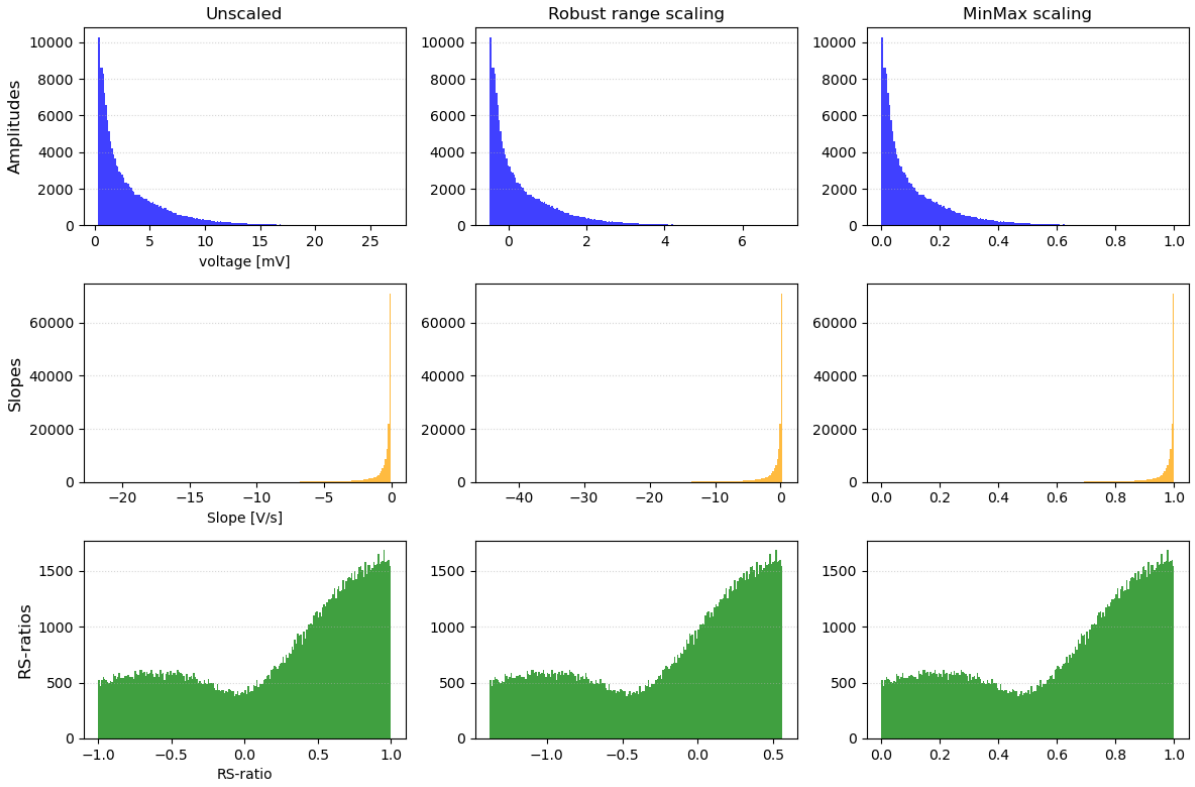

Figure 27: Parameter distribution of included potentials. From left to right: unscaled data, robust range scaling, MinMax scaling.

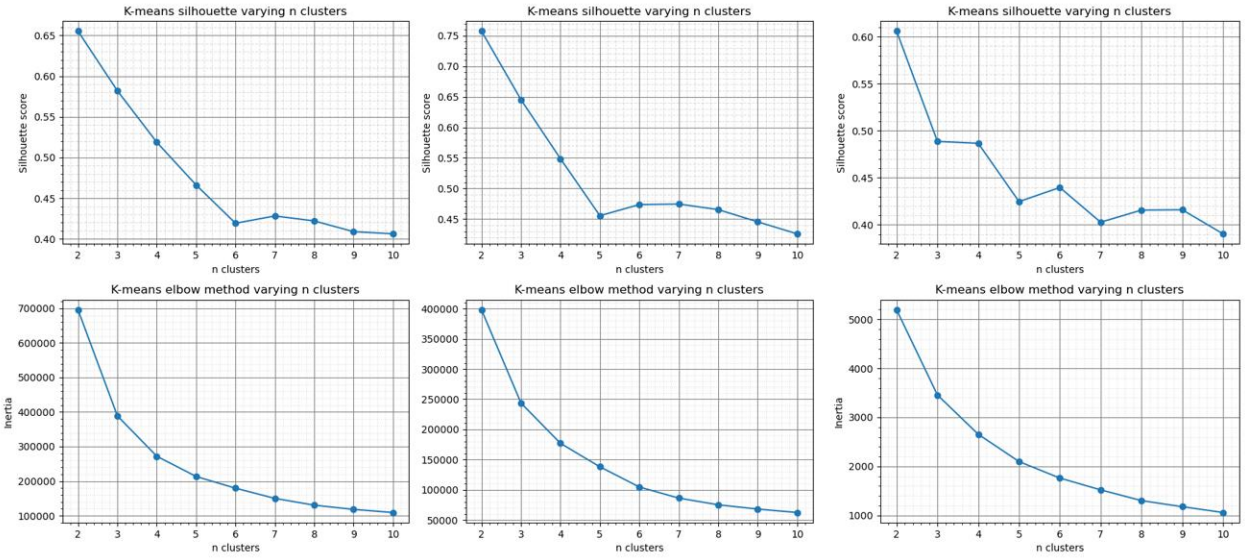

Figure 28: Overview of evaluation scores with different scaling for the currently used parameters. From left to right: unscaled data, robust range scaling, MinMax scaling.

Choice of dimensionality reduction

Reducing segment size results in consistent clustering. Hence a smaller segment size could be adopted. However, reducing segment size will still contain redundant information. Usage of PCA reduces the dimensionality even further and decreases the extent of redundant information compared to clusters formed using time series data (100 ms segments). Usage of the current parameters did not result in clustering results as observed using time series data. Although the goal was to prove that results of 100 ms electrogram clustering is not suffering from the curse of dimensionality, usage of PCA appears

to be an even more suitable option. Therefore, PCA using the first 8 principal components is adopted as dimensionality reduction in the clustering method.

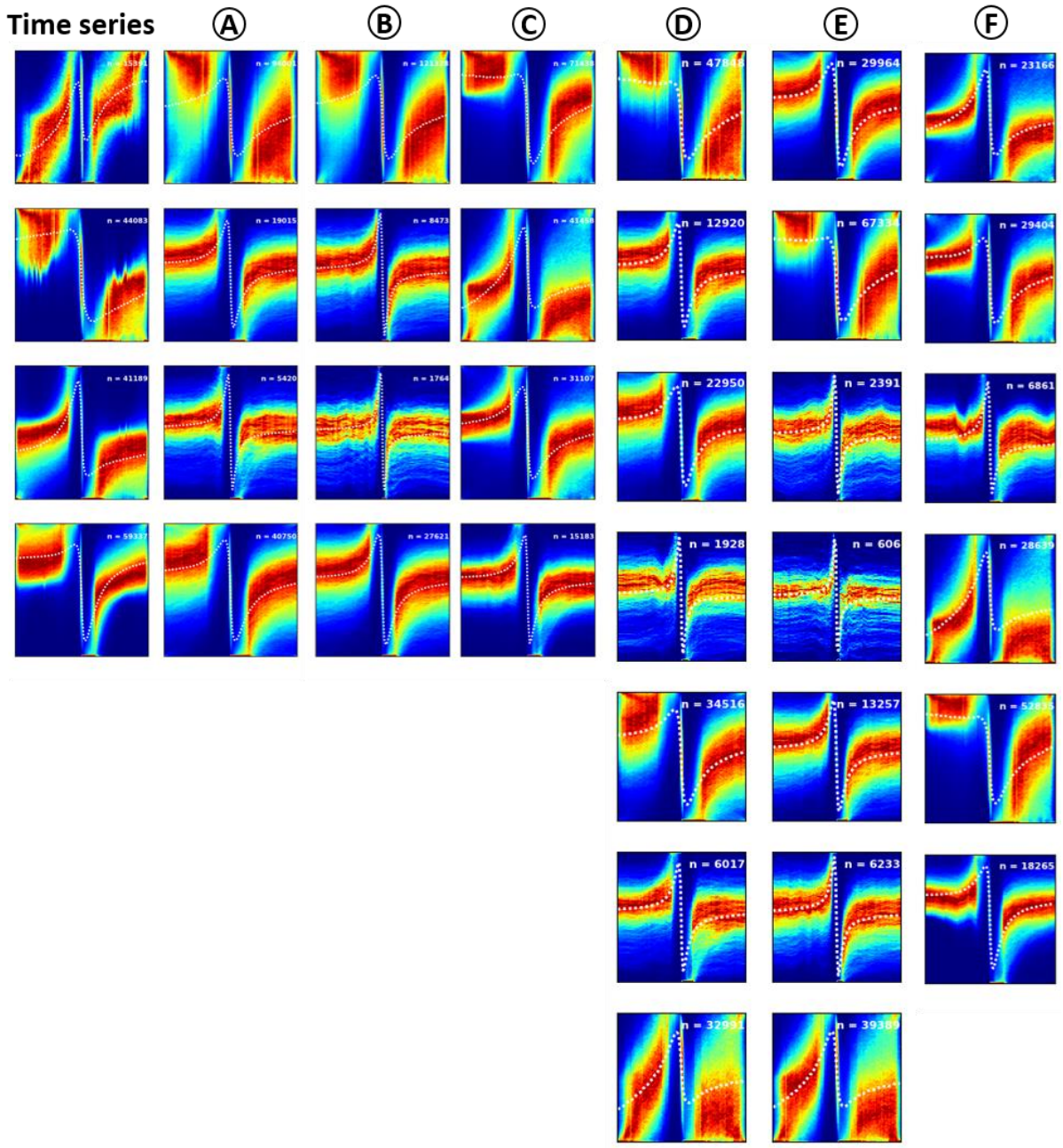

Figure 29: Overview using currently used parameters. Left: four cluster using k-means on time series data, A: four cluster with unscaled data, B: four cluster with robust range scaling, C: four cluster with MinMax scaling, D: seven clusters using unscaled data, E: seven clusters using robust range scaling and F: six clusters using MinMax scaling.

D. Cluster consistency

The results using all regions in equal proportions are already used in the prior sections. A total of 160000 potentials was used for the analysis. The number of potentials from other regions are displayed in Table 2. The clustering method performed from the previous section is utilized (k-means on using the first 8 principal components). Solely comparison between all regions, RA and LA are described.

Table 2: Included data to perform clustering based on different regional input.

	$N_{potentials}$	N_{files}	$N_{patients}$
All regions	*160000*	*128*	*23*
RA	*224055*	*63*	*16*
LA	*149819*	*32*	*18*

Right atrium

Using the proposed clustering method on all potentials retrieved from the RA, results are analogous to the results from combining all regions. The preferential number of clusters is determined at four. The results of the clustering are presented in the left panel of Figure 30. The general structures of the clusters are identical to the ones resulting from analysis of all regions.

Left atrium

Usage of potentials solely from LA results in local maximum of the silhouette score at a number of five cluster, contradictory to the clustering results of using all regions and solely the RA. Results of usage for five clusters is shown in the right panel of Figure 30. All clusters show a different morphology. The general structures from the clusters using a four-cluster approach with RA and a combination of all region data are also present amongst the clusters formed with the five-cluster approach from LA. An additional cluster is formed, shown in the top panel of the column of cluster figures.

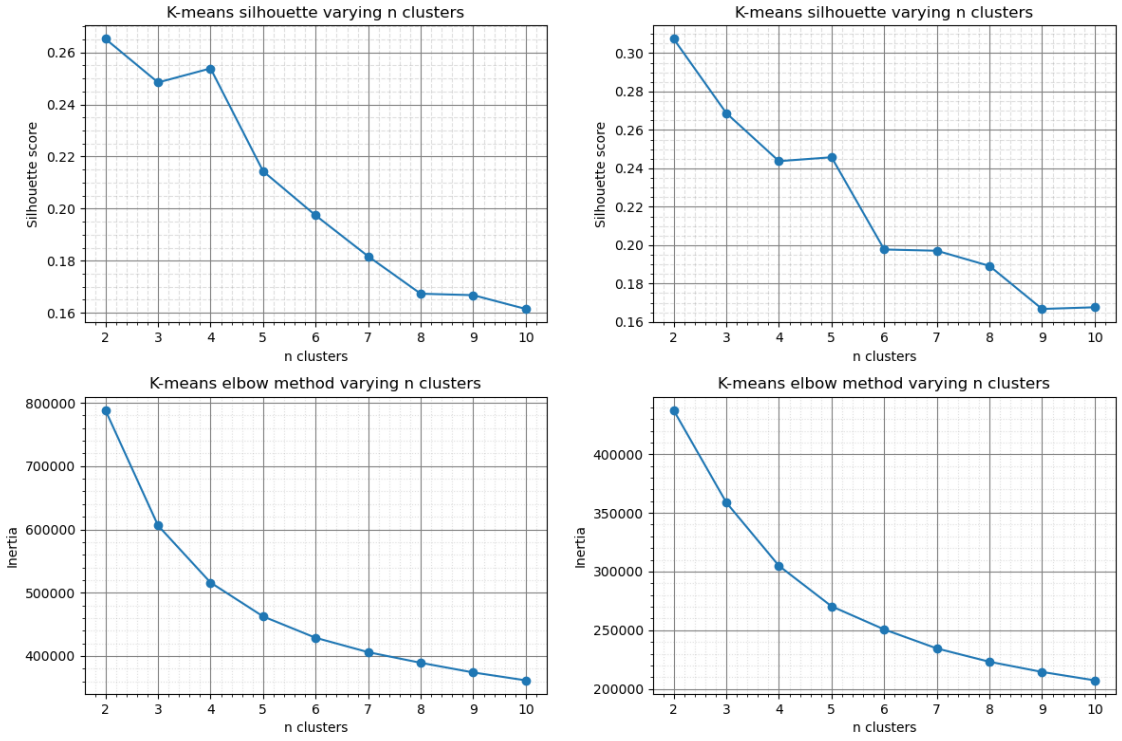

Figure 30: Silhouette scores and elbow method using k-means with input data only originating from the right atrium (left panel) and the left atrium (right panel).

Consensus between different input regions

Using different input data did not result in consistent number of cluster to choose. An overview of the heatmap results using a four and five-cluster approach is displayed in Figure 31. When four clusters instead of five clusters is adapted for input data originating from LA, the cluster without iso-electric segments is lacking. This cluster is present when adapting four clusters to RA data and data from all regions (indicated by the yellow circle at the right bottom of the cluster). The first cluster using LA data shows slightly increased density at the diagonal running from the left bottom corner to the right top

corner. This structure is corresponding with the separate cluster that is formed when using other input data.

When five clusters are formed with LA data, the increased density around the previously described diagonal disappears. Furthermore, the cluster without iso-electric segments appears (indicated by the red circle at the right bottom of the cluster). For input data from all regions and RA, a cluster with a morphology different from other clusters is formed. The newly formed cluster follows the morphology already present when using LA data as input with a four-cluster approach. The resulting general structures for the clusters for different input data are displayed in Figure 32.

One type of input data raises consideration of using a five-cluster morphology. Applying this strategy to the other types of input data, a new morphological structure is formed with increased consolidation of potentials around the general structure. Applying a five-cluster approach will therefore be most suitable. Further increasing the number of clusters does not result in creation of new morphological clusters. Usage of a five-cluster approach is therefore deemed optimal for clustering the SPs across the atrial epicardium. An overview of the results of clustering results using six clusters is displayed in Appendix I: Additional clustering results. The RA and the LA are the most prominent structures, hence these structures are explored as different input types. The same can be adopted to the remaining included regions: BB and the PV area. The results for these regions are displayed in Appendix I: Additional clustering results.

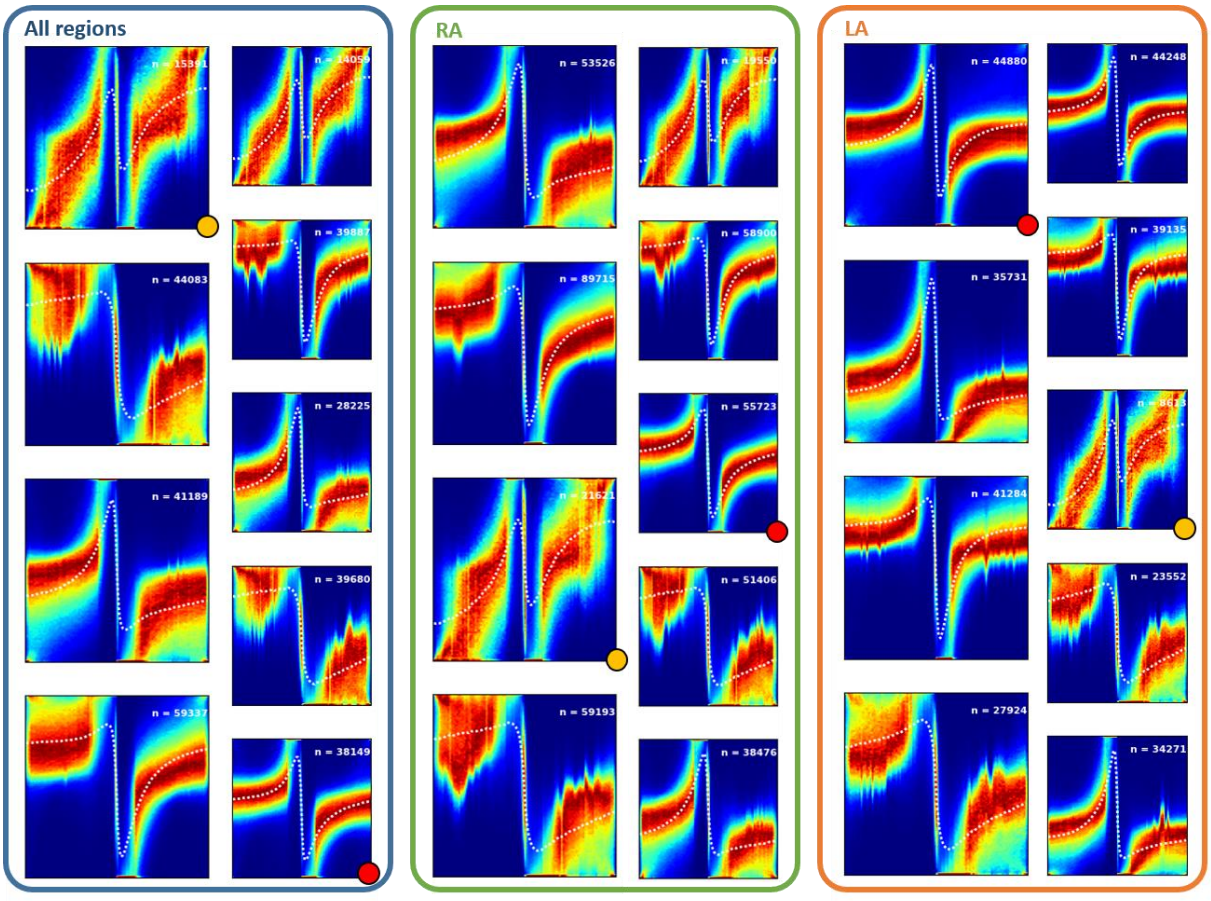

Figure 31: Results using a four and five-cluster approach for different regional inputs.

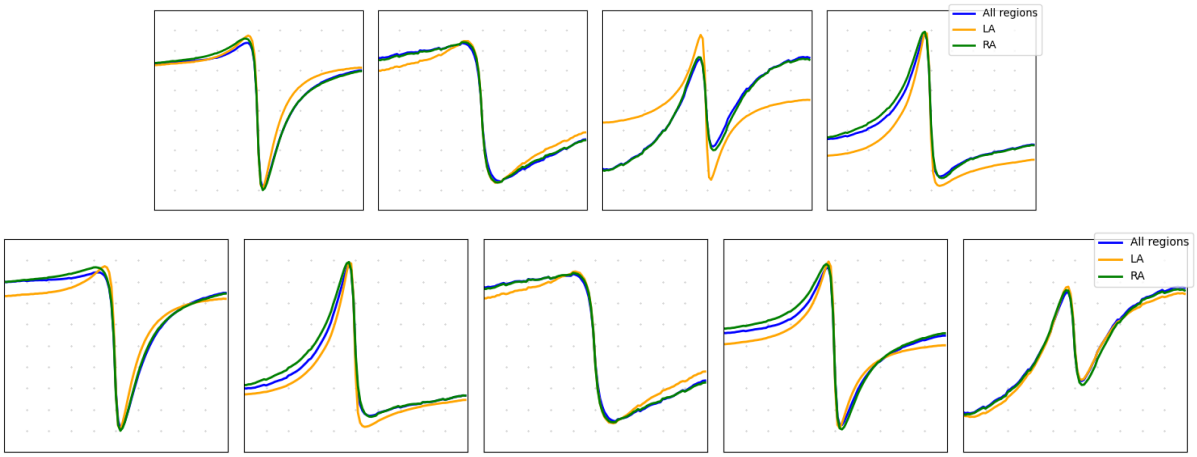

Figure 32: Overview using a four and five-cluster approach for different types of input data. A four-cluster approach shows no consensus in cluster structures. Applying a five-cluster approach shows consistent formation of clusters, irrespective of the input data.

E. Cluster covariance

For the acquired clusters, mean covariance between potentials are 0.58, 0.68, 0.66 and 0.82 and 0.73, respectively. When comparison between clusters is added, it can be observed that the covariances are effectively lower. An overview of the within cluster coefficients and the between cluster covariance is displayed in Table 3. The corresponding recurrence matrices within and between regions are shown in Figure 33. The range of the recurrence matrix is restricted between 0 and 1, since showing more detail in similar potentials is preferred. It can be observed that the first cluster is predominantly different from all other clusters. Although the covariances show similarity between some clusters (as seen between the second and the fifth cluster), it is significantly lower than the mean covariances reached within the clusters. The average within cluster covariance is 0.69. The between cluster covariance in the samples was 0.30. When looking for individual clusters, the covariances are relatively higher within clusters compared to comparison with other clusters (within-to-between cluster covariance ratio ranging from 31.96% to 105.31%).

The results confirm the presence of a pattern within the identified clusters. Potentials which are clustered together appear to be more similar compared to potentials from different clusters.

Table 3: Overview of within and between cluster covariance.

Cluster	1	2	3	4	5
1	***0.58***	*0.10*	*0.09*	*-0.33*	*0.01*
2	*0.10*	***0.68***	*0.56*	*0.55*	*0.63*
3	*0.09*	*0.56*	***0.66***	*0.50*	*0.37*
4	*-0.33*	*0.55*	*0.50*	***0.82***	*0.56*
5	*0.01*	*0.63*	*0.37*	*0.56*	***0.73***
Within-between ratio (%)	*105.31*	*31.96*	*42.12*	*61.21*	*45.92*

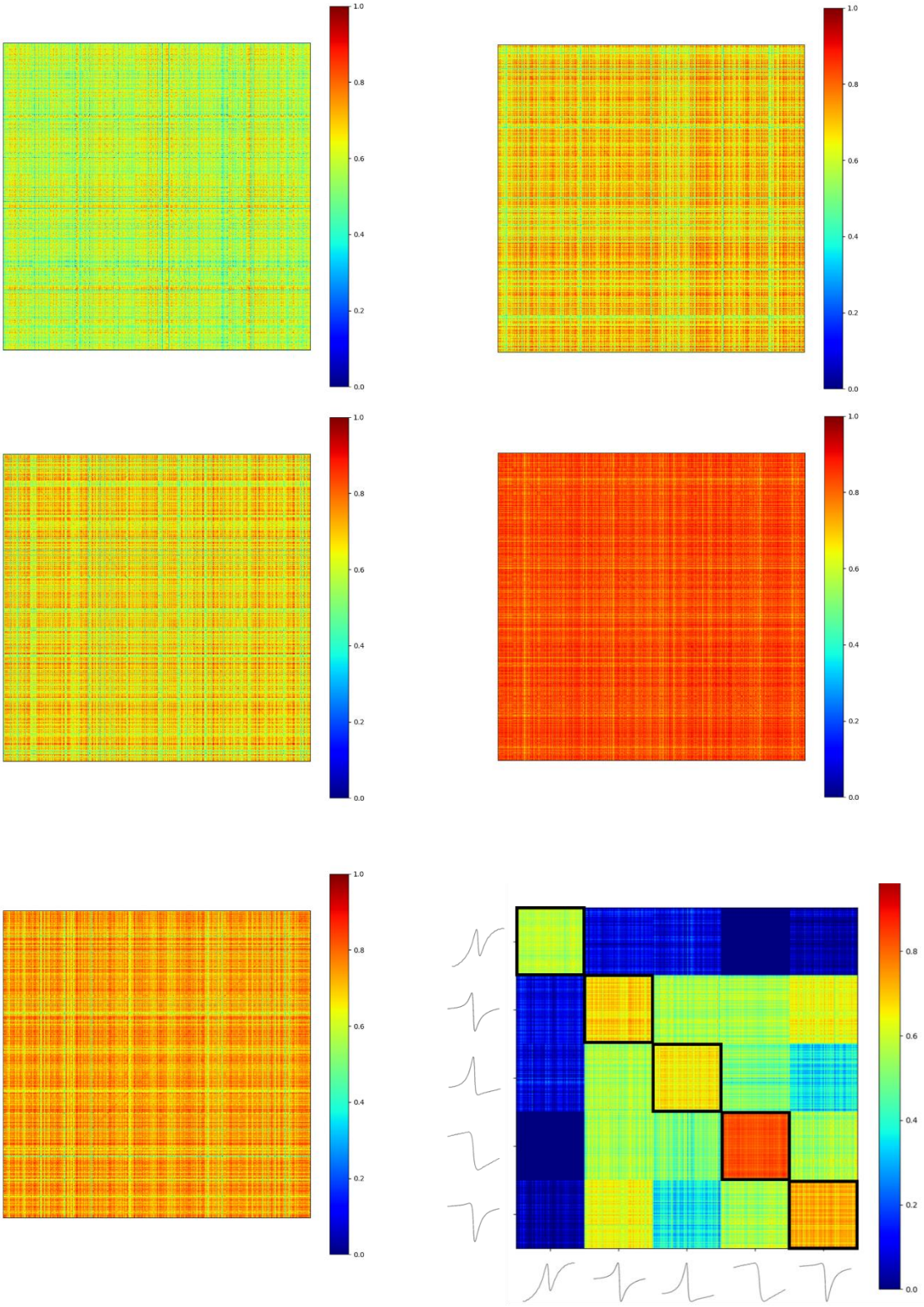

Figure 33: Covariance within and between clustered potentials, displayed by a recurrence matrix. Negative values of the recurrence matrix are clipped at a value of 0. The top panel shows the covariance of potentials within the same cluster for the first and second cluster. The middle panel does the same for the third and fourth cluster. The left site lower panel shows the covariance of potentials within the same cluster for the fifth cluster. The right site shows the overview of the covariances within a cluster but also between different clusters.

II. Single potentials – spatial cluster occurrence (II)

For all subgroups in both the regional and the cluster analysis, normal distribution could not be assumed. Analysis was performed using non-parametric tests. An overview of the occurrence of the different clusters across different regions is given in Table 4. Values are displayed as median with IQR. Hereafter, the clusters will be referred to with the names appointed in Figure 34.

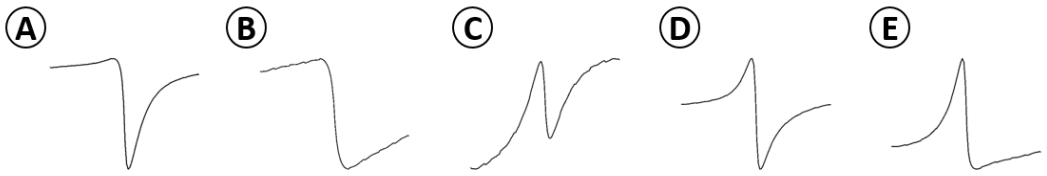

Figure 34: General structures of clusters with new indications.

Table 4: Overview of mean occurrence percentage across different regions and clusters. Values are displayed as median and interquartile range.

	RA (n_{files} = 62)	LA (n_{files} = 32)	PV (n_{files} = 19)	BB (n_{files} = 16)	RS-ratio	Amplitude	Slope
Cluster A	28.36 [16.15|40.44]	21.67 [11.78|28.85]	21.64 [11.78|28.85]	17.26 [11.91|29.28]	0.73 [0.58|0.86]	3.30 [1.69|5.30]	-0.35 [-0.77|-0.16]
Cluster B	24.81 [14.78|34.35]	9.77 [5.31|17.52]	30.73 [17.45|40.45]	41.26 [37.26|45.10]	0.64 [0.35|0.83]	1.48 [0.85|2.52]	-0.11 [-0.20|- 0.07]
Cluster C	7.24 [3.67|12.86]	4.54 [1.60|8.32]	10.12 [3.60|15.39]	9.84 [3.79|14.41]	-0.51 [-0.74|-0.23]	0.67 [0.45|1.01]	-0.09 [-0.14|- 0.07]
Cluster D	22.71 [16.71|28.58]	32.87 [24.11|39.57]	17.31 [15.10|24.16]	14.18 [12.39|16.86]	0.22 [-0.07|0.43]	4.23 [1.91|7.10]	-0.64 [-1.52|- 0.23]
Cluster E	13.86 [7.42|20.25]	24.26 [12.73|32.99]	9.53 [4.33|16.34]	15.97 [12.84|18.57]	-0.57 [-0.77|-0.33]	2.48 [1.18|5.11]	-0.30 [-0.90|- 0.12]

A. Cluster occurrence

Cluster occurrence from a regional perspective

An overview of the distribution of the relative occurrences for the four predefined regions is shown in Figure 35.

Cluster A, B and D had significantly higher occurrence across the RA compared to cluster C and E ($p < 0.001$). Furthermore, cluster E was significantly higher represented across the RA compared to cluster C ($p < 0.05$). The overall pattern shows mainly potentials with a S-wave morphology. Potentials showing an R-wave morphology are less commonly encountered. At LA, cluster C was significantly lower represented compared to cluster A, D and E ($p < 0.001$). Cluster E and D were also relatively more common across LA compared to cluster B ($p < 0.05$ and $p < 0.001$, respectively). S-wave morphology is more dominant across RA, LA shows more R to RS-wave morphology. The PV region shows a similar distribution to RA with a S-morphology occurring in a high proportion of the potentials. Cluster A and B show significantly more observed compared to cluster C and E ($p < 0.01$ for cluster A comparison and $p < 0.001$ for cluster B comparison). In BB, manifestation of B is pronounced above the other defined clusters ($p < 0.05$, $p < 0.01$, $p < 0.001$ and $p < 0.001$ for cluster A , E, C and D, respectively). No other clusters appear to have heightened occurrence in this region.

Regional occurrence from a cluster perspective

An overview of the distribution of the relative occurrences for the four predefined regions is shown in Figure 36.

Not all clusters show a preferential occurrence site. Cluster A occurs equally across the defined regions. However, Cluster B shows distinct preferential regional occurrence. The cluster is least represented across LA compared to the three other regions ($p < 0.01$, $p < 0.01$ and $p < 0.001$ compared with RA, PV and BB, respectively). Furthermore, BB area appears as preferential site with increased occurrence compared to RA ($p < 0.01$). Cluster C shows, likewise cluster A, no preferential site of manifestation. Manifestation of cluster D is increased in the LA region. The percentage of potentials falling in this cluster at LA is significantly higher compared to RA ($p < 0.01$), PV area ($p < 0.01$) and BB ($p < 0.001$). This high occurrence rate might be explanatory for a preferential number of five clusters based on the silhouette scores in the cluster generation. Furthermore, cluster D is significantly higher represented across RA compared to BB ($p < 0.001$). Cluster E is increased in LA compared to RA and the PV area ($p < 0.01$ and $p < 0.001$, respectively).

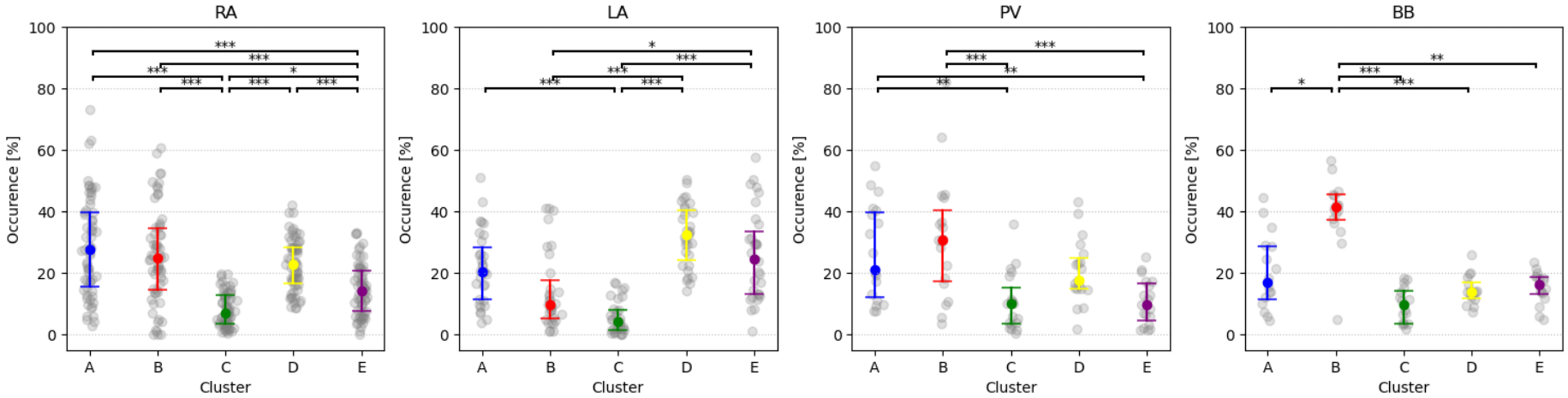

*Figure 35: Regional analysis of cluster occurrence. Significant differences are displayed at the top of the figure (* = p < 0.05, ** = p < 0.01, *** p < 0.001).*

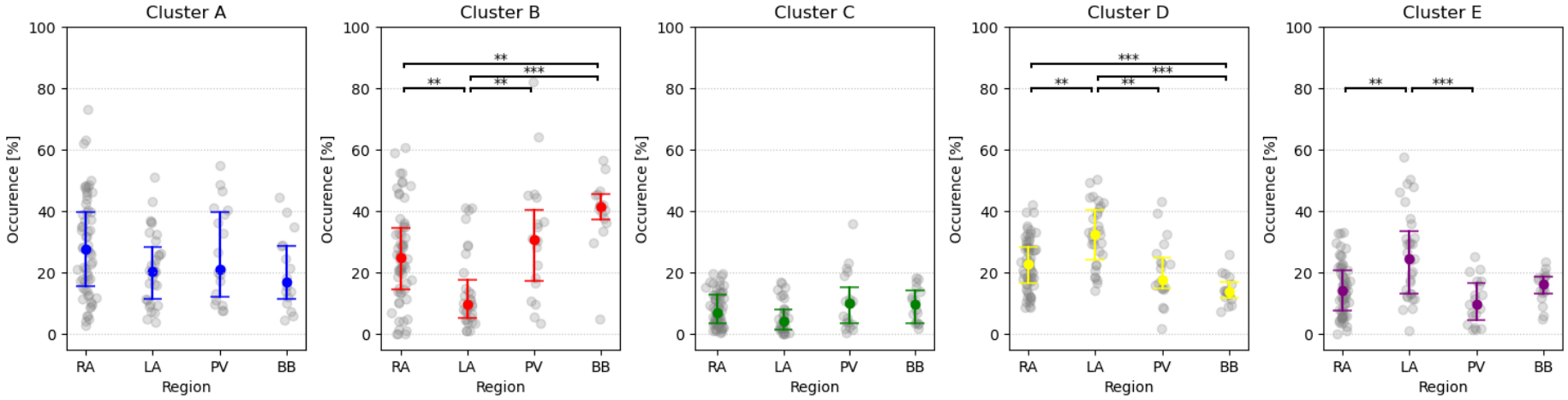

*Figure 36: Cluster analysis with occurrence across the different regions. Significant differences are displayed at the top of the figure (* = p < 0.05, ** = p < 0.01, *** p < 0.001).*

B. Cluster characteristics

The violin plots of the currently used parameters per cluster are shown in the Figure 37. The presence of outliers can cause the difficulty in analyzing the underlying distributions. Hence, the y-axis for the violin plots of the amplitude and slope parameter have been clipped based on visual inspection. The high number of data caused significant differences between all clusters for all the described parameters. However, not all differences should be regarded as clinically relevant.

Cluster C did not show a known distinct morphology. The potential itself did not represent the maximum and minimum of the electrogram range when normalized. The values of for the currently used parameters could therefore be inaccurate using the current software and cannot be compared to the values of the other clusters.

Cluster A and B show an S-pattern, as expected. Cluster D shows a distribution more focused across the spectrum of an Rs to an rS pattern. Cluster R shows increased density at potentials with an R-wave pattern. Cluster A , D and E show relatively higher amplitudes compared to cluster B. Especially cluster D shows increased amplitude. The results for the amplitude are unanimous with the observed patterns across the slopes of the potentials in the clusters. Cluster B shows a flattened slope compared to cluster A, D and E. Of all clusters, cluster D shows potentials with the steepest slopes.

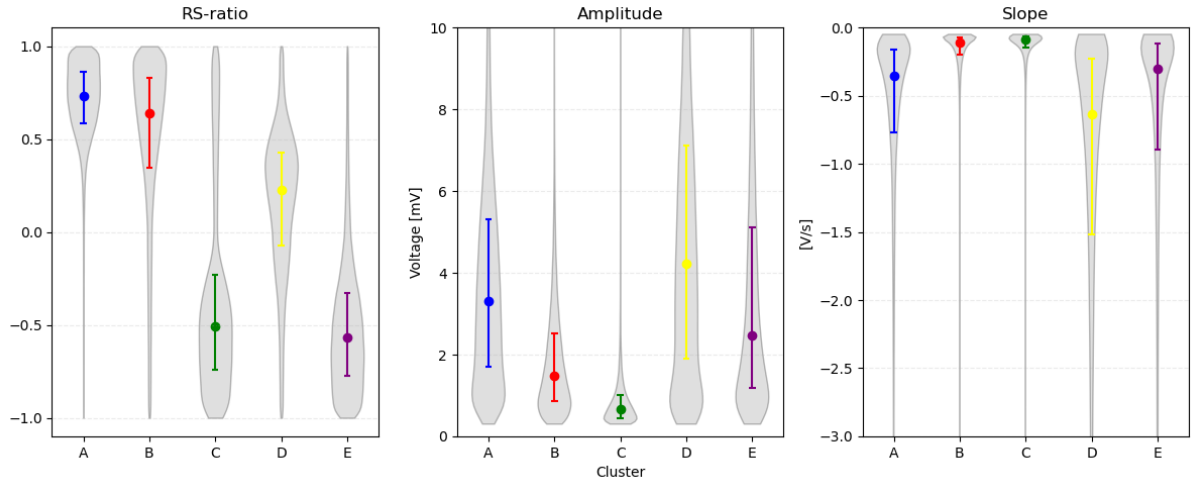

Figure 37: Violin plots of distributions of the currently used parameters per cluster. The color coding of the clusters corresponds to the scatterplot figure across different clusters as shown before. The colored marks represent median values with interquartile ranges.

DISCUSSION & CONCLUSION

4

Discussion

I. Cluster formation

A. Algorithm consideration

Clusters were formed using the k-means algorithm. DBSCAN did not appear to be an adequate clustering algorithm for the current data. Explanatory could be the normalization of the potentials. Normalization causes mapping (most of) the potential to the same range around the deflection, with a value of 1 around the R-peak and a value of 0 around the S-peak. DBSCAN is a density based clustering algorithm. The value of all potentials in the dimensions across this features (time instances) are similar, reducing the variance in the high dimensional space. This causes clusters density to be increased along these dimensions. The unequal density could hamper the efficacy of the clustering algorithm using the current parameters for the DBSCAN algorithm. Notable is that potentials falling in the noise show a heatmap that, if compared to using k-means, shows a pattern most resembling the cluster without iso-electric segment (or cluster C). Amongst these potentials in the noise, the deflection in the potential might not yield the total range of the potential after normalization. The general structure of the noise becomes more similar to cluster C with increasing value of epsilon. The finding supports the probability of hampered clustering ability due to normalization of potentials. Regarding GMM, only the usage of GMM with a spherical covariance restriction reaches a performance close to the usage of the k-means algorithm. This structure is most similar to the k-means algorithm in terms of decision boundaries. Other covariance restrictions reduced clustering ability. The findings underlines the choice for the usage of k-means as the most appropriate clustering algorithm for the current problem amongst the included algorithms.

B. Evaluation metrics

Using k-means, the number of clusters is defined based on the silhouette score and the elbow method. A silhouette score of 0 is achieved when the eventual clusters are indifferent. The closer the silhouette score is to 1, the better the clusters are separated. The observed silhouette scores might therefore not be satisfactorily high. This could be due to the usage of high dimensional data. Increasing dimensions or features will increase the variety in the dataset. When the dimensions are reduced, distinctly higher silhouette scores are reported. This is notable when performing clustering based on the parameters of the ‘currently used parameters’ section. Although the reported scores are significantly higher, this did not result in satisfactory clustering results upon visualization. The currently used dimensionality reduction (using the first 8 principal components) does report similar silhouette scores. As mentioned, PCA defines new axis in the feature space to reduce dimensionality whilst retaining variance. Hence, the silhouette scores are not expected to be substantially increased.

C. Cluster evaluation

Each of the five eventual clusters displayed a different structure. Four of the clusters showed an evident morphology (cluster A, B, D and E). One cluster shows an obvious R-wave pattern (cluster E). Potentials falling in this cluster could be located at sites of wave termination. One cluster shows a distinct RS-pattern (cluster D). Two clusters show a predominant S-pattern (cluster A and cluster B). The main difference between the two clusters appears to be in the duration of the potential. Unlike cluster B, cluster A shows an S-wave, followed by a quick return to the iso-electric segment. Conspicuous is the cluster showing no iso-electric segments (cluster C). It is expected that the deflection is the component of the electrogram with either the highest or lowest voltages. This does not seem to be the case in this cluster. The cluster might contain potentials showing a morphology not to be explained by the electrophysiological characteristics of the cardiac tissue. Segments with ventricular activity overlap are excluded. Contribution of ventricular activity is therefore ruled out.

Baseline drift of the electrode during measurement might contribute to the observed morphological structure. Cluster C appears to be represented to a lesser extent compared to other clusters. Furthermore, the covariance of the potentials in this cluster compared to potentials from other clusters was consistently low (see Figure 33), establishing the distinct different morphology compared to other clusters.

II. Epicardial cluster occurrence

During SR, the wave front is initiated in superiorly in the RA. The expected pattern across RA would be an S to an RS pattern across the right atrium. BB is located in proximity to the SAN between the RA appendage and the superior vena cava (84), connecting RA and LA. Hence a predominant S-wave pattern is expected as well. The wavefronts are expected to be terminated primarily in LA or the PV area. These regions would be categorized by relatively more R-wave morphology compared to BB and the RA region. Van Schie et al. (21) and Ye et al. (20) confirmed these patterns of RS-ratio distribution across the atrial tissue during SR.

During AF, the morphological pattern across the atrial surface is expected to change. Focal activation from the PV are significantly contributing in the initialization of AF (85). Although initial focusses can be concentrated to specific regions, sustaining AF causes decline of the atrial tissue conductivity. Hence, differences in driver distribution are observed across the atrial surface in more advanced stages of AF (86-88). When regarding the cluster through the perspective of RS-ratios, the PV region does show increased S-wave morphology. However, the LA tissue shows no distinct differential pattern when compared to RS-ratio histograms during SR (20, 21). The S-wave morphology was expected to be more prominent in this region. Not only is an R-wave and RS-wave morphology more present compared to the other clusters, the morphologies are also most prominently expressed in this region compared to the other region. The same goes for the RA region. A S-wave and RS-wave morphology is still the most encountered morphological structure. BB still showed prominent S-wave morphology. Hence, the observed pattern does therefore not fully match the on beforehand expected pattern.

Although both cluster A and B show a S-wave morphology, both waves are different from a electrophysiological perspective. The heatmaps raised suspicion on increase of the potential duration compared to cluster A, D and E. Potentials in cluster B showed a distinct flattened slope, compared to the other clusters. The reduction is accompanied by a reduction in amplitude. An S-wave pattern with increased duration and reduced amplitude could be fitting the characteristics of focal activity. Cluster B appears heightened in BB, the PV area and RA. Focal activity from RA could partially contain SAN activity. Focal activity from the PV area is, as described, a known site of focal impulses during AF (85). However, BB shows a surprisingly high occurrence of cluster B. From a regional perspective, the occurrence of cluster B compared to the other clusters is far more prominent in BB compared to other regions. BB is a myocardial structure with parallel fiber orientation. Animal models showed increased conduction velocity along the fiber direction compared to other atrial structures (89-92). However, BB has also shown anisotropic behavior (89, 93). Given the high proportion of AAF patients, the conductive properties of the bundle are expected to be intact and potentials conducting along the longitudinal axis are not expected to be elongated. The observed increase in slowly conducting S-wave morphology in BB could therefore be the result of innervation from other sites rather than the longitudinal axis of the fibers during AF. The absence of a clear R-wave suggest initiation in close proximity to the bundle itself. The structures capable of innervation near BB could come from the roof of either atrium. However, a major proportion foci would be expected to still cause innervation proximally along the longitudinal fiber axis. Another myocardial structure near BB capable of innervation from a transversal site to the fiber orientation is the intra-atrial septum. This structure cannot be evaluated from an epicardial perspective. Yet, studies using a endocardial approach have appointed the septum to

contain substantial arrhtyhmogenic substrate (86, 87, 94). With septal innervation however, the wave front would approaching BB would be expected to show an R-wave component. The general structure of the cluster is lacking this morphology.

A single origin causing the observed pattern at BB is difficult to appoint. However, when analyzing density boundaries along the heatmaps of cluster A, B, D and E, cluster B also shows the least condensation around the general structure. Multiple sources possibly contribute to pattern observed at BB, including LA and RA roofs and the intra-atrial septum.

III. Limitations

A. Choice of clustering setup

K-means was determined to be the most suitable algorithm for the current problem. However, when inspecting the heatmaps from the respective clusters, it can be thought that potentials will be on the border in between two clusters. As mentioned, k-means is an algorithm performing hard clustering. Detailed deviations in potentials on the border of two clusters can cause very similar potentials to fall into different clusters. The concept is elaborated in Appendix II: Soft clustering .

The usage of soft clustering provides opportunity to use a constraint on the posterior probability for a potential to be assigned to a cluster. A certain degree of certainty can be applied to the probability for a potential to be assigned to a cluster. This way, the clusters will be better defined when compared to the currently used method. The main downside will be the inability to cluster a proportion of the potentials. One soft clustering algorithm already encountered is GMM. The usage of spherical covariance approaches the performance of the usage of k-means clustering. However, as mentioned before, the borders of the heatmaps using the GMM algorithm show more discontinuity compared to using k-means. Fuzzy c-means is the soft clustering equivalent of k-means (95, 96). Exploration of this algorithm might increase the distinction between clusters. The higher the constraint of a potential to have a certainty to belong to an individual cluster, the better the cluster boundaries are expected to be defined. Furthermore, it might be more applicable for characterizing potentials containing a greater proportion of noise in the signal.

B. Atrial fibrillation subtypes

No distinction is made between the different subtypes of AF. Data from different AF subtypes were included, however AAF was the predominant type of AF across the included patients (56.52%). As mentioned, the atrial tissue remodels overtime during AF (16). Different studies already investigated epicardial tissue properties between different subtypes of AF. Comparing LSPAF with AAF, LSPAF showed an increased number of simultaneous wave fronts activating the tissue, accompanied by higher proportion of conduction block (23, 24). Furthermore, de Groot et al. (97) showed increased amount of breakthrough waves at the epicardial surface LSPAF compared to AAF. A wave originating from the endocardium layer was characterized by a small R-wave followed by a relatively superior S-wave, focally originating at the epicardial surface. These findings affirm the possibility of observing morphological changes at the epicardial surface for different subtypes of AF. The unequal contribution of different types of AF across the data might limit the generalizability of the results.

C. Single potentials

The sole usage of SPs is a limitation of the current study. Although SPs are expected to be a considerable proportion of the data, potentials containing multiple deflections are not analyzed in this thesis. FPs might occur at sites of most abnormal conduction. Sole usage of SPs might show a distorted pattern of the actual tissue characteristics. In line with the previous limitation, further progressed stages of AF show a higher proportion of FPs along the epicardial surface during rapid pacing when

mapped in animal subjects overtime (98, 99). The proportion of SPs can become even less representative of the tissue characteristics in further advanced stages of AF. The substantial proportion of AAF patients might enhance adequate representation of the cardiac tissue when solely using SPs.

IV. Clinical implications

Using the currently identified clusters, SPs can be used to evaluate potential morphology at an individual level. The degradation of conductive properties of the atrial tissue are not sufficiently classified using the current categorization. AF subtype is determined based on the first recorded episode. However, detection of the first episode can be highly variable across different patients. Especially in patients with asymptomatic AF, the first recorded episode is discovered incidentally. Remodeling of the atrial tissue could already be present for a substantial period. Asymptomatic atrial fibrillation is reported in 15-30% of the patients (100). Hence, the current classification scheme is not optimal in determining the tissue damage severity across patients. Usage of the individualized potential morphology could aid in describing the individual tissue characteristics and mediate in estimation of progression state of AF.

Lastly, the methodology of this study could have implications in future electrophysiological procedures. Electrophysiological ablational strategies for AF are primarily focused on the modulation of the LA arrhyrhmogenic substrate (101). Standardized ablational strategies are effective in early stages of AF (102). However, equivalent strategies are not sufficient in terminating further sustained types of AF, with lacking standardized additional treatment options (103, 104). Patient eligible for treatment should be selected based on progression state of the atrial tissue and spatial distribution of potential drivers. The current findings indicate possible contribution of a broader proportion of atrial tissue than the LA alone. Individual assessment of tissue characteristics can be contributing to select patients suitable for treatment. The current methodology is adapted to data from an epicardial perspective. Although presently not yet performed in clinical practice, possible advancement of technology might introduce the possibility of high-resolution endocardial mapping. Translation to endocardial mapping could introduce patient treatment election at acceptable invasiveness.

V. Future perspectives

The future perspectives of this thesis are widespread. The research can be regarded as the basis for a future research options. Future directions are aimed to further describe the characteristics of atrial tissue at an individual level.

A. Atrial fibrillation subtype analysis

The majority of the database covered patients with AAF (56.52% of the patients and 62.50% of the files). The other subtypes of AF were relatively low represented: PAF (17.39% of the patients with 20.31% of the files), PeAF (8.70% of the patients with 1.55% of the files), LSPAF (17.39% of the patients with 15.63% of the files) and PerAF (0% of the patient with 0% of the files). Furthermore, files included from patients with PeAF were only originating from the LA. The shortage of available data from the individual subtypes of AF complicates the possibility of comparison. However, as discussed prior, different morphological structures could be expected between different AF subtypes. Data from all included regions was available from patients with PAF and LSPAF. The adaption of the clusters to these subtypes are supplied in Appendix III: Atrial fibrillation subtype , however no statistical analysis was performed. Once a more extensive spreads of data of different AF subtypes becomes available, the current methodology could be adapted to perform analysis of the different subtypes. The observations from subtypes analysis could be a foundation for estimation of progression state based on the observed epicardial morphologic patterns.

B. Description of fractionated potentials

Application of current methodology

Following the limitation on the sole usage of SPs, description of potentials with multiple deflections could be valuable to further characterize the atrial tissue. Clustering potentials with multiple deflections will be complicated using the current methods. Using SPs, the morphological structures can be compared by normalization of the potentials and alignment around the deflection. When additional deflections are added, the spectrum of options drastically increases. The different timing between the deflections will hamper the comparative the ability between two potentials given the deflections will not be aligned. Although not applicable in SP clustering, usage of elastic distance measure like DTW could mediate in improving alignment for clustering ability in spare cases. When the secondary deflections of the potential are located on the same site of the primary deflection, the alignment might be improved. If not, the monotonicity condition (see 'Distance measures' section) will hamper alignment to the corresponding component of the to be compared potential.

Furthermore, normalization causes the potential to be mapped to the range of the deflection in most cases. The contribution of the amplitude in the cluster determination therefore becomes negligible. The introduction of multiple deflections will cause the relative amplitude of the two potentials to become a factor in the clustering process.

Visualizing the created clusters is a vital concept in unsupervised learning. Although the evaluation metrics are suitable to find an adequate number of clusters, the clusters itself should be carefully inspected to ensure adequate performance. The high-dimensionality hampers usual scatterplot techniques to visualize the clusters. The usage of SPs allows the creation of heatmaps to visualize the created clusters. With the addition of multiple deflections, general structures of potentials cannot be visualized using the proposed heatmaps.

Fractionated potential categorization

For the purpose of clustering FPs, other options than using the time-domain could be considered. Evaluation of individual potentials interferes with the usage common techniques in the frequency-domain. The spectral resolution is related to the length of the analyzed signal and the used sample frequency. Decreasing the segment length reduces the spectral resolution. Usage of 100 ms segments with a sample frequency of 1 kHz will result in an analysis of spectral components in steps of 10 Hz. The usage of wavelets creates different levels of temporal and spatial resolution. It should be investigated whether the spectral resolution hampers the analysis of the spectral content of the signal. However, if analysis of the spectral features is feasible, visualization of adequate clustering performance will still be problematic.

Another consideration would be using the currently described results. A SP is the result of a propagating wave causing simultaneous activation of the cardiac tissue underneath the unipolar electrode. A FP is the result of the asynchronous activation of isolated groups of myocardial tissue, containing a component of temporal separation, spatial separation or both (105). The eventual potential should be the result of superimposing the resulting potential of multiple groups of myocardial tissue, each creating their SP. The results from clustering the SPs could therefore be used to model FPs.

The general structures from the cluster analysis in SPs can be regarded as the basis functions to build the FPs. The influence of temporal and spatial variation should be taken into account for the basis functions. Temporal variation would cause the deflections to be shifted in time at the site of the FP. Scaling and shifting along the temporary axis of the basis functions should therefore be allowed. The amplitude of the recorded potential is a tradeoff between group size and distance to the electrode.

The greater the myocardial group size, the larger the amplitude. The amplitude decreases with distance from the source (106). Therefore, scaling the amplitude of the basic functions covers the influence of group size and spatial variation. The occurring FP should be described by the relative contribution of different basis functions and their respective timing, scaling in time and scaling in amplitude.

A method similar to the proposed strategy is performed by Houben et al. (107) to define FPs. The FPs were set up by a variations of time-shifted and amplitude-scaled combinations of mathematically defined SPs. However, the method was utilized for detection from atrial electrograms with the ultimate goal of real-time unipolar mapping rather than morphological analysis. The description of the individual basis function contribution might help to characterize the genesis of FPs. A potential method for evaluation is the usage of matching pursuit (108). Matching pursuit approximates the observed signal (FP) by a weighted combination of elements from a predefined library. Individual components of the library are appointed a coefficient. A higher coefficient effectively increases the amplitude. Therefore, the library could consist of the basis functions, scaled along the temporary axis.

Conclusion

K-means with PCA-reduced dimensionality (8 principal components) was deemed the most suitable clustering algorithm. Performing the clustering on SPs across the atrial surface during AF resulted in a total of 5 clusters, mostly distinguishable by RS-ratio and respective duration of the potential. Regional occurrence of the different clusters through the scope of RS-wave morphology showed patterns not evidently different from described RS-wave morphologies during SR. BB showed evidently increased occurrence clusters containing a low-amplitude, slowly-conducing S-wave morphology. Both indicate the possible broader contribution of atrial tissue components than solely the LA, which is mostly targeted during electrophysiological procedures. Further research regarding the description of potentials consisting of multiple deflections and analysis of patients with different AF subtypes could aid in further understanding of tissue deterioration through the course of AF. Both encourage understanding of the (individualized) tissue characteristics to help in selecting eligible patients for treatment and better indications of AF progression state.

References

1. Kannel WB, Wolf PA, Benjamin EJ, Levy D. Prevalence, incidence, prognosis, and predisposing conditions for atrial fibrillation: population-based estimates. The American journal of cardiology. 1998;82(7):2N-9N.
2. Watanabe I. Smoking and risk of atrial fibrillation. Elsevier; 2018.
3. Wasmer K, Eckardt L, Breithardt G. Predisposing factors for atrial fibrillation in the elderly. J Geriatr Cardiol. 2017;14(3):179-84.
4. Wolf PA, Abbott RD, Kannel WB. Atrial fibrillation as an independent risk factor for stroke: the Framingham Study. stroke. 1991;22(8):983-8.
5. Soliman EZ, Lopez F, O'Neal WT, Chen LY, Bengtson L, Zhang Z-M, et al. Atrial fibrillation and risk of ST-segment–elevation versus non–ST-segment–elevation myocardial infarction: The Atherosclerosis Risk in Communities (ARIC) Study. Circulation. 2015;131(21):1843-50.
6. Soliman EZ, Safford MM, Muntner P, Khodneva Y, Dawood FZ, Zakai NA, et al. Atrial fibrillation and the risk of myocardial infarction. JAMA internal medicine. 2014;174(1):107-14.
7. Stewart S, Hart CL, Hole DJ, McMurray JJV. A population-based study of the long-term risks associated with atrial fibrillation: 20-year follow-up of the Renfrew/Paisley study. The American journal of medicine. 2002;113(5):359-64.
8. Lee E, Choi E-K, Han K-D, Lee H, Choe W-S, Lee S-R, et al. Mortality and causes of death in patients with atrial fibrillation: a nationwide population-based study. PLoS One. 2018;13(12):e0209687.
9. Krijthe BP, Kunst A, Benjamin EJ, Lip GYH, Franco OH, Hofman A, et al. Projections on the number of individuals with atrial fibrillation in the European Union, from 2000 to 2060. European heart journal. 2013;34(35):2746-51.
10. Mandapati R, Skanes A, Chen J, Berenfeld O, Jalife J. Stable microreentrant sources as a mechanism of atrial fibrillation in the isolated sheep heart. Circulation. 2000;101(2):194-9.
11. Narayan SM, Krummen DE, Shivkumar K, Clopton P, Rappel W-J, Miller JM. Treatment of atrial fibrillation by the ablation of localized sources: CONFIRM (Conventional Ablation for Atrial Fibrillation With or Without Focal Impulse and Rotor Modulation) trial. Journal of the American College of Cardiology. 2012;60(7):628-36.
12. Nattel S. New ideas about atrial fibrillation 50 years on. Nature. 2002;415(6868):219-26.
13. de Groot N, Van Der Does L, Yaksh A, Lanters E, Teuwen C, Knops P, et al. Direct proof of endo-epicardial asynchrony of the atrial wall during atrial fibrillation in humans. Circulation: Arrhythmia and Electrophysiology. 2016;9(5):e003648.
14. Buch E, Share M, Tung R, Benharash P, Sharma P, Koneru J, et al. Long-term clinical outcomes of focal impulse and rotor modulation for treatment of atrial fibrillation: A multicenter experience. Heart Rhythm. 2016;13(3):636-41.
15. Verma A, Jiang C-y, Betts TR, Chen J, Deisenhofer I, Mantovan R, et al. Approaches to catheter ablation for persistent atrial fibrillation. New England Journal of Medicine. 2015;372(19):1812-22.
16. Allessie M, Ausma J, Schotten U. Electrical, contractile and structural remodeling during atrial fibrillation. Cardiovascular research. 2002;54(2):230-46.
17. Issa ZF, Miller JM, Zipes DP. Clinical arrhythmology and electrophysiology: a companion to Braunwald's heart disease: Elsevier Health Sciences; 2009.
18. Yaksh A, van der Does LJME, Kik C, Knops P, Oei FBS, van de Woestijne PC, et al. A novel intra-operative, high-resolution atrial mapping approach. Journal of Interventional Cardiac Electrophysiology. 2015;44(3):221-5.
19. Konings KTS, Smeets JLRM, Penn OC, Wellens HJJ, Allessie MA. Configuration of unipolar atrial electrograms during electrically induced atrial fibrillation in humans. Circulation. 1997;95(5):1231-41.
20. Ye Z, van Schie MS, De Groot N. Signal Fingerprinting as a Novel Diagnostic Tool to Identify Conduction Inhomogeneity. Frontiers in physiology. 2021;12:375.

21. van Schie MS, Starreveld R, Roos-Serote MC, Taverne YJHJ, van Schaagen FRN, Bogers AJJC, et al. Classification of sinus rhythm single potential morphology in patients with mitral valve disease. EP Europace. 2020;22(10):1509-19.
22. van Schie MS, Starreveld R, Bogers AJJC, de Groot NMS. Sinus rhythm voltage fingerprinting in patients with mitral valve disease using a high-density epicardial mapping approach. EP Europace. 2021;23(3):469-78.
23. Allessie MA, de Groot NMS, Houben RPM, Schotten U, Boersma E, Smeets JL, et al. Electropathological substrate of long-standing persistent atrial fibrillation in patients with structural heart disease: longitudinal dissociation. Circulation: Arrhythmia and Electrophysiology. 2010;3(6):606-15.
24. Zeemering S, Bonizzi P, Maesen B, Peeters R, Schotten U, editors. Recurrence quantification analysis applied to spatiotemporal pattern analysis in high-density mapping of human atrial fibrillation. 2015 37th Annual International Conference of the IEEE Engineering in Medicine and Biology Society (EMBC); 2015: IEEE.
25. Orozco-Duque A, Duque SI, Ugarte JP, Tobón C, Novak D, Kremen V, et al., editors. Fractionated electrograms and rotors detection in chronic atrial fibrillation using model-based clustering. 2014 36th Annual International Conference of the IEEE Engineering in Medicine and Biology Society; 2014: IEEE.
26. Almeida TP, Soriano DC, Mase M, Ravelli F, Bezerra AS, Li X, et al. Unsupervised classification of atrial electrograms for electroanatomic mapping of human persistent atrial fibrillation. IEEE Transactions on Biomedical Engineering. 2020;68(4):1131-41.
27. Caulier-Cisterna R, Blanco-Velasco M, Goya-Esteban R, Muñoz-Romero S, Sanromán-Junquera M, García-Alberola A, et al. Spatial-Temporal Signals and Clinical Indices in Electrocardiographic Imaging (II): Electrogram Clustering and T-Wave Alternans. Sensors. 2020;20(11):3070.
28. Benjamin EJ, Levy D, Vaziri SM, D'Agostino RB, Belanger AJ, Wolf PA. Independent risk factors for atrial fibrillation in a population-based cohort: the Framingham Heart Study. Jama. 1994;271(11):840-4.
29. Psaty BM, Manolio TA, Kuller LH, Kronmal RA, Cushman M, Fried LP, et al. Incidence of and risk factors for atrial fibrillation in older adults. Circulation. 1997;96(7):2455-61.
30. Bachmann G. The inter-auricular time interval. American Journal of Physiology-Legacy Content. 1916;41(3):309-20.
31. Boron WF, Boulpaep EL. Medical physiology, 2e updated edition e-book: with student consult online access: Elsevier health sciences; 2012.
32. Wong E. Physiology of cardiac conduction and contractility: action potential of cardiac muscles: McMaster Pathophysiology Review; 2013 [updated October 7, 2013. Available from: http://www.pathophys.org/physiology-of-cardiac-conduction-and-contractility/actionpotential/.
33. Ramdat Misier AR, Opthof T, Van Hemel NM, Defauw JJAM, De Bakker JMT, Janse MJ, et al. Increased dispersion of “refractoriness” in patients with idiopathic paroxysmal atrial fibrillation. Journal of the American College of Cardiology. 1992;19(7):1531-5.
34. De Jong AM, Maass AH, Oberdorf-Maass SU, Van Veldhuisen DJ, Van Gilst WH, Van Gelder IC. Mechanisms of atrial structural changes caused by stretch occurring before and during early atrial fibrillation. Cardiovascular research. 2011;89(4):754-65.
35. Spach MS, Heidlage JF, Dolber PC, Roger C. Changes in anisotropic conduction caused by remodeling cell size and the cellular distribution of gap junctions and Na+ channels. Journal of electrocardiology. 2001;34(4):69-76.
36. Schotten U, Neuberger H-R, Allessie MA. The role of atrial dilatation in the domestication of atrial fibrillation. Progress in biophysics and molecular biology. 2003;82(1-3):151-62.
37. Yu W-C, Lee S-H, Tai C-T, Tsai C-F, Hsieh M-H, Chen C-C, et al. Reversal of atrial electrical remodeling following cardioversion of long-standing atrial fibrillation in man. Cardiovascular research. 1999;42(2):470-6.
38. Van Gelder IC, Hemels MEW. The progressive nature of atrial fibrillation: a rationale for early restoration and maintenance of sinus rhythm. Europace. 2006;8(11):943-9.

39. January CT, Wann LS, Alpert JS, Calkins H, Cigarroa JE, Cleveland JC, et al. 2014 AHA/ACC/HRS guideline for the management of patients with atrial fibrillation: a report of the American College of Cardiology/American Heart Association Task Force on Practice Guidelines and the Heart Rhythm Society. Journal of the American College of Cardiology. 2014;64(21):e1-e76.
40. Lippi G, Sanchis-Gomar F, Cervellin G. Global epidemiology of atrial fibrillation: An increasing epidemic and public health challenge. International Journal of Stroke. 2021;16(2):217-21.
41. Zoni-Berisso M, Filippi A, Landolina M, Brignoli O, D'Ambrosio G, Maglia G, et al. Frequency, patient characteristics, treatment strategies, and resource usage of atrial fibrillation (from the Italian Survey of Atrial Fibrillation Management [ISAF] study). The American journal of cardiology. 2013;111(5):705-11.
42. Kerr CR, Humphries KH, Talajic M, Klein GJ, Connolly SJ, Green M, et al. Progression to chronic atrial fibrillation after the initial diagnosis of paroxysmal atrial fibrillation: results from the Canadian Registry of Atrial Fibrillation. American heart journal. 2005;149(3):489-96.
43. De Sisti A, Leclercq JF, Halimi F, Fiorello P, Bertrand C, Attuel P. Evaluation of time course and predicting factors of progression of paroxysmal or persistent atrial fibrillation to permanent atrial fibrillation. Pacing and Clinical Electrophysiology. 2014;37(3):345-55.
44. Venkatachalam KL, Herbrandson JE, Asirvatham SJ. Signals and signal processing for the electrophysiologist: part I: electrogram acquisition. Circulation: Arrhythmia and Electrophysiology. 2011;4(6):965-73.
45. De Bakker JMT, Wittkampf FHM. The pathophysiologic basis of fractionated and complex electrograms and the impact of recording techniques on their detection and interpretation. Circulation: Arrhythmia and Electrophysiology. 2010;3(2):204-13.
46. Sim I, Bishop M, O'Neill M, Williams SE. Left atrial voltage mapping: defining and targeting the atrial fibrillation substrate. Journal of Interventional Cardiac Electrophysiology. 2019:1-15.
47. Jacquemet V, Virag N, Ihara Z, Dang LAM, Blanc O, Zozor S, et al. Study of unipolar electrogram morphology in a computer model of atrial fibrillation. Journal of cardiovascular electrophysiology. 2003;14:S172-S9.
48. Vlachos K, Efremidis M, Letsas KP, Bazoukis G, Martin R, Kalafateli M, et al. Low-voltage areas detected by high-density electroanatomical mapping predict recurrence after ablation for paroxysmal atrial fibrillation. Journal of cardiovascular electrophysiology. 2017;28(12):1393-402.
49. Spach MS, Miller 3rd WT, Miller-Jones E, Warren RB, Barr RC. Extracellular potentials related to intracellular action potentials during impulse conduction in anisotropic canine cardiac muscle. Circulation Research. 1979;45(2):188-204.
50. Esteva A, Kuprel B, Novoa RA, Ko J, Swetter SM, Blau HM, et al. Dermatologist-level classification of skin cancer with deep neural networks. nature. 2017;542(7639):115-8.
51. Liu S, Liu S, Cai W, Pujol S, Kikinis R, Feng D, editors. Early diagnosis of Alzheimer's disease with deep learning. 2014 IEEE 11th international symposium on biomedical imaging (ISBI); 2014: IEEE.
52. Biswal S, Sun H, Goparaju B, Westover MB, Sun J, Bianchi MT. Expert-level sleep scoring with deep neural networks. Journal of the American Medical Informatics Association. 2018;25(12):1643-50.
53. Hannun AY, Rajpurkar P, Haghpanahi M, Tison GH, Bourn C, Turakhia MP, et al. Cardiologist-level arrhythmia detection and classification in ambulatory electrocardiograms using a deep neural network. Nature medicine. 2019;25(1):65-9.
54. Lopez C, Tucker S, Salameh T, Tucker C. An unsupervised machine learning method for discovering patient clusters based on genetic signatures. Journal of biomedical informatics. 2018;85:30-9.
55. Lanters EAH, van Marion DMS, Kik C, Steen H, Bogers AJJC, Allessie MA, et al. HALT & REVERSE: Hsf1 activators lower cardiomyocyt damage; towards a novel approach to REVERSE atrial fibrillation. Journal of translational medicine. 2015;13(1):1-7.
56. van der Does LJME, Yaksh A, Kik C, Knops P, Lanters EAH, Teuwen CP, et al. QUest for the Arrhythmogenic Substrate of Atrial fibRillation in Patients Undergoing Cardiac Surgery (QUASAR study): rationale and design. Journal of cardiovascular translational research. 2016;9(3):194-201.

57. Kik C, Mouws EMJP, Bogers AJJC, de Groot NMS. Intra-operative mapping of the atria: the first step towards individualization of atrial fibrillation therapy? Expert review of cardiovascular therapy. 2017;15(7):537-45.
58. Shkurovich S, Sahakian AV, Swiryn S. Detection of atrial activity from high-voltage leads of implantable ventricular defibrillators using a cancellation technique. IEEE Transactions on Biomedical Engineering. 1998;45(2):229-34.
59. Petrutiu S, Ng J, Nijm GM, Al-Angari H, Swiryn S, Sahakian AV. Atrial fibrillation and waveform characterization. IEEE Engineering in Medicine and Biology Magazine. 2006;25(6):24-30.
60. Rieta JJ, Castells F, Sanchez C, Zarzoso V, Millet J. Atrial activity extraction for atrial fibrillation analysis using blind source separation. IEEE Transactions on Biomedical Engineering. 2004;51(7):1176-86.
61. Pan J, Tompkins WJ. A Real-Time QRS Detection Algorithm. IEEE Transactions on Biomedical Engineering. 1985;BME-32(3):230-6.
62. MacQueen J, editor Some methods for classification and analysis of multivariate observations. Proceedings of the fifth Berkeley symposium on mathematical statistics and probability; 1967: Oakland, CA, USA.
63. Jain AK. Data clustering: 50 years beyond K-means. Pattern Recognition Letters. 2010;31(8):651-66.
64. Pedregosa F, Varoquaux G, Gramfort A, Michel V, Thirion B, Grisel O, et al. Scikit-learn: Machine learning in Python. the Journal of machine Learning research. 2011;12:2825-30.
65. Arthur D, Vassilvitskii S. k-means++: The advantages of careful seeding. Stanford, 2006.
66. Rasmussen CE, editor The infinite Gaussian mixture model. Nips; 1999.
67. Dempster AP, Laird NM, Rubin DB. Maximum likelihood from incomplete data via the EM algorithm. Journal of the Royal Statistical Society: Series B (Methodological). 1977;39(1):1-22.
68. Ester M, Kriegel H-P, Sander J, Xu X, editors. A density-based algorithm for discovering clusters in large spatial databases with noise. kdd; 1996.
69. Sander J, Ester M, Kriegel H-P, Xu X. Density-based clustering in spatial databases: The algorithm gdbscan and its applications. Data mining and knowledge discovery. 1998;2(2):169-94.
70. Rahmah N, Sitanggang IS, editors. Determination of optimal epsilon (eps) value on dbscan algorithm to clustering data on peatland hotspots in sumatra. IOP conference series: earth and environmental science; 2016: IOP Publishing.
71. Berndt DJ, Clifford J, editors. Using dynamic time warping to find patterns in time series. KDD workshop; 1994: Seattle, WA, USA:.
72. Sakoe H, Chiba S. Dynamic programming algorithm optimization for spoken word recognition. IEEE Transactions on Acoustics, Speech, and Signal Processing. 1978;26(1):43-9.
73. Senin P. Dynamic time warping algorithm review. Information and Computer Science Department University of Hawaii at Manoa Honolulu, USA. 2008;855(1-23):40.
74. Cuturi M, Blondel M, editors. Soft-dtw: a differentiable loss function for time-series. International Conference on Machine Learning; 2017: PMLR.
75. Beyer K, Goldstein J, Ramakrishnan R, Shaft U, editors. When is “nearest neighbor” meaningful? International conference on database theory; 1999: Springer.
76. Hinneburg A, Aggarwal CC, Keim DA, editors. What is the nearest neighbor in high dimensional spaces? 26th Internat Conference on Very Large Databases; 2000.
77. Xia S, Xiong Z, Luo Y, Zhang G. Effectiveness of the Euclidean distance in high dimensional spaces. Optik. 2015;126(24):5614-9.
78. Li Z-X, Guo J-S, Hui X-B, Song F-F. Dimension reduction method for multivariate time series based on common principal component. Control and Decision. 2013;28(4):531-6.
79. Rousseeuw PJ. Silhouettes: a graphical aid to the interpretation and validation of cluster analysis. Journal of computational and applied mathematics. 1987;20:53-65.
80. Thorndike RL. Who belongs in the family? Psychometrika. 1953;18(4):267-76.
81. Schwarz G. Estimating the dimension of a model. The annals of statistics. 1978:461-4.

82. Akaike H. A new look at the statistical model identification. IEEE Transactions on Automatic Control. 1974;19(6):716-23.
83. Ng J, Gordon D, Passman RS, Knight BP, Arora R, Goldberger JJ. Electrogram morphology recurrence patterns during atrial fibrillation. Heart Rhythm. 2014;11(11):2027-34.
84. Ho SY, Anderson RH, Sánchez-Quintana D. Atrial structure and fibres: morphologic bases of atrial conduction. Cardiovascular research. 2002;54(2):325-36.
85. Haissaguerre M, Jaïs P, Shah DC, Takahashi A, Hocini M, Quiniou G, et al. Spontaneous initiation of atrial fibrillation by ectopic beats originating in the pulmonary veins. New England Journal of Medicine. 1998;339(10):659-66.
86. Stiles MK, Brooks AG, Kuklik P, John B, Dimitri H, Lau DH, et al. High-density mapping of atrial fibrillation in humans: Relationship between high-frequency activation and electrogram fractionation. Journal of cardiovascular electrophysiology. 2008;19(12):1245-53.
87. Park JH, Pak HN, Kim SK, Jang JK, Choi JI, Lim HE, et al. Electrophysiologic characteristics of complex fractionated atrial electrograms in patients with atrial fibrillation. Journal of cardiovascular electrophysiology. 2009;20(3):266-72.
88. Krummen DE, Peng KA, Bullinga JR, Narayan SM. Centrifugal gradients of rate and organization in human atrial fibrillation. Pacing and clinical electrophysiology. 2009;32(11):1366-78.
89. Wagner ML, Lazzara R, Weiss RM, Hoffman BF. Specialized conducting fibers in the interatrial band. Circulation research. 1966;18(5):502-18.
90. Childers RW, Merideth J, Moe GK. Supernormality in Bachmann's bundle: an in vitro and in vivo study in the dog. Circulation research. 1968;22(3):363-70.
91. Goodman D, Van Der Steen AB, Van Dam RT. Endocardial and epicardial activation pathways of the canine right atrium. American Journal of Physiology-Legacy Content. 1971;220(1):1-11.
92. Hayashi H, Lux RL, Wyatt RF, Burgess MJ, Abildskov JA. Relation of canine atrial activation sequence to anatomic landmarks. American Journal of Physiology-Heart and Circulatory Physiology. 1982;242(3):H421-H8.
93. Horiba M. Stimulus Conduction in Atria Studied by Means of Intracellular Microelectrode Part I. That in Bachmann's Bundle. Japanese heart journal. 1963;4(4):333-45.
94. Jais P, Haissaguerre M, Shah DC, Chouairi S, Clementy J. Regional disparities of endocardial atrial activation in paroxysmal atrial fibrillation. Pacing and clinical electrophysiology. 1996;19(11):1998-2003.
95. Dunn JC. A fuzzy relative of the ISODATA process and its use in detecting compact well-separated clusters. 1973.
96. Bezdek JC. Pattern recognition with fuzzy objective function algorithms: Springer Science & Business Media; 2013.
97. de Groot NMS, Houben RPM, Smeets JL, Boersma E, Schotten U, Schalij MJ, et al. Electropathological substrate of longstanding persistent atrial fibrillation in patients with structural heart disease: epicardial breakthrough. Circulation. 2010;122(17):1674-82.
98. Kirubakaran S, Chowdhury RA, Hall MCS, Patel PM, Garratt CJ, Peters NS. Fractionation of electrograms is caused by colocalized conduction block and connexin disorganization in the absence of fibrosis as AF becomes persistent in the goat model. Heart Rhythm. 2015;12(2):397-408.
99. Eckstein J, Maesen B, Linz D, Zeemering S, Van Hunnik A, Verheule S, et al. Time course and mechanisms of endo-epicardial electrical dissociation during atrial fibrillation in the goat. Cardiovascular research. 2011;89(4):816-24.
100. Rienstra M, Lubitz SA, Mahida S, Magnani JW, Fontes JD, Sinner MF, et al. Symptoms and functional status of patients with atrial fibrillation: state of the art and future research opportunities. Circulation. 2012;125(23):2933-43.
101. Calkins H, Hindricks G, Cappato R, Kim Y-H, Saad EB, Aguinaga L, et al. 2017 HRS/EHRA/ECAS/APHRS/SOLAECE expert consensus statement on catheter and surgical ablation of atrial fibrillation: executive summary. 2017.
102. Parameswaran R, Al-Kaisey AM, Kalman JM. Catheter ablation for atrial fibrillation: current indications and evolving technologies. Nature Reviews Cardiology. 2021;18(3):210-25.

103. Willems S, Klemm H, Rostock T, Brandstrup B, Ventura R, Steven D, et al. Substrate modification combined with pulmonary vein isolation improves outcome of catheter ablation in patients with persistent atrial fibrillation: a prospective randomized comparison. European heart journal. 2006;27(23):2871-8.
104. Fassini G, Riva S, Chiodelli R, Trevisi N, Berti M, Carbucicchio C, et al. Left mitral isthmus ablation associated with PV isolation: long-term results of a prospective randomized study. Journal of cardiovascular electrophysiology. 2005;16(11):1150-6.
105. Correa de Sa DD, Thompson N, Stinnett-Donnelly J, Znojkiewicz P, Habel N, Müller JG, et al. Electrogram fractionation: the relationship between spatiotemporal variation of tissue excitation and electrode spatial resolution. Circulation: Arrhythmia and Electrophysiology. 2011;4(6):909-16.
106. Podziemski P, Kuklik P, van Hunnik A, Zeemering S, Maesen B, Schotten U, editors. Far-field effect in unipolar electrograms revisited: High-density mapping of atrial fibrillation in humans. 2015 37th Annual International Conference of the IEEE Engineering in Medicine and Biology Society (EMBC); 2015: IEEE.
107. Houben RPM, de Groot NMS, Lindemans FW, Allessie MA. Automatic mapping of human atrial fibrillation by template matching. Heart Rhythm. 2006;3(10):1221-8.
108. Mallat SG, Zhang Z. Matching pursuits with time-frequency dictionaries. IEEE Transactions on signal processing. 1993;41(12):3397-415.

Appendices 5

Appendices

I. Appendix I: Additional clustering results

A. PV and BB clustering

The evaluation metrics for the PV region and BB are displayed in Figure 38. The PV region shows a preferential cluster number of four, as shown by the local maximum in the silhouette score and the point of maximum curvature in the graph using the elbow method. The observed pattern is in line with the clustering results from all regions and RA data. The evaluation metrics using solely potentials from BB show no evident number of clusters. From the elbow method, it could be argued that the point of maximum curvature is at four clusters at well. This number of clusters is not obvious when looking at the silhouette scores. In correspondence with clustering based on input data from other regions, the formed clusters using a four and five-cluster approach are visualized.

The results of the aforementioned approaches are shows in Figure 39. Using a four-cluster approach, the PV region shows the previously observed cluster without iso-electric segment (indicated by the yellow dots at the right bottom) and lacks the cluster with a RS-ratio of 0 (indicated by the red dots at the right bottom). Last mentioned appears when adapting a five-cluster approach based on potentials from the PV region. The observed pattern in clustering outcome is similar to the observed pattern using a potentials solely originating from the RA. Using BB potentials, a four-cluster approach shows clusters with mean structures corresponding with the results from a four-cluster approach with data from all regions. However, the result of a five-cluster approach does not show the occurrence of the expected cluster (with RS-ratio of 0). Instead, a cluster similar to the already present cluster appears (the second and fifth cluster).

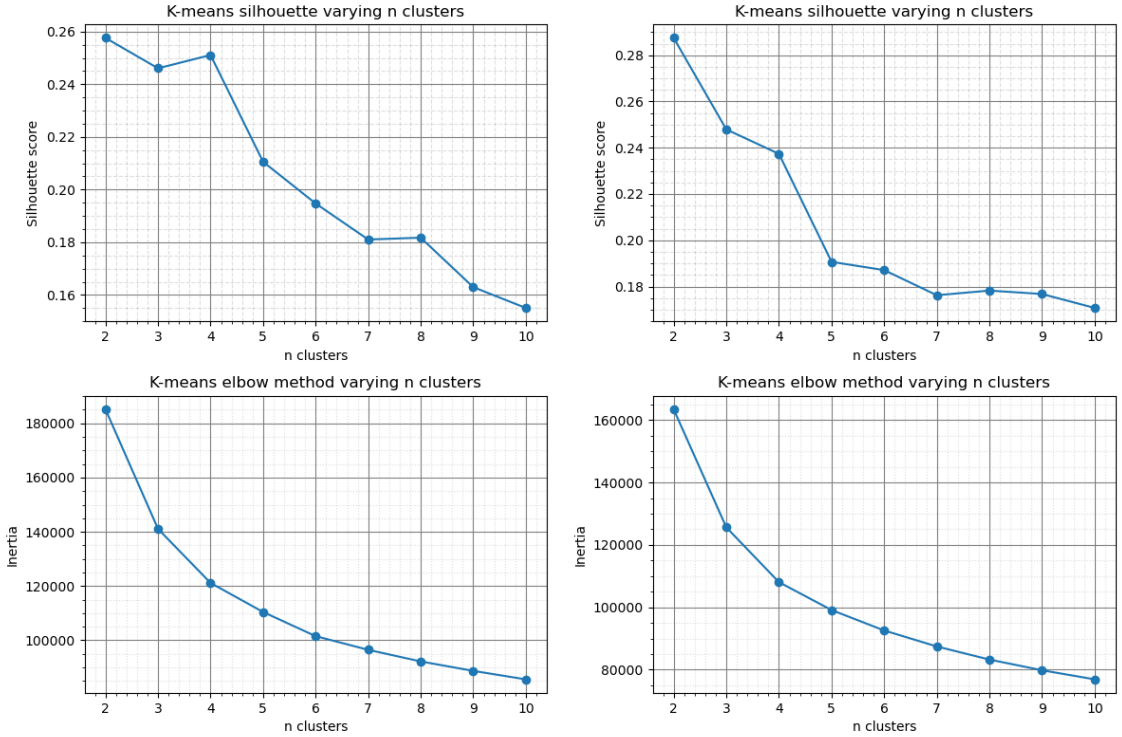

Figure 38: Silhouette score and elbow method for both the PV region (left) and BB (right).

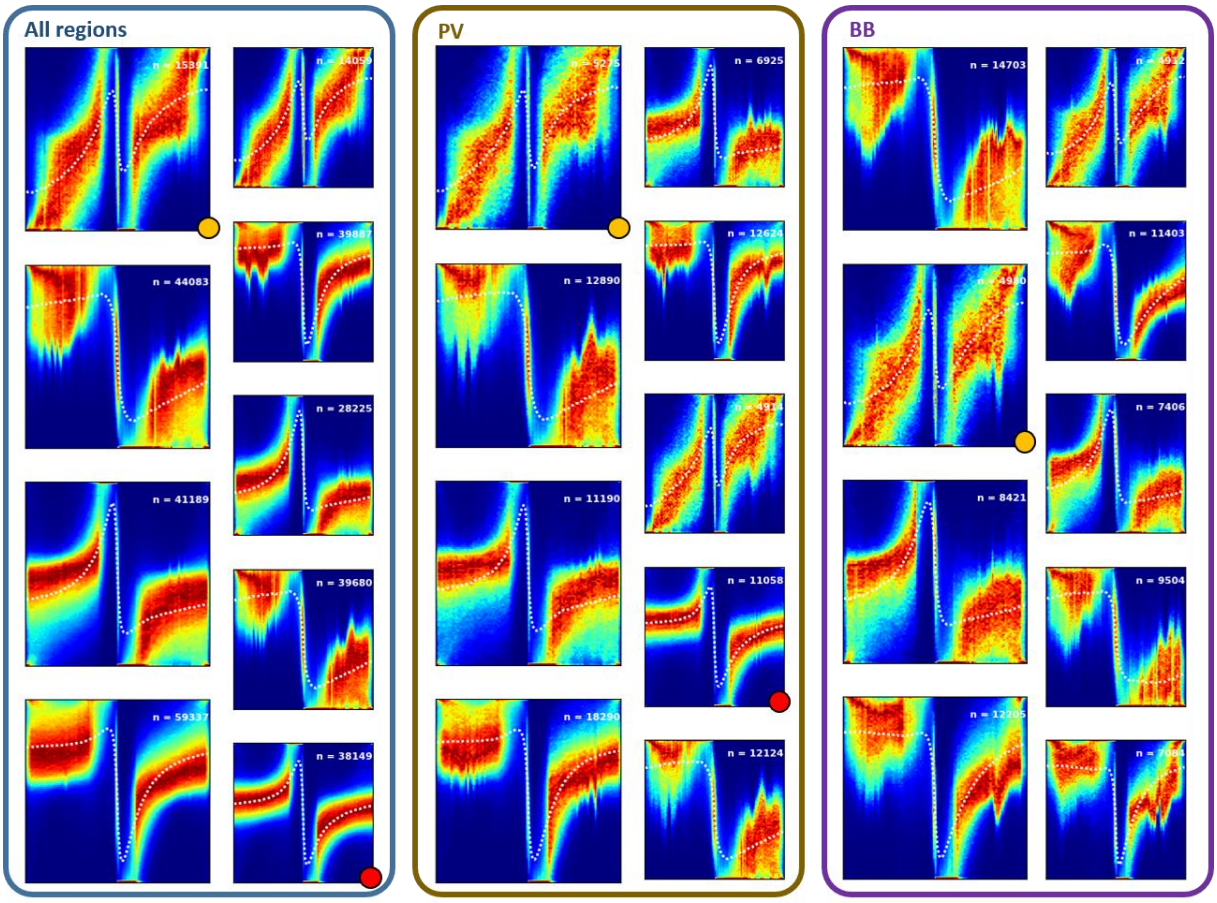

Figure 39: Results using a four and five-cluster approach for different regional inputs.

B. Increased cluster results

The results of increasing the number of clusters with data from all regions is displayed in Figure 40. When increasing from a four to a five-cluster approach, a new morphological structure appears (indicated with the red dot at the right bottom of the heatmap). Although a substantially lower silhouette score is observed using a four-cluster compared to a five-cluster approach in data originating from all regions, the different morphological cluster combined with the preferential five-cluster approach from LA data indicates the usage of five clusters to be preferential. Increasing to a six-cluster approach creates clusters with the same morphological structure (indicated with the yellow dots at the right bottom of the heatmaps). Increase from a number of five to six clusters is therefore undesirable.

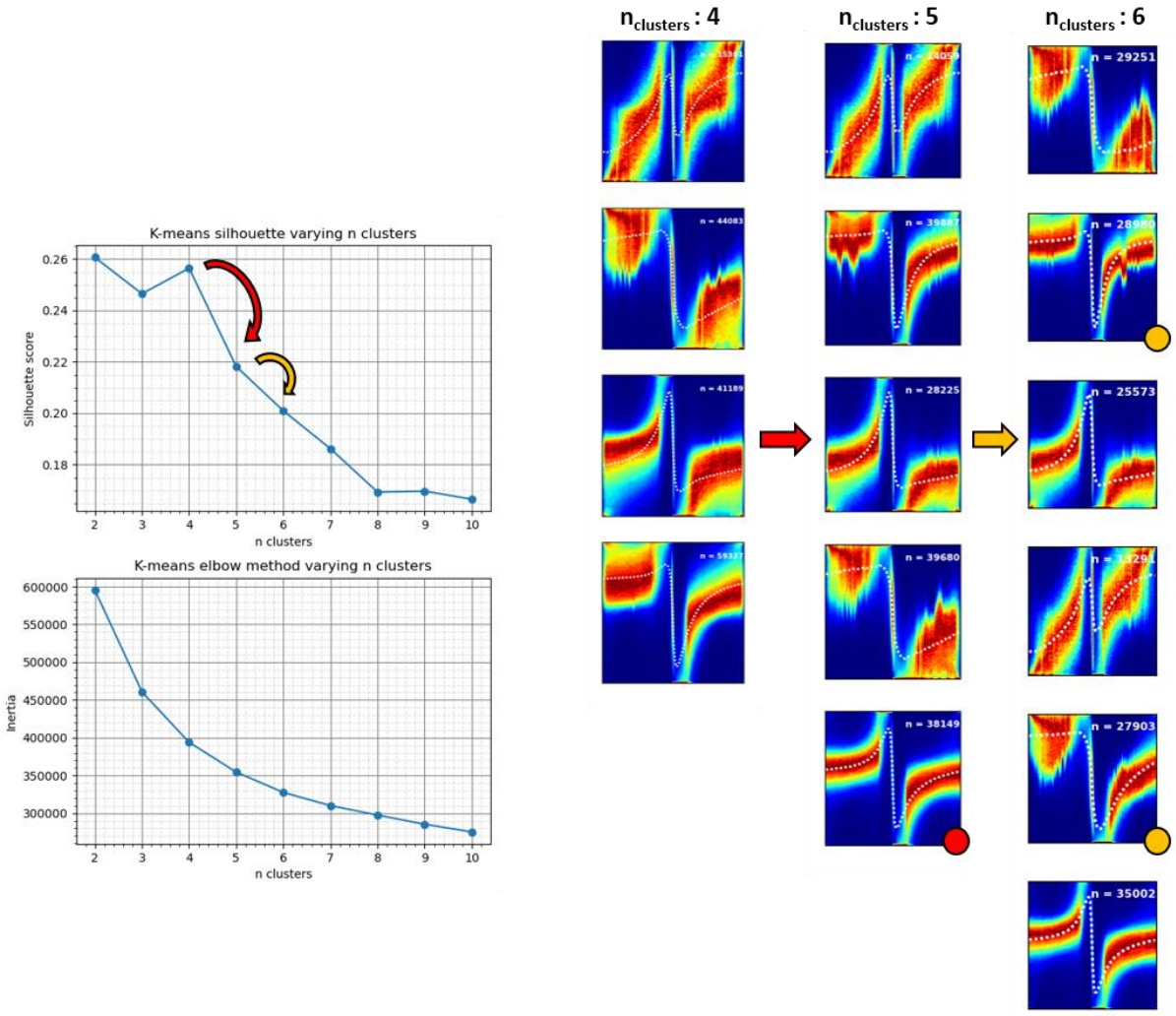

Figure 40: Increasing from a four to a six-cluster approach results (data originating from all regions).

II. Appendix II: Soft clustering application

The previous results of the usage of GMM with spherical covariance type are displayed below (Figure 41, panel A), followed by the distribution of the probabilities (using the four-culster approach on 160000 potentials from all regions, Figure 41, panel B). The far majority of potentials showed a high probability to belong to one of the defined clusters (97.57%) of the included potentials. However, there are also potentials present from which the posterior probability distribution is not evident. To show the morphologies of potentials with a less evident cluster to assign, three groups are visualized in heatmaps based on the probability to the most likely cluster: 0-50%, 50-75% and 75-95%. The heatmaps are displayed in Figure 41, panel C. In the group with a probability between 0-50%, solely 8 potentials were identified, resulting in the inability to create an adequate heatmap. Although the number low number of potentials in the heatmaps causes scattered heatmaps, all groups show a general morphology approaching a potential with a RS-ratio of zero.

When comparing this to the originally identified clusters (Figure 41, panel A), the same general morphological structure is not observed. The inability to adequately define the most suitable cluster can be impeded. The confusion matrices in Figure 41, panel D show the cluster with the highest probability for the individual groups. Color coding is relative to the total number of potentials. The y-axis shows the cluster with the highest probability and the x-axis shows the cluster with the second highest probability. The confusion matrix of all potentials with a probability below 95% is shown in Figure 41, panel E. The color bar provided in Figure 41 panel E, does not match with the color coding in Figure 41 panel D.

When less evident potentials are grouped in the first or second cluster, the probability of the potential to fall under the third or fourth and vice versa. Crossover probability between the first and second cluster and between the third and fourth cluster is less prominent. When observing the original cluster, this is coherent with the general structures observed. The inability to inadequately cluster potentials with a morphology not occurring in the original clustering structures is highlighted by the decreased probabilities using a soft clustering algorithm.

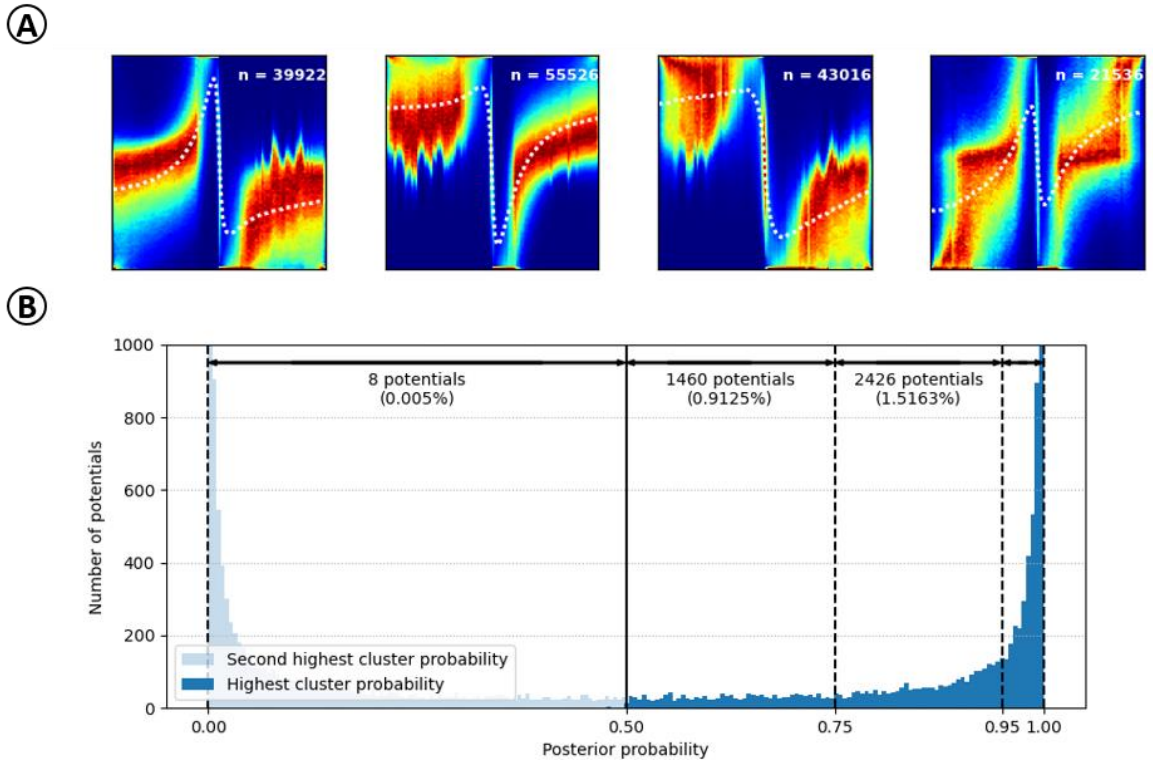

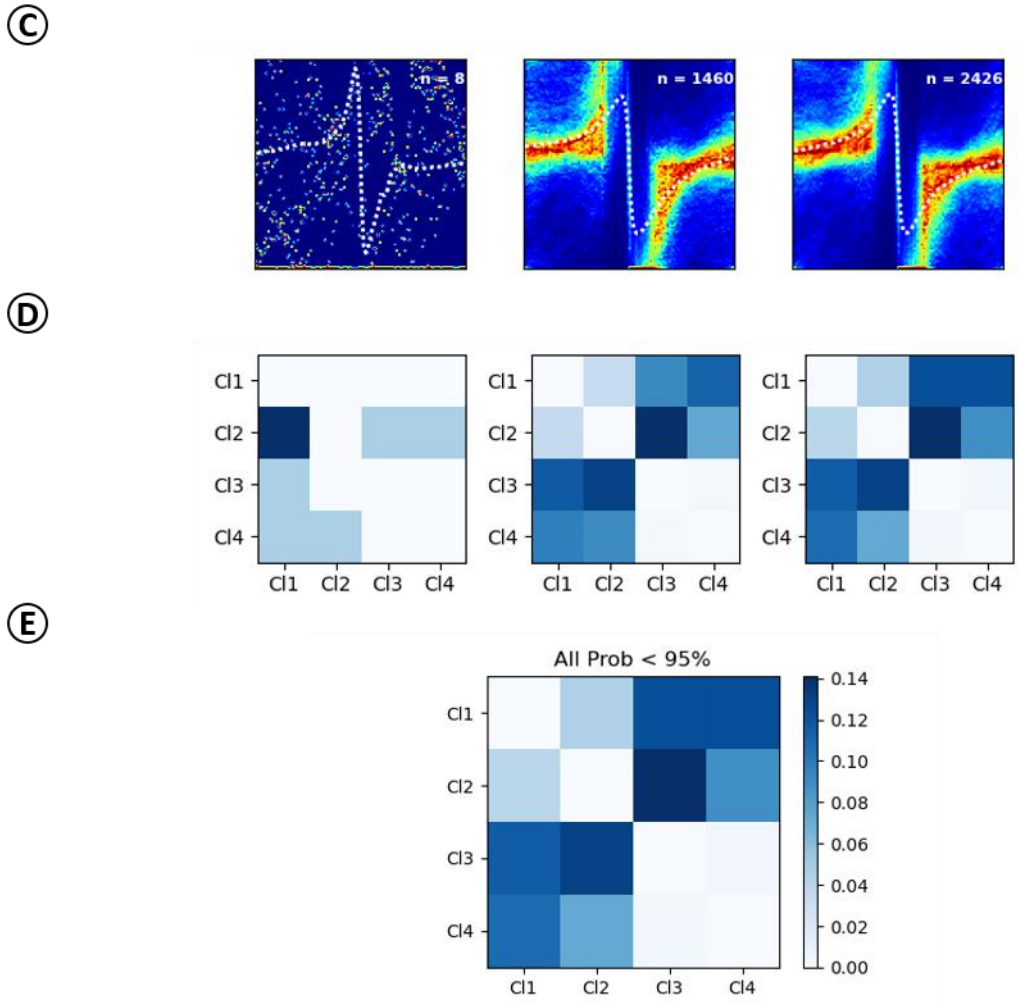

Figure 41: Overview of soft-clustering application. Panel A shows the results of GMM with spherical covariance for 4 clusters. Panel B shows the distribution of highest and second highest probabilities of the included clusters. Panel C shows the heatmaps of potentials falling in groups of lowered probability to be assigned to a cluster (from left to right: 0-50%, 50-75% and 75-95%). Panel D shows the confusion matrices of the potentials in line with groups in panel C. Panel E shows the confusion matrix of all potentials with a posterior probability to the most likely cluster of <95%.

Note that this appendix does not focus on the best clustering method, which is shown to be with k-means. However, the appendix shows that potentials do not always need to follow the morphologic structures from general structure of one of the identified clusters. Applying a threshold for a minimal probability of a potential to belong to a certain cluster could mediate in defining the boundaries towards the identified mean structures in the clusters.

III. Appendix III: Atrial fibrillation subtype analysis

The results from the regional analysis in patients with PAF are displayed in Figure 42: Regional analysis of cluster occurrence during PAF.. The corresponding results from the perspective of the five clusters for patients in PAF are displayed in Figure 43. Figure 44 and Figure 45 display the figures for the case of patients with LSPAF. summarizes the observations from both analyses Table 5.

Table 5: Overview of mean occurrence percentage across different regions and clusters during PAF and LSPAF. Values are displayed as median and interquartile range.

	PAF (n_{pat} = 4)				**LSPAF** (n_{pat} = 3)			
	RA (n_{files} = 12)	**LA** (n_{files} = 6)	**PV** (n_{files} = 4)	**BB** (n_{files} = 4)	**RA** (n_{files} = 9)	**LA** (n_{files} = 6)	**PV** (n_{files} = 2)	**BB** (n_{files} = 3)
Cluster A	16.10 [8.93|22.20]	17.51 [16.20|20.17]	8.62 [7.72|9.94]	9.73 [6.64|12.61]	12.53 [6.17|14.13]	11.38 [9.67|22.72]	26.23 [19.80|32.65]	10.22 [8.06|12.12]
Cluster B	37.52 [26.01|48.72]	10.84 [4.60|18.81]	40.72 [34.58|50.24]	44.36 [40.53|49.23]	32.61 [29.33|35.06]	10.13 [9.06|11.35]	26.58 [21.60|31.56]	40.59 [35.17|47.22]
Cluster C	8.41 [6.32|11.67]	4.37 [2.00|7.60]	21.97 [18.29|26.48]	13.32 [9.39|16.05]	14.00 [13.04|17.15]	10.61 [7.86|14.26]	14.68 [12.40|16.96]	12.07 [11.77|14.61]
Cluster D	17.58 [12.23|27.67]	32.14 [29.84|39.33]	11.85 [8.70|14.97]	14.08 [13.66|17.21]	17.52 [11.72|18.63]	24.27 [17.19|33.76]	18.14 [16.39|19.90]	14.28 [11.96|16.57]
Cluster E	17.25 [11.96|21.75]	22.25 [13.53|29.88]	12.86 [6.72|18.39]	18.30 [15.55|18.93]	25.81 [22.68|32.76]	32.61 [20.16|44.93]	14.38 [8.90|19.86]	20.22 [19.38|21.83]

No statistical analysis is performed. However, the patterns in patients with PAF are similar to the observations when analyzing all subtypes of AF. A general heightened occurrence of cluster B and a according decrease in the occurrence of cluster A is present at most regions compared to the situation in which all subtypes are used, with exception of LA. From a regional perspective, cluster B appears to be occurring more prominently than the other clusters in RA and the PV region. Surprisingly, the data from patients with LSPAF show a pattern in cluster A and B even more resembling the pattern observed when analyzing all subtypes. Especially from a regional perspective, cluster B is less dominantly occurring with respect to the other clusters.

For the subtype analysis, the data is originating from select group of patients. The known inter-individual variance complicates the interpretability of the results. In order to draw conclusions of difference in observed per AF subtype, a larger number of patients should be included in the analysis.

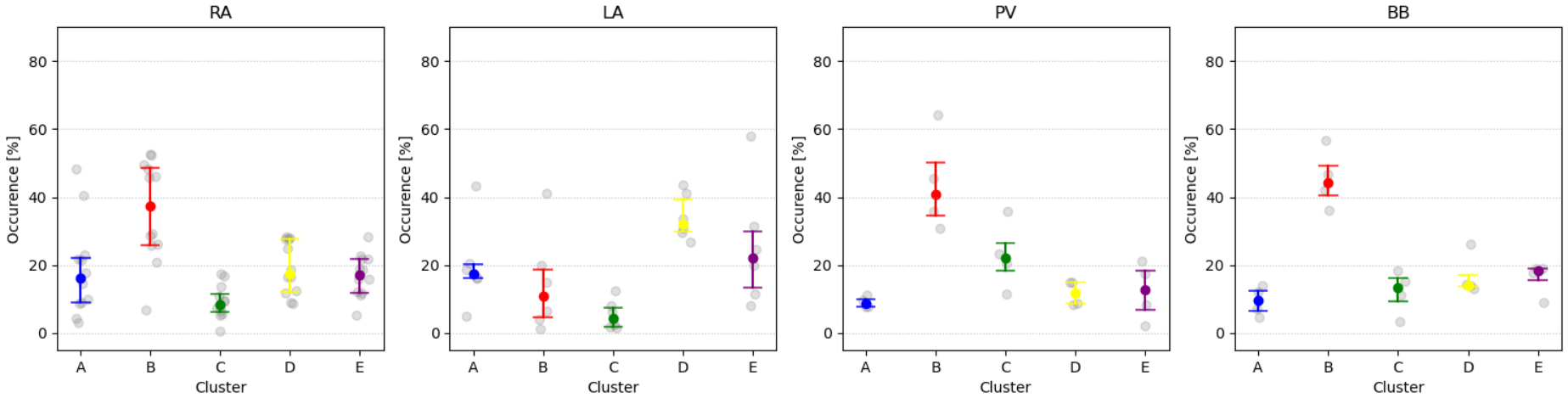

Figure 42: Regional analysis of cluster occurrence during PAF.

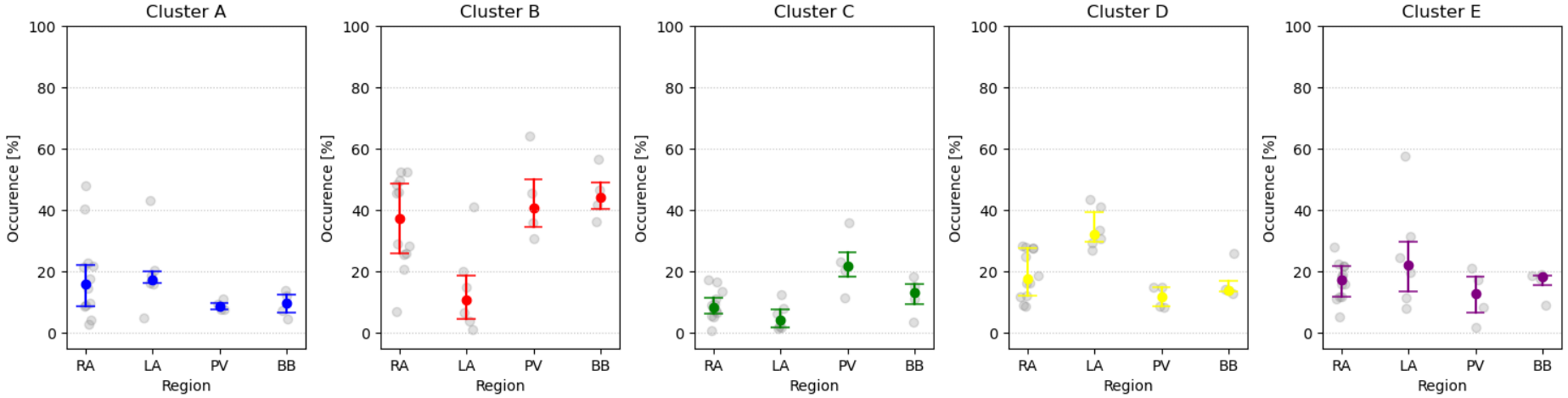

Figure 43: Cluster analysis with occurrence across the different regions during PAF.

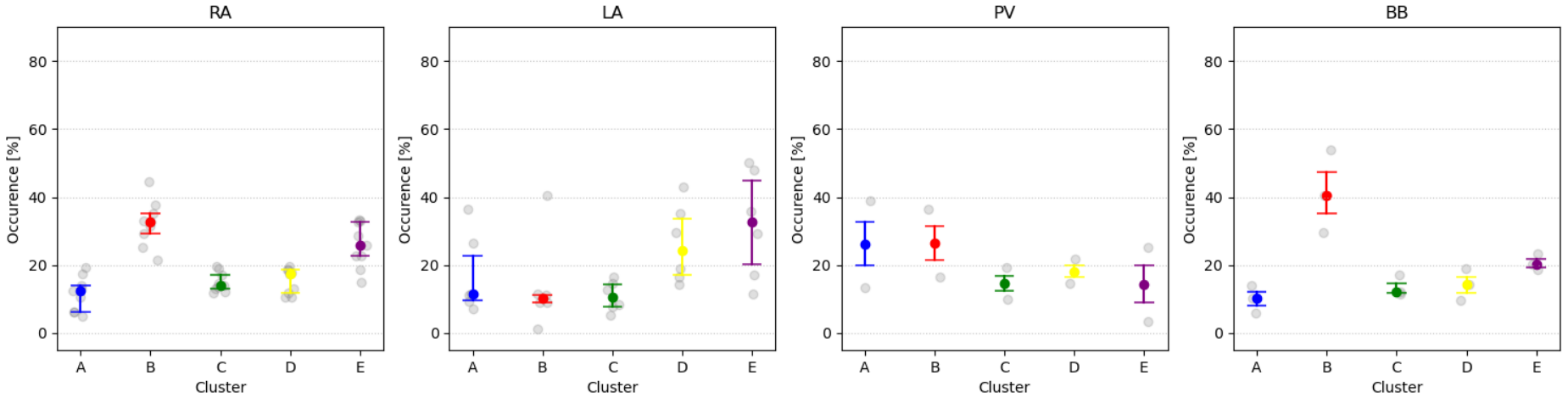

Figure 44: Regional analysis of cluster occurrence during LSPAF.

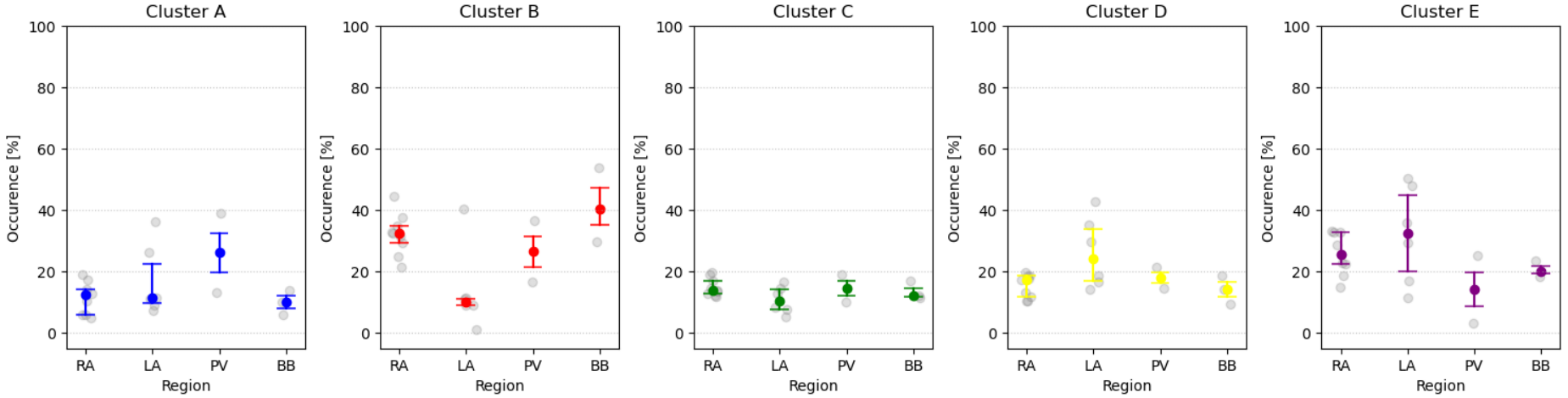

Figure 45: Cluster analysis with occurrence across the different regions during LSPAF.